MODELING THE BEHAVIOR OF FIBER REINFORCED SANDWICH STRUCTURES SUBJECTED TO UNDERWATER EXPLOSIONS

Thesis by

Luigi Emanuele Perotti

In Partial Fulfillment of the Requirements

for the Degree of

Doctor of Philosophy

California Institute of Technology

Pasadena, California

2011

(Defended October 1, 2010)

To my family

Acknowledgements

The research that results in this thesis has only been possible with the constant support of my advisor, Professor Michael Ortiz. He has guided me throughout my studies with constant advice and patience. It was an honor to be one of his graduate students. I will never forget his rigor and enthusiasm in facing new challenging research projects.

Professor Anna Pandolfi motivated me throughout my Ph.D studies, from the application process to the thesis defense day. She has always been available and kind in giving me very useful suggestions and comments regarding my research. I was lucky to meet her during my undergraduate studies in Milan.

I am also very grateful to Professor Guruswami Ravichandran, Professor Sergio Pellegrino and Professor Swaminathan Krishnan who form my thesis committee and who supported me, provided useful insights and suggestions and were always available to answer my questions.

The research presented here is the fruit of a collaboration with Professor Tamer El Sayed (King Abdullah University of Science and Technology - KAUST) and with Dr. Ralf Deiterding (Oak Ridge National Laboratory): I want to express my gratitude to both of them for all the work done together and for the stimulating and fun collaboration. Dr. Ralf Deiterding was heavily involved in building the fluid-solid coupled simulations presented in this thesis: his constancy and detailed explanations were fundamental.

I want to thank the Office of Naval Research for sponsoring this research as part of the DOD MURI program on Mechanics and Mechanisms of Impulse Loading, Damage and Failure of Marine Structures and Materials. (ONR Grant No. N00014-06-1-0730, program manager Dr. Y. D. S. Rajapakse).

I also want to thank my research group and friends for the many discussions we had. Discussing my and others' research problems helped my understanding and has made the research process more stimulating and fun. In particular I would like to thank Agustin,

Celia, Daniel, Francisco, Gabriela, Marcial and Phanish for all the time spent working and having fun together.

I want to thank Marta and Lydia as well, not only for their gracious technical-administrative support but also for the warmth and cheer they bring to the lab.

All my friends at Caltech have been a fundamental ingredient for my happiness during these years of graduate studies: thanks to all of you for the adventures and hikes. Thanks to my officemate Vedran for the fun during the many endless working nights, to Zach for the great hikes and Orienteering events, to the "Luigi's Revenge" basketball team for three great tournaments, to Andrew for the floorball games, to Ahmed and Phanish for the adventurous dinners and the HW nights eating cookies in the office, to Ben and the Renegade's crew for the awesome sailing times ...

Professor Saouma who was my advisor during my previous studies and research in Milan had a fundamental role in motivating me to apply for a Ph.D abroad. I am very thankful to him for inspiring the choice to come here, which has made me very happy.

During these years, even if far from home, I could always count on my friends from high school and undergrad back at home. The always growing Poli "farm" and the "Vittorini-ans" always bring a smile to my face! Thank you guys because every time we see each other it feels like we have always been living in the same place close to each other.

Last, but certainly not least, I have a debt of gratitude to all the members of my family; their unconditional support and encouragement has always provided a safe port. I have been lucky because I had the example and love of my parents Rita and Roberto, of my aunts Pierangela and Danda, of my uncle Angelo, of Jimmy, of my grandparents Luigi, Maria, Giuseppe and Amelia, of my sister Paola, of my cousins Andrea, Anna and Paolo and of my girlfriend Madeline.

Thank you all.

Abstract

Fiber composite material panels and sandwich panels possess both a high resistance to weight ratio and a high stiffness to weight ratio. Due to these features, fiber composite panels are used widely in aeronautic and marine structures, where the improvement of the structural performance while keeping a low weight is crucial. Sandwich structures, consisting of a foam core enclosed by two external layers of fiber reinforced material, seem to be promising in minimizing the total weight, maintaining structural rigidity and improving the resistance under exceptional loads, such as those due to explosions. Full scale experiments to test the performance of real fiber composite sandwich structures subjected to underwater explosions would be very complex and extremely expensive. Therefore, the capability to numerically simulate the response of sandwich structures undergoing explosive loading will provide a powerful and unique tool to analyze and optimize their design by investigating the influence of different parameters. Obviously, small scale laboratory tests will still be essential to validate and calibrate the computational model before its use.

The present research focuses on the development of a computational scheme to model the behavior of large sandwich panels subjected to underwater explosions. The description of the sandwich requires the definition of the material behavior of the components, i.e., the foam core and the external sheets, of the structural behavior of the thin shell structure, and of the interaction with the surrounding fluid. Several finite kinematics material models taken from the recent literature have been used, and a new simple model for fiber reinforced composite has been developed and validated. The thin shell structure is modeled with an existing in-house built non-local shell finite element code (SFC), equipped with fracturing capabilities. The coupling between the behavior of the shells and the action of the fluid as a consequence of an underwater explosion is modeled here with the aid of an existing fluid-solid interaction (FSI) code. In this study, the FSI code has

been expanded in order to include the possibility of simulating fiber composite materials. New algorithms and new control indicators, such as global measures of energy dissipation, have also been developed. The new capabilities of the fluid-solid coupled solver have been verified and validated before applying the solver to realistic problems. In the applications part of the present research, two different methods for applying the pressure load due to an underwater explosion are compared. The first method is simpler, and consists in applying a prescribed pressure profile without considering FSI. In the second method, the explosive charge is modeled as a spherical energy deposition and the full FSI is considered. The simpler method is used to assess the role of different design parameters of the face sheets on the overall response of sandwich panels when subjected to impulsive loads. Subsequently, the best sandwich design obtained from these initial simulations is used for the evaluation of the mechanical performance of the hull section of an existing Argentinean navy vessel. The final application of the proposed computational scheme is a parametric analysis of the hull section, considering different weights of the explosive charge and different distances of the explosion location from the hull wall.

Finally, with awareness of the limits of the adopted approach, several alternative schemes to improve the dynamical analysis of sandwich panels impulsively loaded are presented and discussed. In particular, two different kinds of shell finite elements are introduced. The proposed shell elements are based on alternative approximation schemes, which may model in a more realistic way the behavior of sandwich structures under extreme loads.

Contents

List of Figures

List of Tables

Chapter 1

Introduction

1.1 Sandwich structures

A first and simple way to understand what is a sandwich structure is by analogy to an I shape beam: most of the material is placed in the flanges situated farthest from the neutral axis and only enough material is left in the connecting web to allow the flanges to work together.

A sandwich panel is indeed formed by three parts (Figure 1.1):

- two faces that are usually thin if compared to the thickness of the entire sandwich panel. The external layers confer high flexural and in-plane stiffness to the sandwich panel.
- a central core that is usually thick, light and weaker than the external faces (the core typical thickness varies between 3 mm and 60 mm)
- two adhesive layers between the sandwich external faces and the internal core.

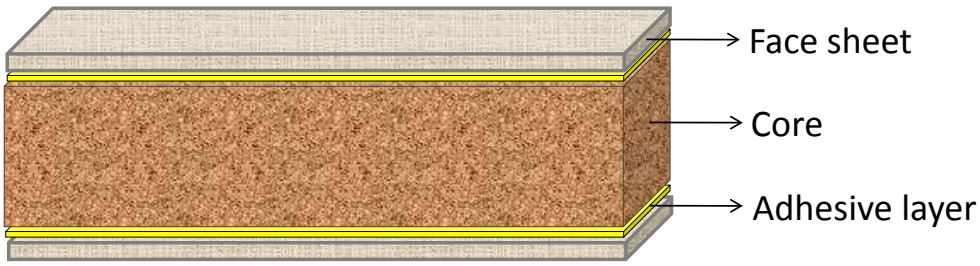

Figure 1.1: Typical cross section of a sandwich panel formed by two external face sheets and an internal core connected by adhesive layers.

The requirements for the materials forming the sandwich external faces depend on the specific structural application but the most common specifications are (Battley, 2010): high stiffness to achieve high flexural rigidity, high tensile and compressive strength, impact resistance, surface finish, environmental resistance (chemical, UV, heat, etc.), wear resistance. Composite materials, metals, wood and polymers are among the most common materials used to build the external face sheets of sandwich structures.

The properties required for the core material depend on the structural applications and vary. Typical requirements can include low density, high stiffness and strength perpendicular to the sandwich faces, energy absorption, high shear modulus and strength, thermal and acoustic insulation, thermal and chemical stabilities for manufacturing. Many different materials are currently employed in the core of sandwich panels: among these the most common are balsa wood, polymers (PVC, SAN), and metals (aluminum). Also, different core morphologies have been applied, such as: homogeneous foam core, corrugated core, honeycomb (Figure 1.2).

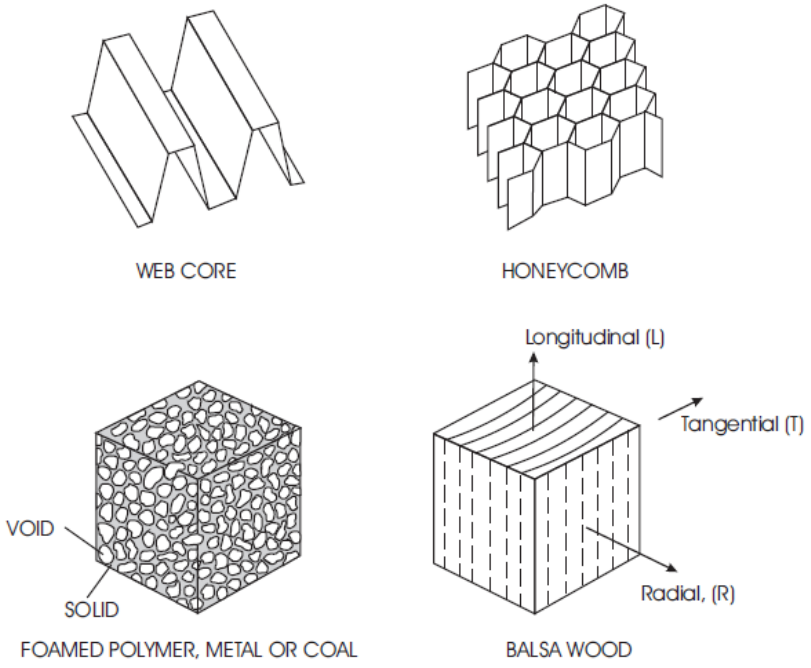

Figure 1.2: Examples of different common core types. Figure taken from Carlsson (2010).

One of the first structures in which sandwich panels were used is the De Havilland Albatross aircraft, which completed its first flight in 1937. Its fuselage was made of

plywood-balsa-plywood to decrease the airplane weight while preserving stiffness and strength. The same concepts employed in its fuselage were later used in designing the famous Mosquito bomber during World War II, and this was the first example of sandwich panel mass production (Gdoutos, 2010). From these early applications the use of sandwich structures in modern engineering grew very rapidly. Sandwich structures are today heavily employed in the military navy industry, in common and racing cars, recreational and racing sailboats, aircrafts for military and civilian purposes, wind turbines blades, space shuttle fuselage, among other applications (Figure (1.3) shows a few examples of structures in which the sandwich materials are heavily used).

Figure 1.3: Examples of modern structures that use sandwich composite materials to reduce weight and enhance performance and life span. From left to right, top to bottom, Boeing 787, Ferrari F1 2004, 61.5 m - 17.7 tons wind turbine blade, JR-Maglev high speed train (figures source: Wikimedia Commons and Thomsen (2010)).

The use of sandwich panels has improved the performance of many structures, as it has allowed the realization of larger and lighter applications. The aircraft industry is a clear example where the use of sandwich panels leads to extended lifetime and weight saving (Crump et al., in press).

The wind turbine industry is another example where fiber composite sandwich configurations are increasingly used to improve performances and to extend the limit on the di-

mension of the present wind blades (Thomsen, 2010). Present day designs mainly employ glass and carbon fiber reinforced composites, but they also include substantial amounts of sandwich materials. It is likely that even more sandwich elements may be used in future for very large blades to further reduce their weight and to provide additional buckling capacity.

The naval military and civilian industries have also been increasingly using sandwich fiber composite materials to effectively design structures that need to operate in severe environmental conditions. Sandwich material configurations are used to improve the resistance of boat hulls to cyclic operational loading (i.e., repeated wave slamming) and exceptional loads (i.e., underwater explosion). Moreover, fiber composite sandwich panels offer other advantages such as low radar and magnetic signature and are therefore ideal for building the hulls of mine hunters and combat vessels. Also, the reduced weight due to the use of sandwich composite configurations implies a higher top speed and better maneuverability.

Figure 1.4: Swedish HMS Helsingborg: its hull is constructed with a sandwich design consisting of a PVC core and vinyl external faces reinforced with carbon fibers (figure source: Wikimedia Commons).

Nowadays there are many challenges associated with the use of sandwich panels in structural applications. Among them, two seem to be of particular relevance:

- a better understanding of the behavior of sandwich structures under normal and exceptional loads is required to employ them in a safe manner. Experiments as well as simulations have a great importance in filling the gap of confidence in the use of sandwich material configurations with respect to more traditional and longer used construction materials such as steel, aluminum and concrete.

- a better understanding of the damage tolerance of sandwich structures as well as the development of methods to detect and correct the damage in operative structures (Thomsen, 2010, Hayman, 2010).

1.2 Modeling of sandwich and composite structures subjected to explosions

A material to be employed in the hull of military vessels must possess the capability to sustain explosive loads. Fiber composite materials and sandwich material configurations have been studied by many researchers as a promising possibility to sustain the load due to underwater explosions. Some authors (i.e., Tekalur et al. (2008)) studied experimentally the response of fiber composite face sheets alone subjected to blast loads. Another area of research focuses instead on studying the behavior of the complete sandwich structures subjected to explosive loads. Particular attention is dedicated to the experimental study of the effect of different core topologies and densities on the final damage and residual properties of the structure. For instance, Mouritz (1995) studied the damage in sandwich panels with foam core and fiber glass external panels with and without Kevlar thread stitches through the thickness: no relevant differences in the damage pattern were found between the stitched and unstitched panels. Wang et al. (2009) investigated the effect of varying the foam core density through the thickness (while keeping the overall weight constant) and discovered that a lighter foam layer on the side of the explosion improves the overall sandwich structure response. Kazemahvazi et al. (2010) analyzed instead a more sophisticated corrugated carbon fiber core that shows superior compressive perfor-

mance. Also very relevant to understanding the behavior of sandwich structures are the experimental campaigns conducted by Ivanez et al. (2010) and Dear et al. (2010). Ivanez et al. (2010) compared the high velocity impact response of a foam core sandwich plate and of the same structural configuration without the internal foam core (in the latter case only the external face sheets are present and there is no connection between them). Unexpectedly, the resistance of the foam core sandwich plate is only slightly higher. Dear et al. (2010) presented instead full scale experiments involving sandwich composite plates (1.3m $\times$ 1.6m) subjected to air blast. The complete set of experiments, to appear shortly in the literature, is expected to be of great value for the validation of numerical models.

A different area of research focuses on damage mechanisms that develop in the sandwich structures under explosive loads. Among others, the most important and studied failure mechanisms are core compression, shear crack formation, face sheet-core delamination, matrix and fiber cracking (i.e., Klaus and Reimerdes (2010), Wang and Shukla (2010), Espinosa et al. (2010)).

Many experimental studies are coupled with numerical simulations that, once validated using the experimental results, are employed to expand the experimental findings via parametric studies (i.e., Zhu et al. (2008, 2009), Avachat and Zhou (2010)).

Other authors prefer an analytical approach in studying the behavior of sandwich structures to explosive loads. These studies are usually restricted to two dimensional beams but provide nevertheless a detailed description of damage evolution (Cavicchi and Massab, 2010) and of the sandwich response as a function of core geometry and blast characteristics (Deshpande and Fleck, 2004).

Wider attention is given to numerical approaches such as finite element analyses since they are more flexible and easily applied to different situations. Some authors (i.e., Batra and Hasssan (2007, 2008)) studied the damage and energy absorption in fiber reinforced composites exposed to an underwater or in-air explosion. In particular fiber matrix debonding, matrix cracking and fiber breakage are considered and the energy absorbed in each failure mechanism is examined giving preliminary information on how to optimize the design of fiber composite structures to increase blast resistance. Other researchers focused on the full sandwich structure (i.e., Librescu et al. (2006, 2007)) investigating contemporaneously the effect of core and face sheet construction on the sandwich panel behavior.

Among other areas of research relevant to the study of sandwich panels subjected to explosive load, the understanding of the fluid-structure interaction is very important. The effect of cavitation reload (Xie et al., 2007), shock bubble interaction (Xie et al., 2009) and interaction between deformable bodies and multiphase flow (Young et al., 2009) are some of the aspects to be better captured during simulations.

1.3 Present research

As briefly reviewed in the previous section, many researchers have been studying in detail the behavior of sandwich and fiber composite structures subjected to underwater explosions. The damage formation and propagation in the sandwich core as well as in the fiber composite sheets have been extensively investigated together with the characterization of the overall behavior of the sandwich panels.

However there has not been much attention given to the analysis of large sandwich panels subjected to underwater and in-air explosions. Experiments regarding a full scale structure are both difficult to realize and very expensive. On the other hand, numerical analyses may be used to model the response of a full size sandwich panel after the experimental results have been used for validation and for a better understanding of the damage and failure mechanisms. The present work focuses on developing a computational method to study large size sandwich structures in a general framework without imposing restrictions on the material models to be used, on the sandwich structure geometry and on the loading conditions. Even if the same level of detail obtained in a small scale simulation may not be attained, the proposed scheme is able to capture the failure of the analyzed sandwich structure assuming that failure may be fully accounted for through fracture and fragmentation.

The description of the material models for the foam core and the external face sheets is introduced in Chapter (2) together with the cohesive law that governs fracture propagation and therefore the failure mode. Subsequently the finite element model used in the analyses of large sandwich panels is described in Chapter (3). Chapter (4) contains the verification and validation of the newly developed computational tools. The application of this computational model to foam core sandwich structures with different face sheets

is illustrated in Chapter (5). The possibility to use the presented capability to optimize the sandwich shell response to underwater explosions is also shown. Ideas for improving the efficiency and predictive capability of the code are presented in Chapter (6). As part of the future developments, two new numerical approximation schemes for shells are discussed in detail and have been further investigated outside the present research. A summary of the achieved results is finally presented in Chapter (7).

Chapter 2

Material modeling of soft core composite shells

The sandwich structure is modeled using standard shell elements and multiple integration points across the element thickness are used to capture the sandwich material configuration. Each integration point belongs to a different material layer and has assigned a correspondingly different material model. This discretization scheme across the thickness does not model phenomena such as interlayer delamination but it is able to capture the interaction between different materials in the sandwich structure. It is also very flexible, allowing to change the material arrangement across the thickness by simply modifying the material properties and material model at each integration point.
Since the work presented in this thesis is focused on the response of sandwich structures composed of fiber reinforced external layers and soft foam core, the models for these particular materials are discussed in detail in the next sections.

2.1 Material model for foam core

The material behavior of the foam core in uni-axial compression has three distinct regimes as shown in Figures (2.1) and (2.2). At low compression the foam elastically deforms with a low Young's modulus; in this stage the foam cells resist the load without collapsing. Subsequently, when a critical compressive stress is reached, the foam cells collapse and the material undergoes very large deformations at almost constant load. Figure (2.3) shows the cells' collapse process during a foam uni-axial compression test. Finally, when all the internal cells are collapsed, the foam response approaches that of the bulk material

and a high gain in stiffness is observed (Deshpande and Fleck, 2001, Patel and Finnie, 1970, Mines and Alias, 2002, Thomas et al., 2004). On the contrary, the foam response in tension may be modeled, to a good approximation, as linear elastic until fracture occurs.

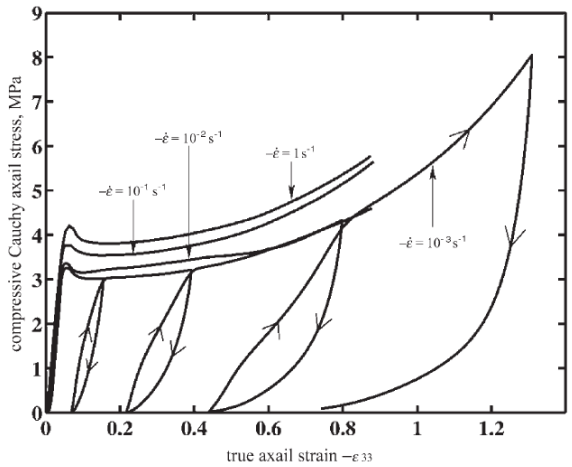

Figure 2.1: Uni-axial compression test for Divinycell H200 foam: experiment shows the three different deformation regimes for different strain rates. Figure taken from Deshpande and Fleck (2001).

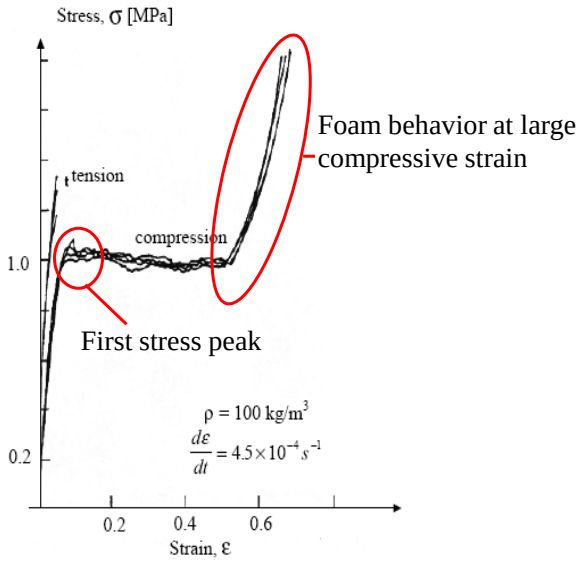

Figure 2.2: Elastic behavior of a polyurethane foam in uni-axial loading. After the first stress peak is reached, the deformation advances at roughly constant stress due to the cell collapse. The middle deformation regime is more pronounced at lower foam densities. Figure taken from Patel and Finnie (1970).

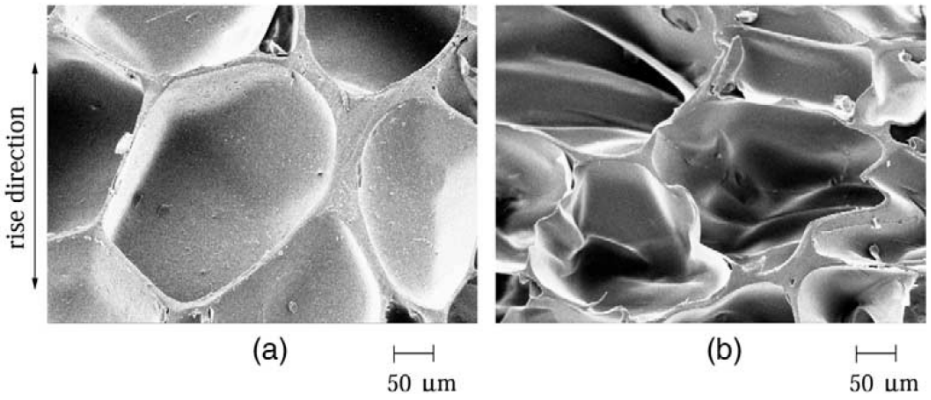

Figure 2.3: Photograph of an H200 foam specimen sectioned along its mid-plane: undeformed specimen (a) and specimen compressed uni-axially to 10% overall axial strain along the rise direction (b). The foam cells' collapse is clearly visible during the uni-axial compression test once the first stress peak has been reached. Figure taken from Deshpande and Fleck (2001).

In order to capture this complex and highly non-linear behavior of the foam, the model proposed by ElSayed et al. (2008a) was used. This constitutive model is formulated in finite kinematics and includes Ogden-type (Ogden, 1984) hyper-elasticity (able to reproduce both Neo-Hookean and Mooney-Rivlin type materials ElSayed et al. (2008a)), deviatoric and volumetric plasticity, viscosity and a different response in tension and compression. The basic equations of the model follow below. A more complete description and other applications of the model may be found in ElSayed et al. (2008a), ElSayed et al. (2008b) and ElSayed et al. (2009).

The free energy at the base of this model is given by the sum of an elasto-plastic A^{ep} and a visco-elastic A^{ve} contribution (Eq 2.1).

$$A = A^{ep}\left(\boldsymbol{F}, \boldsymbol{F}^p, \boldsymbol{Z}^p, T\right) + A^{ve}\left(\boldsymbol{F}, \boldsymbol{F}_i^v, \boldsymbol{Z}_i^v\right) = \tag{2.1}$$
$$W_e\left(\boldsymbol{F}\boldsymbol{F}^{p^{-1}}, T\right) + W_p\left(\boldsymbol{Z}^p, T\right) + \sum_{i=1}^{M}\left[W_i^e\left(\boldsymbol{F}\boldsymbol{F}_i^{v^{-1}}, T\right)\right] + \rho C_v T\left(1 - \log\frac{T}{T_0}\right)$$

where $\boldsymbol{F}$, $\boldsymbol{F}^p$, $\boldsymbol{F}^v$ are the deformation gradient, its plastic and viscous parts, respectively, where the multiplicative decomposition $\boldsymbol{F} = \boldsymbol{F}^e\boldsymbol{F}^p = \boldsymbol{F}_1^e\boldsymbol{F}_1^v = ... = \boldsymbol{F}_M^e\boldsymbol{F}_M^v$ has been used. W^e and W_i^e are the elastic strain energy densities; W^p is the plastic stored energy; T and T_0 are the current and reference temperatures; ρ is the mass density; C_v is the specific

heat at constant volume and $\boldsymbol{Z}^p$ and $\boldsymbol{Z}^v$ are internal variables related to the plastic and viscous mechanisms. The model allows for the presence of M in parallel viscous mechanisms, which may be activated depending on the complexity of the material behavior to be captured. Figure (2.4) from ElSayed et al. (2009) shows the rheological representation of the presented model consisting of an elasto-plastic mechanism and several visco-elastic mechanisms acting in parallel.

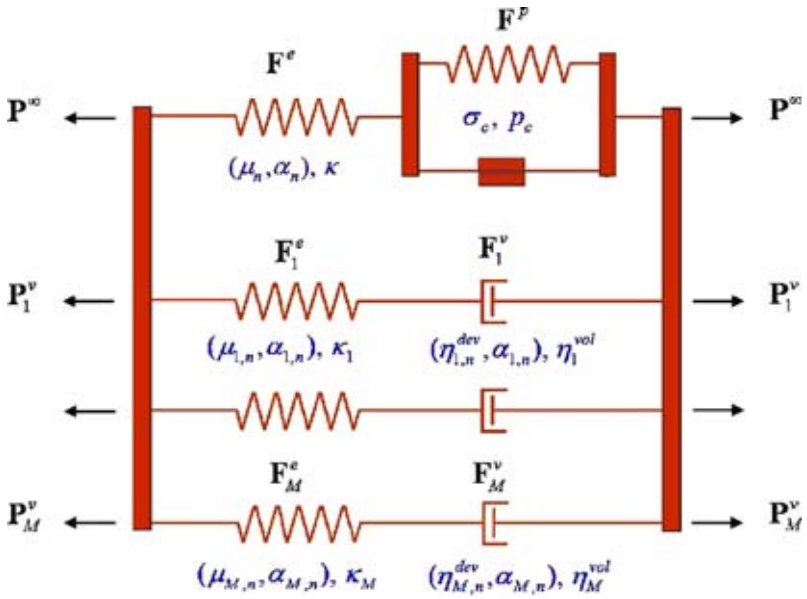

Figure 2.4: Analogy between the presented model and a 1D rheological model. Figure taken from ElSayed et al. (2009).

The first Piola-Kirchhoff stress tensor $\boldsymbol{P}$ and the thermodynamic driving forces $\boldsymbol{Y}^p$ and $\boldsymbol{Y}_i^v$ are derived from the free energy A as reported in Equations (2.2), (2.3) and (2.4).

$$\boldsymbol{P} = \frac{\partial A}{\partial \boldsymbol{F}} \tag{2.2}$$

$$\boldsymbol{Y}^p = -\frac{\partial A}{\partial \boldsymbol{Z}^p} \tag{2.3}$$

$$\boldsymbol{Y}_i^v = -\frac{\partial A}{\partial \boldsymbol{Z}_i^v} \tag{2.4}$$

The variables $\boldsymbol{F}^p$, $\boldsymbol{Z}^p$ and $\boldsymbol{F}_i^v$, $\boldsymbol{Z}_i^v$ are related to each other by the flow rules reported in ElSayed et al. (2008a) and ElSayed et al. (2008b).

The elastic, plastic and viscous energies are expressed in terms of logarithmic strains

computed from the deformation gradient $\boldsymbol{F}$ as shown in Equation (2.5).

$$\boldsymbol{\epsilon} = \frac{1}{2}\log\left(\boldsymbol{F}^T\boldsymbol{F}\right) \tag{2.5}$$

Using logarithmic strains, the elastic Ogden-type deformation energy may be written as:

$$W^e\left(e_j^e, \theta^e\right) = \sum_{j=1}^{3}\sum_{r=1}^{N}\frac{\mu_r}{\alpha_r}\left(\left[\exp\left(e_j^e\right)\right]^{\alpha_r} - 1\right) + \frac{k}{2}\left(\theta^e\right)^2 \tag{2.6}$$

where e_j^e is the j^{th} eigenvalue of the elastic logarithmic deviatoric strain, θ^e is the elastic logarithmic volumetric strain, N is the number of Ogden terms considered, μ_r and α_r are the shear moduli and the stretch exponents regarding the r Ogden function, and k is the bulk modulus.

The strain energy density W_i^e has the same structure.

The plastic stored energy has the form:

$$W^p\left(e^p, \theta^p\right) = \frac{n\sigma_0 e_0^p}{n+1}\left(1 + \frac{e^p}{e_0^p}\right)^{\frac{n+1}{n}} + \frac{n\sigma_0 e_0^p}{n+1}N_v\frac{4\pi a^3}{3}g\left(\theta^p, n\right) \tag{2.7}$$

where σ_0 is the yield stress, e_0^p is the reference plastic strain, e^p is the effective deviatoric plastic strain, n is the hardening exponent, N_v is the void density per unit undeformed volume, a is the void radius, θ_p is the effective volumetric plastic strain. The first term on the RHS of Equation (2.7) represents the deviatoric part of the plastic energy density whereas the second term represents the volumetric contribution. The function $g\left(\theta^p, n\right)$ (Equation 2.8) describes the volumetric plastic behavior due to the expansion or collapse of spherical voids.

$$g\left(\theta^p, n\right) = \int_1^{\frac{1}{f}}\left(1 + \frac{2}{3\epsilon_0^p}\log\frac{\xi}{\xi - 1 + \frac{f_0}{f_0\exp\theta^p - 1}}\right)^{\frac{n+1}{n}} d\xi \tag{2.8}$$

where f_0 and f are, respectively, the initial and current void volume fractions.

2.1.1 Validation

Given a set of experimental data, the material model discussed in the previous section has been calibrated using genetic algorithms as presented in ElSayed et al. (2008a) and

ElSayed (2008). The problem of finding the material parameters required for the presented foam material model is highly non-linear and may have many different minima. Genetic algorithms have proved to be very efficient in solving this type of problem. Figure (2.5) and Figure (2.6) show the agreement between the experimental material behavior and the calibrated material model during uni-axial compression and tension tests. The chosen material model captures well the three distinct deformation stages during the foam compression test.

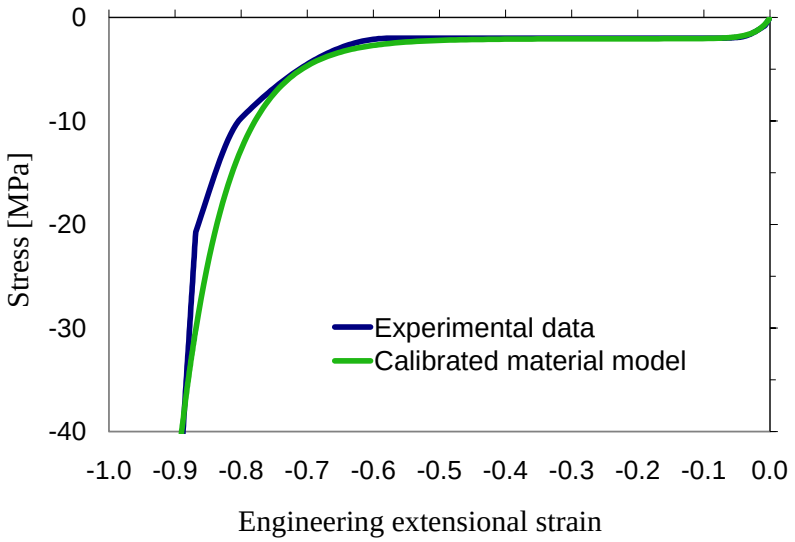

Figure 2.5: Experimental and numerical uni-axial response of PVC foam H100 under uni-axial compression.

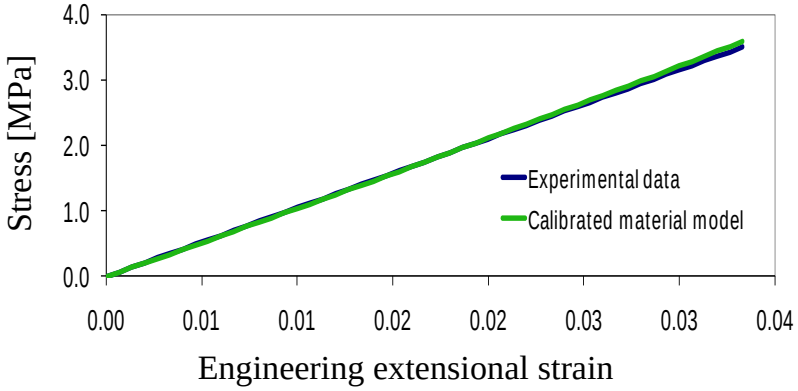

Figure 2.6: Experimental and numerical uni-axial response of PVC foam H100 under uni-axial tension.

2.2 Material model for the external fiber reinforced layers

The new fiber reinforced material model used in the analyses is formulated in finite kinematics as large deformations are expected when a sandwich shell is subjected to explosive loading. The energy density function of this model is composed of two parts: the energy density due to the matrix and the energy density due to the fibers.

$$W\left(\boldsymbol{F}\right) = v_{ep} W_{ep}\left(\boldsymbol{F}\right) + \sum_{i=1}^{nf} v_{fr}^{i} W_{fr}^{i}\left(\boldsymbol{F}\right) \tag{2.9}$$

In Equation (2.9) $W\left(\boldsymbol{F}\right)$ is the total energy density, a function of the deformation gradient $\boldsymbol{F}$. v_{ep} and v_{fr}^{i} are, respectively, the volume fraction of the matrix and that of the i^{th} group of fibers, while $W_{ep}\left(\boldsymbol{F}\right)$ and $W_{fr}^{i}\left(\boldsymbol{F}\right)$ are the energy density of the matrix and of the i^{th} group of fibers. As seen in Equation (2.9) the proposed model allows for the presence of nf different groups of fibers with different material properties and orientation.
The matrix material behavior is captured using a compressible Neo-Hookean material model. The expression of its energy density is written in Equation (2.10) where μ and λ are the Lamé material constants:

$$W_{ep}\left(\boldsymbol{F}\right) = \frac{\mu}{2}\left(tr\left(\boldsymbol{F}^{T}\boldsymbol{F}\right) - 3\right) + \frac{\lambda}{2}\left(\log\left(det\left(\boldsymbol{F}\right)\right)\right)^{2} - \mu \log\left(det\left(\boldsymbol{F}\right)\right) \tag{2.10}$$

The fiber contribution to the total energy density is due to the fiber deformation along its own axis. This contribution is captured in Equation (2.11) where $\boldsymbol{N}_i$ and E_{fr}^{i} are, respectively, the fiber direction and Young's modulus:

$$W_{fr}^{i}\left(\boldsymbol{F}\right) = \frac{1}{2} E_{fr}^{i} \left(\log \sqrt{\boldsymbol{N}_{i}^{T}\boldsymbol{F}^{T}\boldsymbol{F}\boldsymbol{N}_{i}}\right)^{2} \tag{2.11}$$

It is important to note that to correctly describe the response of fiber composite materials using the presented model, the material properties of the matrix must be adjusted to consider the presence of the fibers and represent correctly the stiffer response of the matrix itself. Similar observations are common to other fiber reinforced material models used, for instance, in bio-mechanics (Pandolfi and Manganiello, 2006, Pandolfi and Holzapfel,

2008).

2.2.1 Validation

The simple model presented in Section (2.2) requires only a few parameters: the Lamé constants of the matrix and the Young's modulus of each set of fibers. As mentioned above, the Lamé constants of the matrix need to be calibrated in order to take into account the presence of the fibers and to represent the isotropic part of the response of the matrix and fibers ensemble. The calibration of these two material constants may be performed starting from uni-axial tension tests of fiber reinforced specimens in which the direction of the load varies with respect to the direction of the fibers.
Figure (2.7) shows a comparison between the experimental data of Yokozeki et al. (2007) and the presented model. Once the material properties of the matrix are calibrated using these experimental data, the model captures well the material response under different loading directions with respect to the fiber orientation.

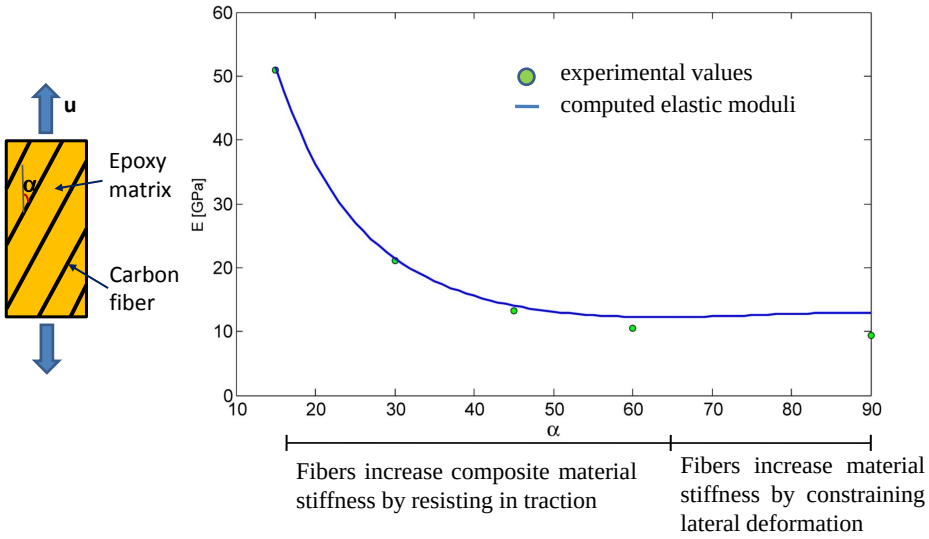

Figure 2.7: Comparison between experimental and computed initial elastic moduli obtained in uni-axial tensile tests with different load/fiber orientation.

Using the material properties corresponding to the fiber reinforced material tested in Yokozeki et al. (2007), two basic numerical experiments are carried out. First the response in uni-axial tension is analyzed as a function of the angle α between the load and the fiber direction. As seen in Figure (2.8) and confirmed in Figure (2.7), the more the load

is aligned with the fiber direction, the stiffer the material response is in general. However the fiber contribution is minimal for an angle α roughly equal to $\pi/3$ when a different mechanism is activated to carry the load. Indeed for angles α between $\pi/3$ and $\pi/2$ the fibers' contribution to load bearing is through resisting the lateral deformation of the specimen (the specimen loaded in the longitudinal direction tends to contract laterally due to the Poisson effect). In order to better understand this aspect, a second numerical uni-axial tension test is performed where the fiber direction is constant and at $\pi/2$ with respect to the load direction. As shown in Figure (2.9) the response of the material is stiffer with a greater Poisson ratio of the matrix and therefore when the ratio between lateral and longitudinal deformations is larger. A larger lateral deformation per unit longitudinal load corresponds to a larger fiber deformation, which thus can better help to sustain the load. During this second numerical test only the matrix Poisson ratio is varied and all the other material properties are kept constant.

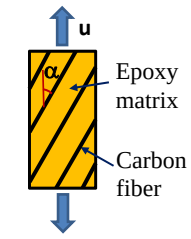

Material Properties	
ν_{matrix}	0.43
E_{matrix} [MPa]	2.85E+04
ν_{matrix}	0.25
ν_{fr}	0.57
E_{fiber} [MPa]	2.10E+05

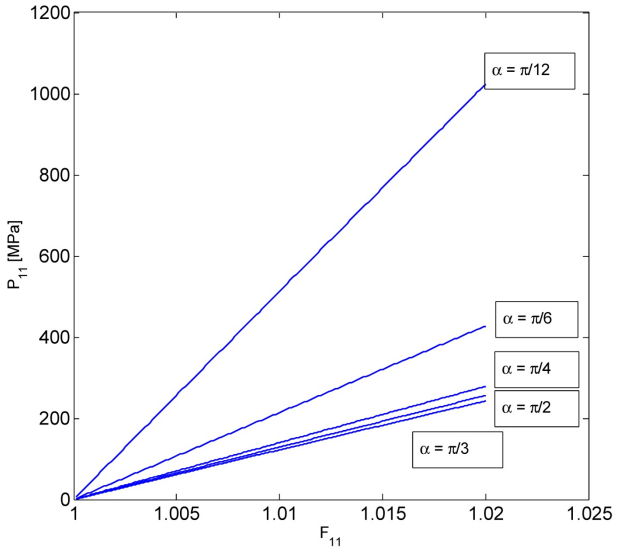

Figure 2.8: Response of epoxy matrix reinforced with carbon fibers under uni-axial tension: dependence on load/fiber angle.

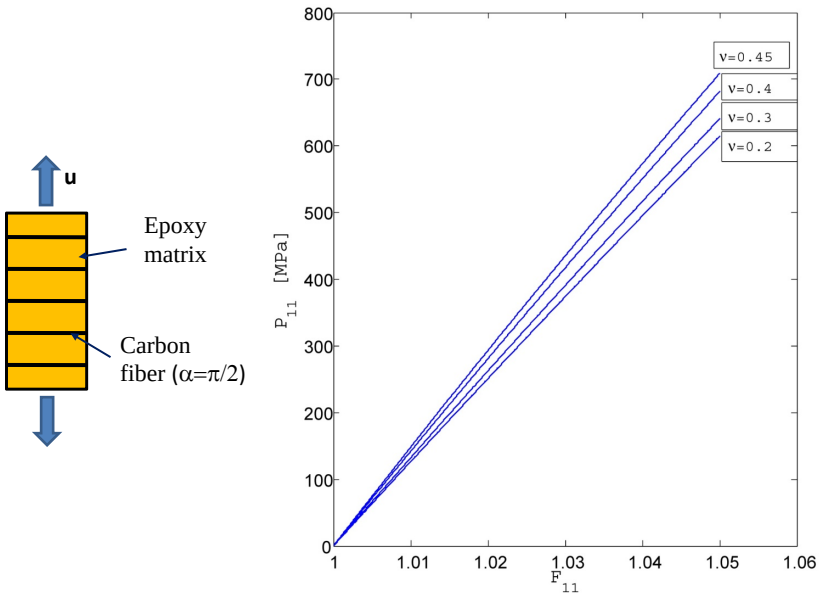

Figure 2.9: Response of fiber (carbon) reinforced epoxy loaded orthogonally to the fiber direction during an uni-axial tension test: dependence on matrix Poisson ratio.

2.3 Cohesive model

In order to describe the fracture propagation in the foam core we use the isotropic cohesive model developed by Camacho and Ortiz (1996) and Ortiz and Pandolfi (1999). According to this cohesive model the fracture formation is a gradual process and is governed by a cohesive potential $\Phi(\delta, \boldsymbol{q})$, which is a function of an effective opening displacement δ and of a suitable set of internal variables $\boldsymbol{q}$. The definition of the potential Φ as a function of δ and $\boldsymbol{q}$ only assumes that the cohesive response of the material is independent of the stretching and shearing of the cohesive surface as well as of the direction of sliding (Ortiz and Pandolfi, 1999).

The effective opening displacement δ is computed as:

$$\delta = \sqrt{\beta^2 \delta_s^2 + \delta_n^2} \tag{2.12}$$

where

$$\delta_n = \boldsymbol{\delta} \cdot \boldsymbol{n} \tag{2.13}$$

$$\delta_s = \|\boldsymbol{\delta} - \delta_n \boldsymbol{n}\| \tag{2.14}$$

and $\boldsymbol{n}$ is the normal to the fracture surface, $\boldsymbol{\delta} = [|\boldsymbol{u}|]$ is the opening displacement and β is the shear to normal cohesive strength ratio, which therefore accounts for mode coupling during the fracture process. The parameter β can be also understood as the ratio between mode II and mode I fracture toughness of the material (Yu et al., 2002).

Ortiz and Pandolfi (1999) also showed that the cohesive traction $\boldsymbol{T}$, which is the conjugate stress measure of the opening displacement $\boldsymbol{\delta}$, is given by:

$$\boldsymbol{T} = \frac{\partial \Phi}{\partial \boldsymbol{\delta}} = \frac{T}{\delta} \left(\beta^2 \boldsymbol{\delta}_s + \delta_n \boldsymbol{n} \right) \tag{2.15}$$

where:

$$T = \frac{\partial \Phi}{\partial \delta} \tag{2.16}$$

The form of the cohesive law assumed in the present research is shown in Figure (2.10); no opening displacement is present until the cohesive strength σ_c is reached. Subsequently, the cohesive tractions decrease linearly to reach zero at $\delta = \delta_c$. Assuming a linear cohesive law, the critical opening displacement δ_c is computed from the mode-I fracture energy density G_c and the cohesive strength σ_c of the material as $\delta_c = \frac{2G_c}{\sigma_c}$.

The irreversibility of the cohesive law is achieved by defining the unloading path toward the origin from the envelope shown in Figure (2.10). The unloading/reloading process is characterized by $\delta < \delta_{max}$ or by $\delta = \delta_{max}$ and $\dot{\delta} < 0$. The scalar effective traction T during unloading/reloading is given by $T = \frac{T_{max}}{\delta_{max}} \delta$.

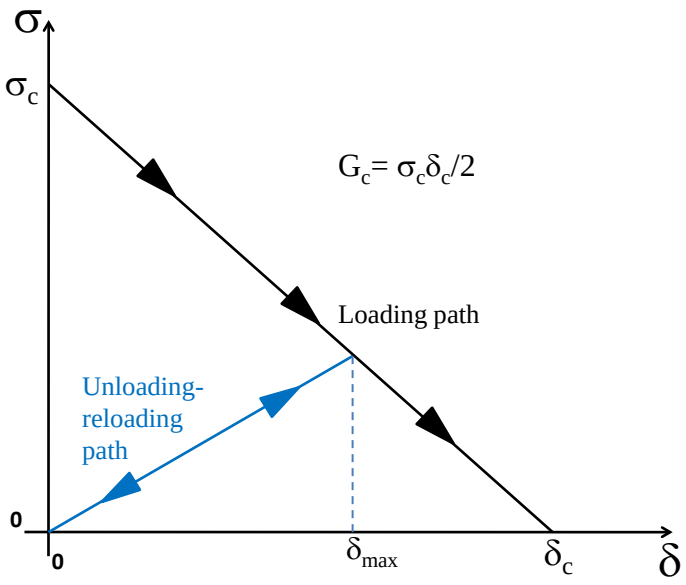

Figure 2.10: Linearly decreasing cohesive law with loading-unloading rules. Another convenient form of the cohesive law is given by Smith and Ferrante and is reported in Ortiz and Pandolfi (1999).

This isotropic model has been adapted by Yu et al. (2002) to describe cohesive fracture propagation in anisotropic fiber reinforced materials. They redefine the cohesive strength σ_c to account for the difference between the direction of the fibers and the direction of fracture propagation. If the fracture propagates along the fibers' direction, the fibers do not increase the strength of the isotropic matrix, but if the fracture propagates normal to the direction of the fibers they greatly increase the cohesive strength of the composite material and consequently its fracture energy. We slightly modify the expression for σ_c proposed in Yu et al. (2002) in order to account for multiple fiber directions to be:

$$\sigma_c = v_{ep}\sigma_{c_{ep}} + \sum_{i=1}^{nf} v_{fr}^i \sigma_{c_{fr}}^i \cos^2\left(\alpha^i\right) \tag{2.17}$$

where $\sigma_{c_{ep}}$ is the cohesive strength of the composite matrix, $\sigma_{c_{fr}}^i$ is the tensile strength of the i^{th} fiber group, and α is the angle between the fiber direction and the normal $\boldsymbol{n}$ to the fracture surface.

Chapter 3

Numerical modeling of composite shells subjected to underwater explosions

In this chapter the shell finite element model for thin sandwich structures is presented together with two strategies to apply the load due to an underwater explosion: a prescribed pressure profile and a full fluid-solid coupled simulation.

3.1 Numerical modeling of sandwich structures

In the literature it is possible to find many alternative approaches for modeling the behavior of sandwich composite shells. Approaches range from analytical studies to different levels of numerical discretizations. Although able to provide complete solutions, analytical methods are usually limited to specific cases by the assumptions under which they are derived (Li et al., 2000a). In view of practical applications that involve different scenarios, including the interaction with fluids, finite element shells are chosen here, since they represent one of the most versatile approaches. Within the known finite element approximations, some authors (i.e., Moreira et al. (2010), Tan and Vu-Quoc (2005)) model each layer of the sandwich shell with a different set of shell elements. These approaches are very flexible, since each material layer is modeled independently; there is no constraint on the number of layers included, and multilayer plates with ply drop-offs may be modeled. However, they are computationally very expensive. As an alternative, other authors (i.e., Han et al. (2008), Jeung and Shen (2001)) include different material layers in a unique element, and evaluate the global shell properties by integrating different material proper-

ties across the shell thickness. The method adopted in the present research, as described in Section (3.1.2), falls in the latter category.

It is worth mentioning that more sophisticated approaches take a microstructural point of view, by considering both distinct material layers and higher order shell theories. Thus they are able to describe the displacement field across the thickness in a more realistic way (i.e., Tabiei and Tanov (2002), Vu-Quoc et al. (2000), Yong and Cho (1995), Millikarjuna and Kant (1992)). A further extension of high order theory shell elements can be found in Sulmoni et al. (2008), where an additional "zig-zag" degree of freedom is introduced to enhance the displacement field across the thickness and improve the description of strains and stresses. Although such models contain many important features that render them more realistic, they require a large number of degrees of freedom per node, which makes them very costly from a computational point of view. Moreover, there is usually no guarantee that such finite elements converge properly in the limit of the thin shells, since they do not satisfy the inf-sup condition (Brezzi and Fortin, 1991).

In the present investigation, the nonlocal shell finite element developed by Cirak et al. (2000) has been adapted to the sandwich shell structure. The nonlocal shell approach is computationally efficient and flexible regarding the insertion of different material layers; it guarantees convergence in the thin limit, it can use linearized as well as finite kinematics, and it can be enriched with inter-element cohesive elements to model fracture propagation across the thickness. Regrettably, the displacement field across the thickness cannot be modeled as accurately as when higher order shell theories or "zig-zag" displacement terms are employed.

An important remark is necessary concerning the assumption of the Kirchhoff-Love kinematic hypothesis used in this study, which assumes that plane sections remain plane after deformation. The choice made here is mainly dictated by the need to model wide sandwich panels, characterized by a high length to thickness ratio, undergoing extreme loading due to explosions. The panel is designed in such a way that the internal and the external faces work together in sustaining the external load. Under impulsive conditions that lead to the rupture of the structure, the actual kinematics of the deformations across the thickness appear to be of minor relevance with respect to the global response of the system. In the present study, the choice of the nonlocal shell finite elements allows limiting substantially

(by more than 60%) the number of degrees of freedom per node with respect to richer kinematics models. The reduced computational effort is crucial for analyses that include fracture and fragmentation. It is clear that for alternative applications, e.g., to study the dissipative properties of the soft core with respect to standard impacts, the Kirchhoff-Love kinematic hypothesis needs to be replaced with a more realistic assumption.

3.1.1 Subdivision shell finite elements

The core of the shell finite element approximation scheme used in the analyses has been developed and described in Cirak et al. (2000), Cirak and Ortiz (2001) and Cirak et al. (2005). This section offers a brief description of this approximation scheme including the hypotheses and main advantages that motivated its use.

The finite element for thin shells developed by Cirak et al. (2000) obeys Kirchhoff-Love theory and is based on subdivision surfaces that are used to describe the shell geometry in the undeformed and deformed configurations. The motivation behind the use of subdivision surfaces resides in the nature of Kirchhoff-Love energy for thin shells, which contains the first and second derivatives of the displacement field. Therefore, in order to ensure that the shell internal energy is bounded, the interpolant for the displacements must have square integrable second derivatives or, in other words, the interpolation function must belong to H^2 giving rise to C^1 finite elements. Subdivision surfaces satisfy this requirement and therefore are optimal to model the shell deformation process.

3.1.1.1 Brief description of subdivision surfaces

Subdivision surfaces are smooth surfaces constructed through repeated refinement of an initial control mesh. During a subdivision step new vertices are added to the previous mesh. The present method is based on a triangular mesh and each triangle is quadrisected during a refinement (or subdivision) step. The nodal positions of the newly created vertices are computed by a weighted average of the nodal coordinates of the already existing vertices. If during a subdivision step only the nodal coordinates of the new vertices are computed, the subdivision scheme is called an *interpolating scheme*. On the other hand, if all the vertices' nodal positions are recomputed following a subdivision step, the scheme is called an *approximating scheme*. Consequently, an approximating

scheme does not interpolate the nodal positions of the initial or control mesh but only approximates them. However, only an approximating scheme produces limit surfaces that have square integrable curvatures as required to be used in the analysis of thin shells obeying Kirchhoff-Love theory. The approximation scheme adopted by Cirak et al. (2000) is the Loop scheme, which has been developed for triangular meshes.

As opposed to classic finite elements, the interpolation functions derived from subdivision schemes are non-local. Therefore the value of a function to be evaluated inside a triangular element of the mesh (i.e., at a quadrature point) does not depend only on the nodal quantities of the considered triangle but also on the nodal values of other elements in the mesh. However, if the vertices of a triangular element are all regular [1], then the value of a function inside that element depends only on the nodal values in the $1-ring$ [2] of elements around the considered triangle (Figure 3.1). Indeed the interpolation function derived from Loop's subdivision scheme over a regular triangle [3] coincides exactly with a quartic box-spline described by 12 basis, or shape, functions.

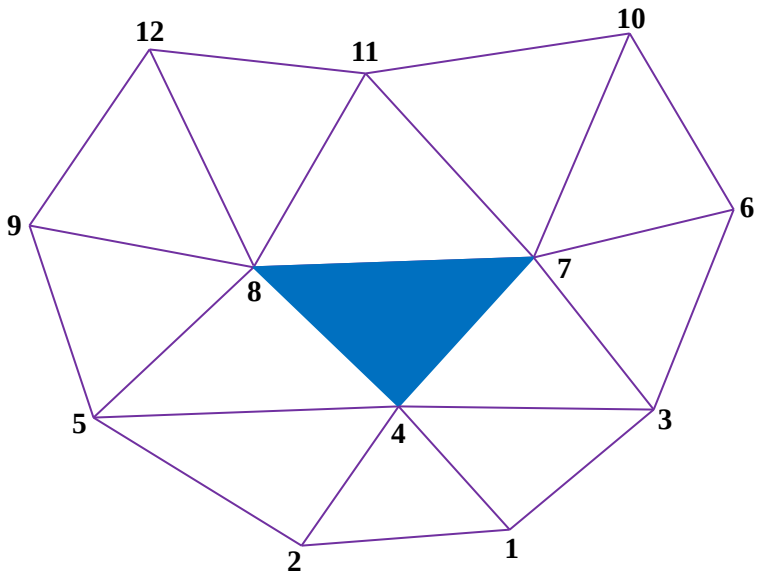

Figure 3.1: Regular patch for the solid filled triangular element. The displacement field inside the solid filled triangle is determined only by the nodal values of the 12 vertices represented above. Figure adapted from Cirak et al. (2000).

[1] A vertex is regular if the number of edges incident on it is equal to 6.
[2] 1-ring of an element is defined as the set of elements incident on the considered element.
[3] A triangle is regular if all its vertices are regular.

Inside each regular triangle the limiting surface in the reference or deformed configuration may be approximated as:

$$\bar{\boldsymbol{x}}\left(\theta^1,\theta^2\right)=\sum_{I=1}^{12}N^I\left(\theta^1,\theta^2\right)\bar{\boldsymbol{x}}_I \tag{3.1}$$

$$\boldsymbol{x}\left(\theta^1,\theta^2\right)=\sum_{I=1}^{12}N^I\left(\theta^1,\theta^2\right)\boldsymbol{x}_I \tag{3.2}$$

where θ^1 and θ^2 are local barycentric coordinates that span each triangular element, N^I is the basis shape function at node I, $\bar{\boldsymbol{x}}_I$ and $\boldsymbol{x}_I$ are, respectively, the nodal coordinates of node I in the reference and deformed configuration. (Analytical expressions for the basis functions N^I may be found in Cirak et al. (2000)).

If the function of interest must be evaluated at a location that does not reside inside a regular element, then the mesh has to be subdivided until such location resides inside a regular triangle. To this extent, any mesh to be used in the present finite element scheme is subdivided once a priori in order to separate all the irregular vertices. Following this first subdivision step, all the triangles in the mesh contain at most one irregular vertex. Since only one surface Gauss integration point is used per triangular element, only one further subdivision step is necessary to evaluate the field of interest inside an irregular element. Indeed, after this second subdivision step, each Gauss point which was at the center of an irregular triangle will reside on the edge of a regular triangle.

It is important to mention that, even if the interpolation scheme deriving from subdivision surfaces is non-local, the displacement field and the shell limit surface defined over overlapping patches of elements are defined unequivocally.

Given the non-locality of the interpolation functions, ghost nodes are necessary at the shell boundary in order to apply Dirichlet-type boundary conditions.

3.1.1.2 Shell kinematics and equilibrium equations

The Kirchhoff-Love kinematic ansatz for shell theory is expressed with the following equations:

$$\bar{\boldsymbol{\varphi}}\left(\theta^1,\theta^2,\theta^3\right) = \bar{\boldsymbol{x}}\left(\theta^1,\theta^2\right) + \theta^3\bar{\boldsymbol{a}}_3\left(\theta^1,\theta^2\right) \qquad -\frac{\bar{h}}{2} \leq \theta^3 \leq \frac{\bar{h}}{2} \tag{3.3}$$

$$\boldsymbol{\varphi}\left(\theta^1,\theta^2,\theta^3\right) = \boldsymbol{x}\left(\theta^1,\theta^2\right) + \theta^3\lambda\left(\theta^1,\theta^2\right)\boldsymbol{a}_3\left(\theta^1,\theta^2\right) \qquad -\frac{\bar{h}}{2} \leq \theta^3 \leq \frac{\bar{h}}{2} \tag{3.4}$$

where $(\theta^1,\theta^2,\theta^3)$ are the curvilinear coordinates that describe the shell domain. θ^1 and θ^2 span the shell middle surface while θ^3 identifies the position along the normal to the middle surface. $\bar{\boldsymbol{\varphi}}\left(\theta^1,\theta^2,\theta^3\right)$ is the position of the material point identified by the curvilinear coordinates $(\theta^1,\theta^2,\theta^3)$ in the shell reference configuration. Correspondingly, $\boldsymbol{\varphi}\left(\theta^1,\theta^2,\theta^3\right)$ is the material point position in the deformed shell configuration. $\bar{\boldsymbol{x}}\left(\theta^1,\theta^2\right)$ and $\boldsymbol{x}\left(\theta^1,\theta^2\right)$ represent the shell middle surface in the undeformed and deformed configuration, respectively. λ is the thickness stretch and is equal to the ratio between the current shell thickness h and the undeformed shell thickness $\bar{h}$ $\left(\lambda = \frac{h}{\bar{h}}\right)$.

The shell directors $\bar{\boldsymbol{a}}_3$ and $\boldsymbol{a}_3$ in the undeformed and deformed configuration are given by:

$$\bar{\boldsymbol{a}}_3 = \frac{\bar{\boldsymbol{a}}_1 \times \bar{\boldsymbol{a}}_2}{\|\bar{\boldsymbol{a}}_1 \times \bar{\boldsymbol{a}}_2\|} \qquad\qquad \boldsymbol{a}_3 = \frac{\boldsymbol{a}_1 \times \boldsymbol{a}_2}{\|\boldsymbol{a}_1 \times \boldsymbol{a}_2\|} \tag{3.5}$$

where the surface basis vectors $\bar{\boldsymbol{a}}_\alpha$ and $\boldsymbol{a}_\alpha$ are:

$$\bar{\boldsymbol{a}}_\alpha = \bar{\boldsymbol{x}}_{,\alpha} \qquad\qquad \boldsymbol{a}_\alpha = \boldsymbol{x}_{,\alpha} \tag{3.6}$$

Greek indices α and β assume values 1 and 2. As described in Equation (3.4) and Equation (3.5) the shell sections remain plane and normal to the shell middle surface during the deformation process (Kirchhoff-Love kinematic ansatz).

The covariant basis vectors needed to derive the deformation gradient $\boldsymbol{F}$ may now be

computed as:

$$\bar{\boldsymbol{g}}_\alpha = \frac{\partial \bar{\boldsymbol{\varphi}}}{\partial \theta^\alpha} = \frac{\partial \bar{\boldsymbol{x}}}{\partial \theta^\alpha} + \theta^3 \frac{\partial \bar{\boldsymbol{a}}_3}{\partial \theta^\alpha} = \bar{\boldsymbol{a}}_\alpha + \theta^3 \bar{\boldsymbol{a}}_{3,\alpha} \tag{3.7}$$

$$\bar{\boldsymbol{g}}_3 = \frac{\partial \bar{\boldsymbol{\varphi}}}{\partial \theta^3} = \bar{\boldsymbol{a}}_3 \tag{3.8}$$

$$\boldsymbol{g}_\alpha = \frac{\partial \boldsymbol{\varphi}}{\partial \theta^\alpha} = \frac{\partial \boldsymbol{x}}{\partial \theta^\alpha} + \theta^3 \frac{\partial \left(\lambda \boldsymbol{a}_3\right)}{\partial \theta^\alpha} = \boldsymbol{a}_\alpha + \theta^3 \left(\lambda \boldsymbol{a}_3\right)_{,\alpha} \tag{3.9}$$

$$\boldsymbol{g}_3 = \frac{\partial \boldsymbol{\varphi}}{\partial \theta^3} = \lambda \boldsymbol{a}_3 \tag{3.10}$$

The controvariant basis vectors follow from the relations:

$$\bar{\boldsymbol{g}}^i \cdot \bar{\boldsymbol{g}}_j = \delta^i_j \qquad\qquad \boldsymbol{g}^i \cdot \boldsymbol{g}_j = \delta^i_j \tag{3.11}$$

where δ^i_j is the Kronecker delta. The deformation gradient $\boldsymbol{F}$ is finally expressed as a function of the controvariant basis vectors:

$$\boldsymbol{F} = \frac{\partial \boldsymbol{\varphi}}{\partial \bar{\boldsymbol{\varphi}}} = \frac{\partial \boldsymbol{\varphi}}{\partial \theta^i} \otimes \bar{\boldsymbol{g}}^i = \tag{3.12}$$

$$= \left[\boldsymbol{a}_\alpha + \theta^3 \left(\lambda \boldsymbol{a}_3\right)_{,\alpha}\right] \otimes \bar{\boldsymbol{g}}^\alpha + \lambda \boldsymbol{a}_3 \otimes \bar{\boldsymbol{g}}^3 \tag{3.13}$$

The deformation gradient $\boldsymbol{F}$ is necessary to evaluate the internal part of the potential energy of the shell:

$$\Pi_{int}\left[\boldsymbol{\varphi}\right] = \int_{\bar{\Omega}} \int_{-\frac{\bar{h}}{2}}^{\frac{\bar{h}}{2}} W\left(\boldsymbol{F}\right) \mu d\theta^3 d\bar{\Omega} \tag{3.14}$$

where $\bar{\Omega}$ and $\bar{h}$ are respectively the shell middle surface and the shell thickness in the undeformed configuration, $W\left(\boldsymbol{F}\right)$ is the strain energy density per unit undeformed volume and μ (Equation 3.15) accounts for the curvature in computing the shell volume.

$$\mu = \frac{\left|\left(\bar{\boldsymbol{g}}_1 \times \bar{\boldsymbol{g}}_2\right) \cdot \bar{\boldsymbol{g}}_3\right|}{\left|\left(\bar{\boldsymbol{a}}_1 \times \bar{\boldsymbol{a}}_2\right) \cdot \bar{\boldsymbol{a}}_3\right|} \tag{3.15}$$

If only distributed loads $\boldsymbol{q}$ per unit area and axial forces $\boldsymbol{N}$ per unit length are considered, the external part of the potential energy may be written as:

$$\Pi_{ext}\left[\boldsymbol{u}\right] = -\int_{\bar{\Omega}} \boldsymbol{q} \cdot \boldsymbol{u} d\bar{\Omega} - \int_{\bar{\Gamma}} \boldsymbol{N} \cdot \boldsymbol{u} d\bar{\Gamma} \tag{3.16}$$

where $\bar{\Gamma} = \partial\bar{\Omega}$, $\boldsymbol{u} = \boldsymbol{x} - \bar{\boldsymbol{x}}$ and it has been assumed that the loads are applied to the shell middle surface ($\theta^3 = 0$).

If no inertial or cohesive forces are present, the shell equilibrium configuration corresponds to a stationary point of the shell potential energy $\Pi_{shell} = \Pi_{int} + \Pi_{ext}$ over the space of all admissible configurations V, i.e.,

$$\delta\Pi_{shell} = \delta\Pi_{int} + \delta\Pi_{ext} = 0 \tag{3.17}$$

Equation (3.17) is also a statement of the principle of virtual work.

In a dynamical problem, the equilibrium Equation (3.17) is augmented by the addition of the virtual kinetic work:

$$\delta\Pi_{kin}\left[\boldsymbol{\varphi}\right] = \int_{\bar{\Omega}} \int_{-\frac{\bar{h}}{2}}^{\frac{\bar{h}}{2}} \bar{\rho}\ddot{\boldsymbol{\varphi}} \cdot \delta\boldsymbol{\varphi}\mu d\theta^3 d\bar{\Omega} \tag{3.18}$$

The equilibrium equation in a dynamical problem is therefore:

$$\delta\Pi_{int} + \delta\Pi_{ext} + \delta\Pi_{kin} = 0 \tag{3.19}$$

Equation (3.19) is the basis on which to construct the finite element approximation once the space of admissible shell configurations V is determined. In the discretized setting of the finite element approach, the space V_d is given by:

$$\boldsymbol{x}_d\left(\theta^1, \theta^2\right) = \sum_{I=1}^{NP} N^I\left(\theta^1, \theta^2\right) \boldsymbol{x}_I \tag{3.20}$$

where d characterizes the size of the finite element mesh, NP is the number of all the nodes in the mesh, N^I is the node I shape function and $\boldsymbol{x}_I$ is the shell middle surface position at node I. In the present context, N^I are computed using the subdivision surface technique described in Section (3.1.1.1) and therefore belong to H^2. As a consequence of the Kirchhoff-Love kinematic ansatz, the equilibrium Equation (3.19) may be expressed in terms only of the position $\boldsymbol{x}\left(\theta^1, \theta^2\right)$ of the shell middle surface.

Introducing Equation (3.20) into the weak form expressed symbolically in Equation (3.19)

the classical system of equations to be solved in a finite element program is obtained:

$$\boldsymbol{M}_d \ddot{\boldsymbol{x}}_d + \boldsymbol{f}_d^{int}\left(\boldsymbol{x}_d\right) = \boldsymbol{f}_d^{ext}\left(t\right) \tag{3.21}$$

where $\boldsymbol{M}_d$ is the mass matrix (in the numerical simulations $\boldsymbol{M}_d$ is lumped through the row-sum procedure), $\boldsymbol{f}_d^{int}$ is the internal force vector, $\boldsymbol{f}_d^{ext}\left(t\right)$ is the external force vector and t represents time. Each term in the discrete Equation (3.21) is computed by using one surface Gauss quadrature point per triangular element and Simpson's rule across the thickness. The time discretization of Equation (3.21) is obtained by recourse to the Explicit Newmark scheme (Hughes, 2000).

Additionally, the plane stress condition is enforced, since the presented finite element method is developed for thin shells. Enforcing the plane stress condition is equivalent to requiring that the stress τ^{33} normal to the shell middle surface in the deformed configuration is equal to zero as shown in Equation (3.22):

$$\tau^{33} = 2\frac{\partial W}{\partial g_{33}} = 0 \tag{3.22}$$

where $\boldsymbol{\tau} = \boldsymbol{P}\boldsymbol{F}^T$ is the Kirchhoff stress tensor, and its components are expressed in the deformed covariant basis ($\boldsymbol{\tau} = \tau^{ij}\boldsymbol{g}_i \otimes \boldsymbol{g}_j$). Equation (3.22) may efficiently be imposed at the constitutive level where the value of g_{33} is evaluated using a Newton-Raphson iterative scheme. The current thickness of the shell may then be computed as a consequence of imposing the plane stress condition:

$$h = \int_{-\frac{\bar{h}}{2}}^{\frac{\bar{h}}{2}} \sqrt{g_{33}} d\theta^3 \tag{3.23}$$

If incompressible materials are considered, the shell thickness in the deformed configuration derives immediately from the incompressibility condition, and the plane stress condition is imposed through computation of the correct pressure p, a priori unknown when incompressible materials are used.

3.1.1.3 Final remarks

The only degrees of freedom in the shell finite element described in Sections (3.1.1.1) and (3.1.1.2) are nodal displacements. This aspect greatly simplifies the use of this element in finite kinematics since no rotation degrees of freedom are present.

In general, for an unstructured mesh and an arbitrary geometry, it is not possible to construct a C^1 conforming finite element discretization when polynomial shape functions are used and only displacement and displacement first derivatives are defined at the mesh nodes. In contrast, the shell finite element described here possesses H^2 shape functions and does not require displacement first derivatives to be defined as unknown at the element nodes. Moreover, the subdivision surface shell element may be used with any shell geometry and may be constructed based on a general triangulation of the analysis domain. The low order quadrature rule required for optimal convergence (only one surface Gauss point per triangular element) makes the element very attractive from a computational point of view.

Finally, the chosen element has been extensively validated in linearized kinematics (through the challenging Belytschko obstacle course, Cirak et al. (2000)), in finite kinematics simulating the inflation of a spherical balloon and of circular and square airbags (Cirak and Ortiz, 2001) and in fracture cases i.e., simulating the perforation of a circular plate impacted by a bullet (Cirak et al., 2005).

3.1.2 Extension of the subdivision surface shell element to sandwich shells

The shell finite element presented in Section (3.1.1) was originally derived assuming a uniform material across the shell thickness. However a simple modification allows it to approximate sandwich shells as well.

Equations (3.14) and (3.18) are numerically integrated across the shell thickness using, for instance, Simpson's integration rule. In the original formulation, all the integration points correspond to the same physical material. On the other hand, if the shell cross section is made of layers of different materials, different constitutive laws and material properties may be assigned accordingly at each thickness integration point. In this sense,

each integration point across the thickness represents a different material point. Figure (3.2) shows an example in which a sandwich shell with foam core and fiber reinforced external layers is modeled using the approach just described. Due to this approxima-

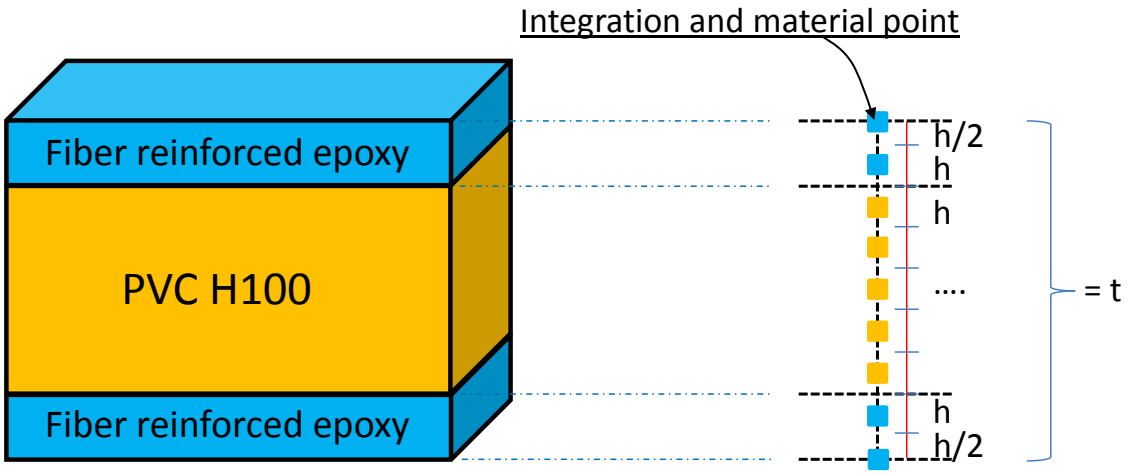

Figure 3.2: Typical sandwich shell cross section and corresponding layout of the integration/material points in the shell thickness. Integration/material points are placed at the center of each interval of length h in which the thickness t is subdivided.

tion through the thickness, the response of the sandwich shell depends on the averaged properties of the materials forming the cross section and no interfaces between layers of different materials are modeled. Thus delamination and interlayer cracking may not be considered employing the extension presented here. Despite this drawback, the proposed method possesses great flexibility since different material layouts may be tested by simply changing the material models and properties associated with the integration points across the thickness. At the same time the efficiency of the shell finite element method is preserved since no new displacement degrees of freedom are introduced. Indeed, to introduce an additional material layer there is no need to insert a new layer of elements in the shell thickness with the consequent increase in the number of nodes and corresponding nodal displacements.

3.1.3 Cohesive elements

In order to capture the possible fracture of sandwich shell structures subjected to underwater explosion, the cohesive element developed by Ortiz and Pandolfi (1999) is coupled

with the subdivision surface element as proposed by Cirak et al. (2005). The following section focuses on the application of the cohesive elements in analyses involving shell elements and the use of cohesive elements with fully 3D finite elements is not described, although the two approaches are very similar.

A cohesive element is a surface-like element that directly embeds the cohesive law presented in Section (2.3). Each cohesive element consists of two surface elements called by convention S^+ and S^-. S^+ and S^- coincide in the shell reference configuration but may separate during the deformation process forming a surface of discontinuity or fracture (Figure 3.3).

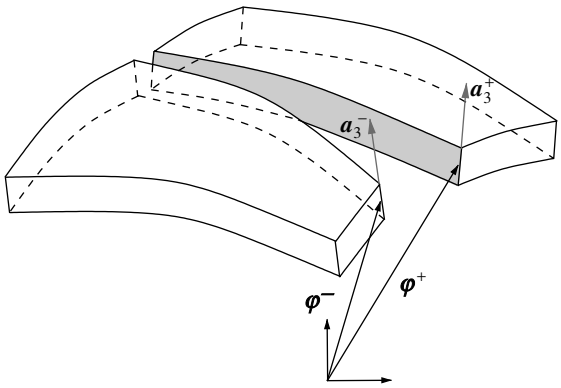

Figure 3.3: Fracture propagating in a shell: opposite crack flanks and jump in deformation mapping (figure taken from Cirak et al. (2005)).

Considering a shell of thickness h the crack flanks $S^{\pm}$ are equal to $\Gamma_C^{\pm} \times [-h/2, h/2]$, where $\Gamma_C^{\pm}$ are the curves on the cracked shell middle surface. In the parameter space (θ^1, θ^2) defined on the shell middle surface, the curves $\Gamma_C^{\pm}$ have the same parametric representation $\theta^1 = \theta^1(\xi)$, $\theta^2 = \theta^2(\xi)$ with $\xi \in \mathbb{R}$.

Across a crack surface the deformation mapping is discontinuous: $[|\boldsymbol{\varphi}|] = \boldsymbol{\varphi}^+ - \boldsymbol{\varphi}^- \neq \mathbf{0}$. Using the shell kinematic assumption written in Equation (3.4) the deformation jump may be written as:

$$[|\boldsymbol{\varphi}|] = [|\boldsymbol{x}|] + \theta^3 [|\lambda \boldsymbol{a}_3|] \tag{3.24}$$

The jump $[|\boldsymbol{\varphi}|]$ may be regarded as the crack opening displacement $\boldsymbol{\delta}$ on which the cohesive law presented in Section (2.3) is based. However, the crack opening displacement needs to be decomposed into its normal and tangential components so that the effective opening

displacement expressed in Equation (2.12) may be computed. In the discrete finite element setting, the normal to the crack surface is not defined unequivocally if the crack is open. Indeed the unit normal to the surface S^+ may differ from the unit normal to the surface S^-. In order to define a unique unit normal, the following average normal to the crack surface is defined:

$$\bar{\boldsymbol{n}} = \frac{\frac{1}{2}\left(\boldsymbol{n}^+ + \boldsymbol{n}^-\right)}{\| \frac{1}{2}\left(\boldsymbol{n}^+ + \boldsymbol{n}^-\right) \|} \tag{3.25}$$

$$\boldsymbol{n}^\pm = \boldsymbol{t}^\pm \times \boldsymbol{a}_3^\pm \tag{3.26}$$

where $\boldsymbol{a}_3^\pm$ is the shell director computed on the two different sides of the crack (Figure 3.3). The tangent vectors $\boldsymbol{t}^\pm$ are computed as:

$$\boldsymbol{t}^\pm = \frac{\partial \boldsymbol{\varphi}^\pm}{\partial \theta^\alpha} \frac{\partial \theta^\alpha}{\partial \xi} \tag{3.27}$$

All the components needed to apply the cohesive law described in Section (2.3) have now been derived. The final step to couple the shell element with the cohesive element consists in modifying the equilibrium Equation (3.19) to include the virtual work of the cohesive forces $\boldsymbol{T}$ (Equation 2.15) in addition to the virtual work of the bulk material. The equilibrium equation which also includes cohesive forces is:

$$\delta\Pi_{int} + \delta\Pi_{ext} + \delta\Pi_{kin} + \delta\Pi_{coh} = 0 \tag{3.28}$$

where

$$\delta\Pi_{coh}\left[\boldsymbol{\varphi}\right] = \int_{\bar{\Gamma}_C} \int_{-\frac{\bar{h}}{2}}^{\frac{\bar{h}}{2}} \boldsymbol{T} \cdot \delta\boldsymbol{\delta} \mu d\theta^3 d\bar{\Gamma}_C \tag{3.29}$$

Given the very short time scale on which the explosion and the structural response occur, dissipative terms related to the heat exchange between the structure and the surrounding water and related to the heat diffusion inside the structure itself are not considered.

Since the interpolation used in the shell subdivision element is non-local, the topology of the mesh and the corresponding shape functions need to be modified to describe a fracture propagating in the shell. Indeed, once a fracture starts to propagates, the displacements on each side of the crack are still interdependent given the non-locality of the shape functions

unless they are modified together with the underlying mesh. In order to circumvent the need to modify the topology of the mesh to allow for a discontinuous displacement field across a fracture, Cirak et al. (2005) proposed to pre-fracture all the element patches[4] at the beginning as shown in Figure (3.4). Before a fracture starts to propagate the pre-fractured elements are held together through a penalty approach. Once a fracture starts to propagate, the element patches on each side of the crack are free to move independently without the need to modify either the mesh or the non-local interpolation functions. Indeed the displacement field on each element on either side of the crack depends only on the displacements of the nodes belonging to its own independent pre-fractured patch.

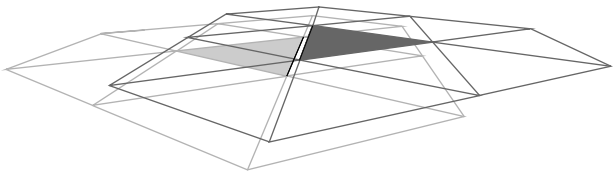

Figure 3.4: Independent element patches associated with the two dark triangular elements on each side of the crack (figure taken from Cirak et al. (2005)).

The penalty approach to enforce element compatibility consists in a slight modification of the cohesive law (Figure 3.5). For stresses less than the cohesive strength σ_c the tractions $\boldsymbol{T}$ across the element boundaries are equal to:

$$\boldsymbol{T} = k\boldsymbol{\delta} \tag{3.30}$$

where k is a penalty parameter. For $k \to \infty$ element compatibility is enforced exactly. In dynamic analyses, Cirak et al. (2005) suggest the practical choice $k = 100E/d$ where d is the element size, and similar values are used in all the analyses in the present study. Equation (3.30) is also used to enforce the non-compenetration of adjacent elements in compression. In particular, since multiple integration points are used across the shell thickness and each point may be under a different state of stress, in a bending mode-type fracture, part of the shell thickness may be in compression and thus uncracked whereas the rest of the shell cross section may be fractured. This scheme, associated with the

[4]The patch of elements associated with a chosen element el is defined by all the neighbors that share a node with el.

cohesive law described in Section (2.3), enables the modeling of shell fracture in a tearing mode, shearing mode or bending mode.

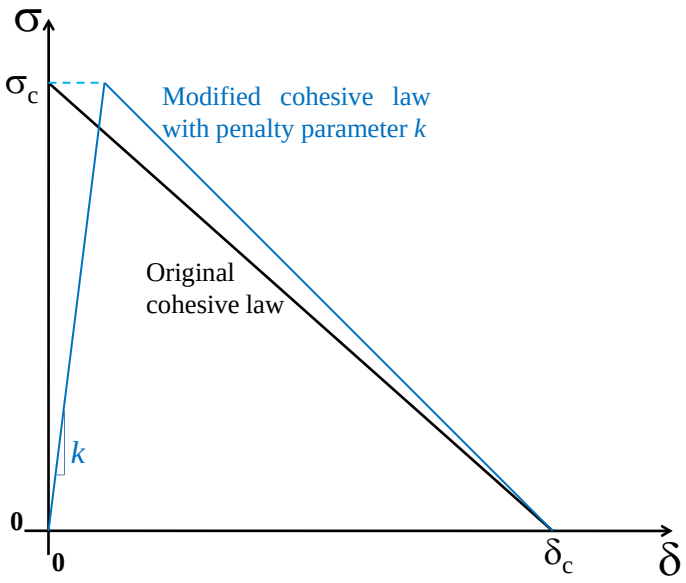

Figure 3.5: An initial branch with slope k is introduced to modify the original cohesive law when a penalty approach is chosen to enforce element compatibility before fracture propagation.

3.2 Numerical simulation of an underwater explosion

The response of sandwich structures subjected to underwater explosions is studied using two main analysis settings: in the first setup, the load due to an underwater explosion is reproduced by applying a pressure profile whereas in the second analysis setup a fully coupled fluid-solid simulation is carried out. In this latter case, the load due to the explosion is modeled by including, at time $t = 0$, a sphere of hot air at the location of the explosive charge. The air properties depend on the explosive type and characteristics.

3.2.1 Applied pressure profile

The application of a pressure profile to simulate the explosion generated pressure load has been widely used in the literature (see for instance Deshpande and Fleck (2004), Batra and Hasssan (2007), Batra and Hasssan (2008)) and has proven to be an efficient tool to determine the resistance of sandwich composite panels subjected to blast and underwater

explosions.

As proposed by Cole (1948) the peak pressure p_0 due to an explosive mass m at distance r from the explosion center is given by:

$$p_0 = K_1 \left(\frac{m^{\frac{1}{3}}}{r} \right)^{A_1} \qquad [MPa] \tag{3.31}$$

Subsequently the pressure decays in time at an exponential rate following:

$$p_t = p_0 \exp\left(\frac{-t}{\theta} \right) \qquad [MPa] \tag{3.32}$$

$$\theta = K_2 m^{\frac{1}{3}} \left(\frac{m^{\frac{1}{3}}}{r} \right)^{A_2} \qquad [ms] \tag{3.33}$$

The values of the parameters K_1, A_1, K_2 and A_2 depend on the explosive considered (See Table 3.1).

Explosive type	TNT	HBX-1	PETN
K_1	52.12 (52.4)	53.51	56.21
A_1	1.18 (1.13)	1.144	1.194
K_2	0.0895 (0.084)	0.092	0.086
A_2	-0.185 (-0.23)	-0.247	-0.257

Table 3.1: Values of the parameters K_1, A_1, K_2 and A_2 as given in Cole (1948) and reported in Batra and Hasssan (2007). The values in parentheses are taken from Swisdak (1978) and reported in Deshpande and Fleck (2004).

3.2.2 Numerical modeling of fluid-solid interaction

A fluid-solid coupled simulation is, however, more accurate, as often pointed out in the literature (see for example Xie et al. (2007), Xie et al. (2009), Tilbrook et al. (2009)). Correct modeling of the fluid-structure interaction is particularly important in the case of sandwich shells subjected to underwater explosions given the relative large flexibility of sandwich panels.

In the present research, the fluid structure interaction is modeled numerically by coupling an Eulerian fluid solver with a Lagrangian shell solver. The shell solver is based on the shell finite element described in Section (3.1.1) whereas the fluid governing equations and

the fluid-solid coupling are briefly described in the present section following Deiterding et al. (2008).

The shell and the fluid solvers are combined inside the code VTF (Virtual Test Facility) developed at the California Institute of Technology under the ASC program (Deiterding et al., 2006).

The simulation of the response of sandwich structures subjected to underwater explosions requires accounting for the fluid compressibility whereas the fluid viscosity may be safely neglected. The governing equations for the fluid solver are therefore the Euler Equations:

$$\partial_t \rho + \nabla \cdot (\rho \boldsymbol{u}) = 0 \qquad \text{Mass conservation} \tag{3.34}$$

$$\partial_t (\rho \boldsymbol{u}) + \nabla \cdot (\rho \boldsymbol{u} \otimes \boldsymbol{u}) + \nabla p = 0 \qquad \text{Momentum conservation} \tag{3.35}$$

$$\partial_t (\rho E) + \nabla \cdot ((\rho E + p)\, \boldsymbol{u}) = 0 \qquad \text{Energy conservation} \tag{3.36}$$

where ρ is the fluid density, $\boldsymbol{u}$ is the fluid velocity vector and E is the specific total energy equal to the sum of the specific internal energy e and of the specific kinetic energy $\frac{1}{2}\boldsymbol{u}\boldsymbol{u}^T$ $\left(E = e + \frac{1}{2}\boldsymbol{u}\boldsymbol{u}^T\right)$. In order to solve the fluid problem, an equation of state $p = p(\rho, e)$ needs to be added to Equations (3.34)−(3.36). The simulation of very high pressure waves, such as the ones caused by an underwater explosion, may be modeled using a stiffened gas equation of state as given in Equation (3.37);

$$p = (\gamma - 1)\, \rho e - \gamma p_\infty \tag{3.37}$$

where $\gamma = \frac{c_p}{c_v}$ is the adiabatic index and p_∞ is a constant representing the attraction between fluid molecules.

The fluid governing equations are discretized using the finite volume approach as described in Deiterding et al. (2008) and references therein.

Of primary importance in fluid structure coupled simulation is the possibility to enforce immersed moving boundary conditions in the fluid domain. In VTF, at every point in the fluid Cartesian grid a scalar function ϕ stores the distance to the immersed thin walled structure. Moreover, the normal $\boldsymbol{n}$ to the fluid domain boundaries may be computed at

any point as $\boldsymbol{n} = -\nabla\phi/\|\nabla\phi\|$. Considering only topologically open surfaces for simplicity (for topologically closed surfaces a signed distance needs to be used (Deiterding et al., 2006) to identify the inner, negative, and outer, positive, volume), a fluid cell is considered a ghost cell if ϕ evaluated at the cell center is less than $h/2$ where h is the thickness of the immersed thin structure. $\phi = h/2$ represents the immersed boundary for the fluid solver and the pressure on the immersed thin structure is computed as the differences between the pressure at $\phi = h/2$ in the positive and negative normal directions (Figure 3.6). Mesh refinement is used near the immersed thin shell to improve the staircase approximation of the fluid boundaries.

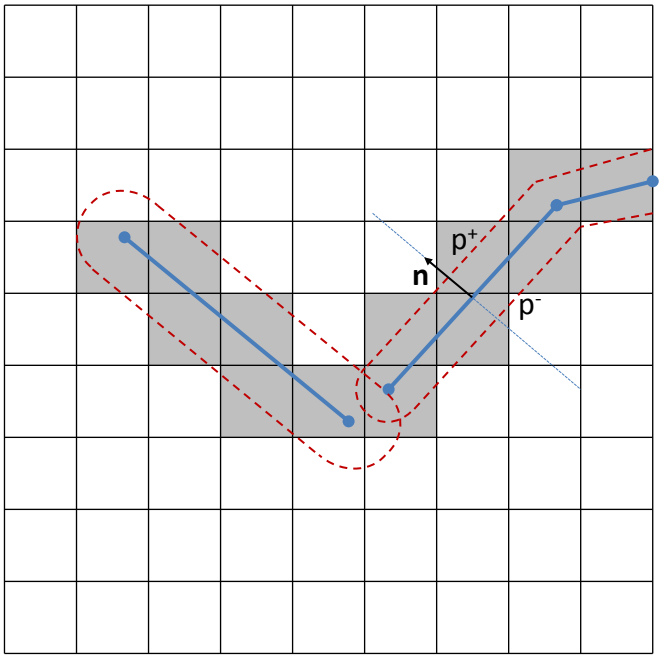

Figure 3.6: The ghost cells (shaded gray) around the immersed thin structures (blue) are represented together with the line (red) corresponding to the level set $\phi = h/2$ (figure reproduced from Deiterding et al. (2008)).

The variables inside each ghost fluid cell are set equal to the values of the nearest real cell in the fluid interior. Following this approach, if a ghost cell becomes active due to the movement of the immersed boundary, its variables are set to the correct state.
In order to couple the fluid and the shell solvers the compatibility conditions between these two systems need to be considered. In the case of an inviscid fluid, as the one considered to model shocks due to underwater explosion, there are two compatibility conditions:

- continuity of the velocity component normal to the immersed boundary;
- continuity between the fluid pressure and the normal component of the traction at the immersed boundary.

Using these compatibility conditions, the fluid and shell solvers are coupled through the following algorithm:

- update the immersed boundary by updating the level set function $\phi(t)$.
- Impose velocity compatibility by setting $u_n^{fluid} = u_n^{solid}$.
- Update fluid solver.
- Impose $(\boldsymbol{\sigma n}) \cdot \boldsymbol{n} = p^{fluid}$.
- Update shell solver.
- Advance in time: $t = t + \Delta t$.

3.3 Characteristics of the code and computational resources

The assembled computational capability is composed of mainly two parts: the shell finite element solver `sfc` originally developed by Fehmi Cirak and the fluid solver `AMROC` developed by Ralf Deiterding. These two modules are mainly written in `C` and `C++` language and are combined together with the `STLIB` modulo (auxiliary algorithms) in the Virtual Test Facility code (`VTF`) developed at the California Institute of Technology under the ASC program.
As part of the present research the sfc code has been further developed to:

- model fiber composite materials (material model, shell and cohesive elements with different fiber orientations);
- adapt its already present parallel and restart capabilities to work in analyses with sandwich material configurations and fiber composite materials;

- compute and collect the internal and external energies used both to verify the code convergence and to characterize the analyses' results as shown in Section (5).

The parallel implementation of the code is based on the open source message passing library `Open MPI` (`http://www.open-mpi.org/`) and the open source parallel partitioning library `Zoltan` (`http://www.cs.sandia.gov/Zoltan/`). Both the `sfc` code and the `VTF` code are compiled and run on the `shc` cluster, part of the Caltech Center for Advanced Computing Research (CACR). The `shc` cluster is composed of 229 8-core and 4-core nodes with 2.2 GHz processors.

Chapter 4

Verification and validation of the proposed computational scheme

Individual parts of the presented computational scheme have been verified separately by different authors: i.e Cirak and Ortiz (2001) verified the subdivision shell finite element in linearized and finite kinematics and Deiterding et al. (2008) verified the fluid solver. Here the verification of the computational scheme regards two aspects important to modeling the failure of sandwich fiber composite panels subjected to underwater explosions:

- the capability to capture fracture propagation in fiber reinforced material;
- the energy balance during simulations to assess the good functioning of the complex computational scheme, which includes fracture, fluid structure interaction, the presence of different material models across the shell thickness, etc.

Subsequently the developed computational scheme is used to simulate the experiments conducted by Inaba and Shepherd (2009a) in order to validate its capability to model the fluid-structure interaction and the structural response of fiber composites subjected to underwater shock conditions.

4.1 Fracture propagation in fiber composite sandwich structures

As discussed in Section (2.3), if fibers are oriented only in one direction, this direction constitutes a preferential path for fracture propagation since fibers cannot increase the cohesive strength of the material along their direction. On the other hand if two orthogonal

families of fibers are present no preferential direction for fracture propagation is present and the fragmentation is expected to be isotropic.

In order to test the capability of the proposed scheme in capturing fracture propagation, two plates and a cylindrical shell with different fiber orientations are considered. Fibers are aligned in one direction only in the first plate, in two orthogonal directions in the second plate and at 45^o with respect to the cylinder axis in the cylindrical sandwich shell. The plates were subjected to an underwater explosion due to a TNT charge equal to 0.1 kg at a distance of 0.20 m from the plate center whereas the pressure load acting on the cylindrical shell was caused by a 0.5 kg TNT charge placed at 0.52 m from the structure outer surface. The results from three test cases are shown in Figure (4.1) and it is possible to identify the preferential direction for fracture propagation in Figures (4.1(a)) and (4.1(c)) and the absence of such direction in Figure (4.1(b)).

4.2 Energy balance

The balance between the total internal energy and the work done by the applied external load is a requirement for the global convergence of a computational scheme. The present computational scheme is particularly complex since the total internal energy is the sum of the deformation energy, the kinetic energy and the dissipated cohesive energy. The balance between the work done by the applied external load and the sum of the accumulated or dissipated energies guarantees convergence and equilibrium at every time step. Moreover, the energy convergence assures that each energy term is computed correctly and may be used as an indicative factor of the total deformation or damage (and therefore performance) of the analyzed structure. The magnitudes of the different energy contributions may also be used to understand how the energy due to an underwater explosion is redistributed once the generated pressure wave hits the target structure. For instance, the comparison between the dissipated cohesive energy and the stored elastic energy indicates the amount of deformation accomodated in fracture and in the bending/stretching mode during the explosion.

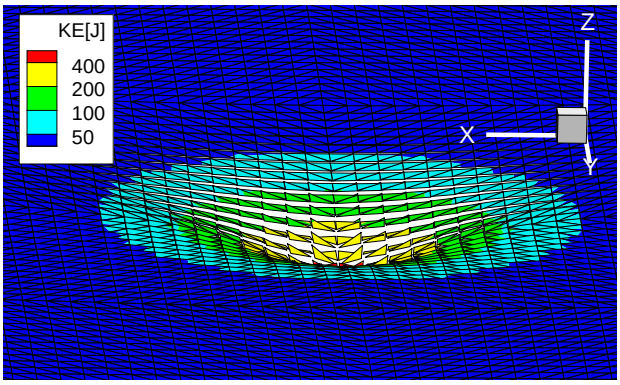

(a) Sandwich plate with fibers in the external layers oriented along the X axis.

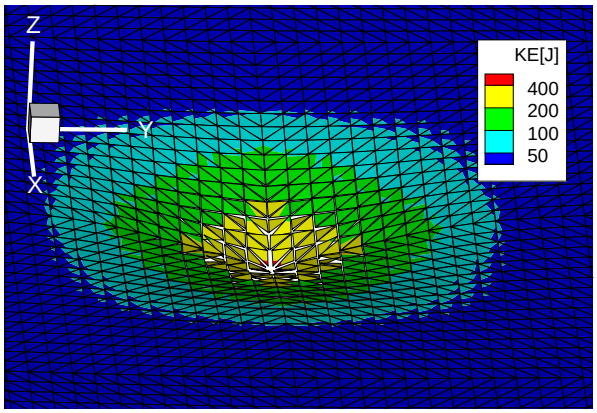

(b) Sandwich plate with fibers in the external layers oriented along the X and Y axes.

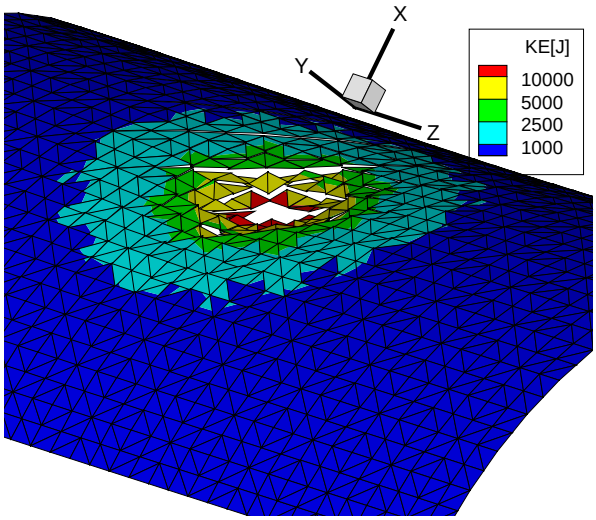

(c) Sandwich cylindrical shell with fibers in the external layers oriented at 45^o with respect to the cylinder axis.

Figure 4.1: Onset of fracture propagation in shell sandwich structures subjected to a pressure load due to an underwater explosion. The kinetic energy contour plots are also shown.

As an example, the energy balances for two plate analyses similar to the ones shown in Figure (4.1) are reported in Figure (4.2). In both analyses the equilibrium between the applied external work and the internal energy is verified with a maximum error of 1.7%. This error is due to the complexity of the dynamic simulations that are carried out using a Newmark explicit time integration scheme and include fracture and fragmentation.

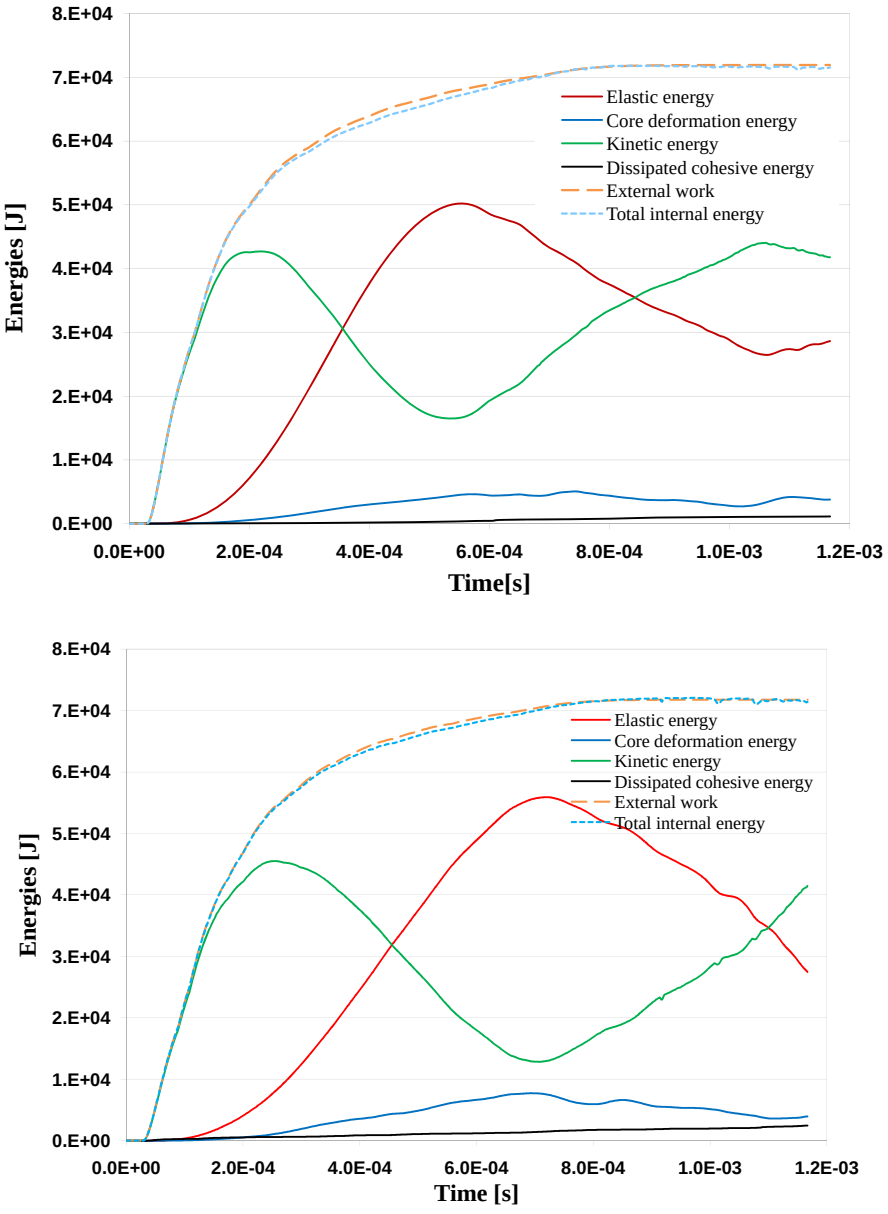

Figure 4.2: Energy convergence plots for two sandwich square plates with fibers in the external layers oriented along one (upper) and two (bottom) directions.

4.3 Elastic response of water filled composite tubes under impulsive loading

Inaba and Shepherd (2009a) subjected several resin-fiber composite tubes filled with water to a water hammer load. Figure (4.3) shows the experimental setup. The water hammer is induced by a 1.5 kg steel projectile that impacts a plastic buffer on the top of the vertical fiber reinforced tube. The steel projectile falls from a constant height and this guarantees that the speed at the time of impact on the plastic buffer is constant in subsequent experiments [1] (the speed of the steel projectile at the time of impact is equal to 5.3 m/s). A gland seal is placed between the plastic buffer and the tube so that no water may exit the tube and the buffer only impacts the water surfaces and not the tube upper edge. This experimental setup guarantees that at the time of impact stress waves are generated only in the water and not in the tube. Therefore the measured stress waves in the tube will be only due to the water-tube interaction. The bottom of the tube is fastened to a fixed aluminum bar. The tube is instrumented with axial and hoop strain gages 100 mm apart and with a pressure gage placed at the bottom. The tube specimens are 0.9 m long, 1.66 mm thick and have an inner diameter equal to 38.3 mm.

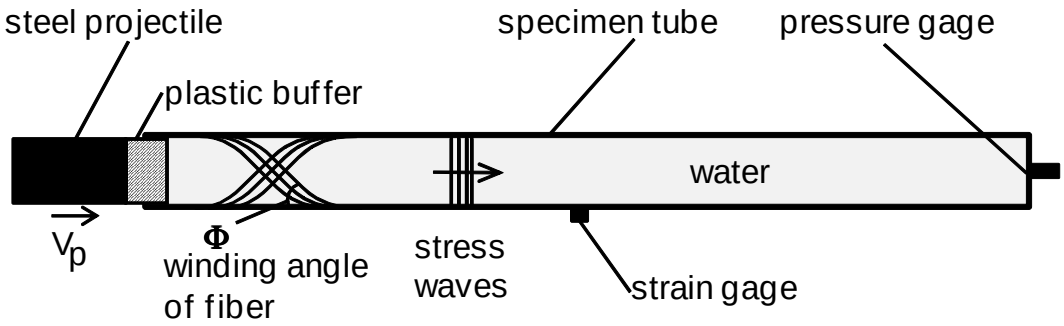

Figure 4.3: Experiments' setup used in the validation analyses: specimen geometry, loading conditions and instrumentation. Figure taken from Inaba and Shepherd (2009a).

During subsequent experiments, tubes with different fiber winding angles were tested in order to study the effect of this design parameter on the tube response to the generated water hammer. During the following validation, two fiber winding angles equal to 45^o and

[1] The piston movement is directly incorporated in the simulations by using a signed distance level set function and by integrating the piston equation of motion as explained in Deiterding et al. (2008).

60^o are considered (Figure 4.4).

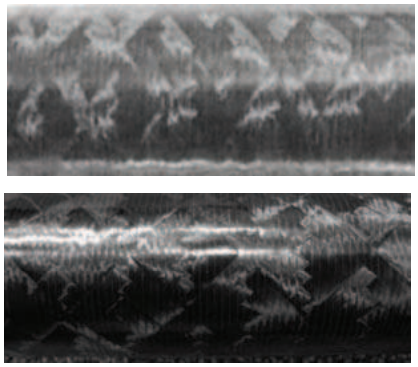

Figure 4.4: Sections of the carbon fiber reinforced tubes used in the experiments with winding angle equal to 60^o (upper image) and 45^o (bottom image). Figure taken from Inaba and Shepherd (2009a).

The material properties of the tubes' carbon fibers and epoxy resin are given in Table (4.1).

Fiber	
Young's modulus	238 GPa
Density	1770 kg/m^3
Matrix	
Young's modulus	2.83 GPa
Density	1208 kg/m^3
Poisson's ratio	0.28
Composite	
Fiber volume fraction	0.7

Table 4.1: Material properties for the fiber composite tubes used in the experimental campaign.

Inaba and Shepherd (2009a) extract five quantities as representative of the experimental results during the tests of fiber composite tubes with different winding angles: precursor wave speed, primary wave speed, average of hoop and longitudinal strain peaks at the primary wave front, and pressure recorded at the bottom of the tube. These quantities are used to compare the simulation results with the experimental ones.

As discussed by Inaba and Shepherd (2009a), fluid-structure interaction plays a major role in determining the tube structural response in these experiments; therefore the experiments are optimal for validation of the coupled fluid-solid code's capabilities. The used numerical model contains 33280 shell finite elements, corresponding to 50076 degrees of freedom, and the fluid domain is discretized using a 16 x 16 x 264 grid for a total of 67584 cells. A section of the finite element mesh together with the locations of the experimental strain gages are reported in Figure (4.5).

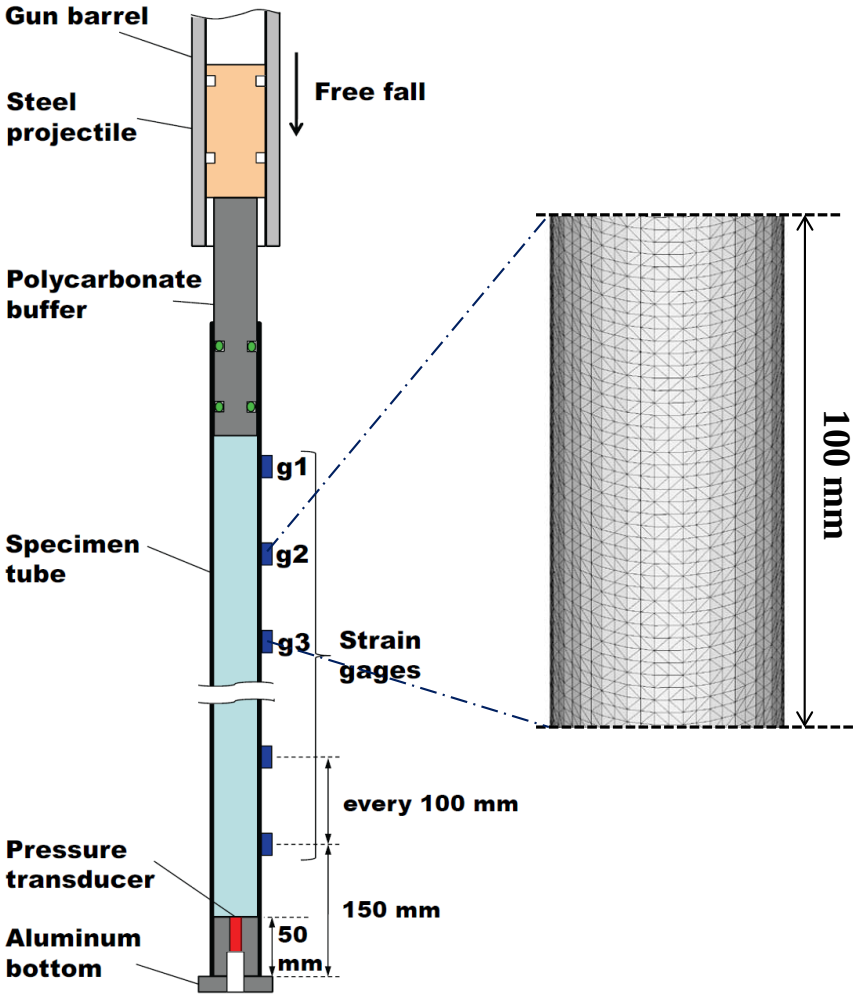

Figure 4.5: Strain gage locations (figure taken from Inaba and Shepherd (2009a)) and section of the mesh used in the simulations.

Once the steel projectile impacts the buffer at the top of the tube, the buffer transmits the impulse to the water inside the tube. After this point in time the load is transmitted from the water to the tube and back from the tube to the water due to the elastic expan-

sion and contraction of the tube itself. A first wave starts traveling inside the tube due to the first deformation imparted from the water onto the tube but it does not cause the main deformation in the tube; this wave is called the precursor wave and mainly travels along the fibers that possess the highest Young's modulus to density ratio with respect to the epoxy matrix. In order to compute the precursor wave speed during the simulations, the displacement histories in the direction of the tube axis at seven strain gages' locations were measured.

The precursor wave passes from a given location when a displacement different than zero is first registered. The longitudinal displacement versus time plots are reported in Figure (4.6). The displacement profiles in Figure (4.6) are offset based on the strain gage location so that it is possible to interpret the signal to capture the precursor wave moving along the tube.

The precursor wave speeds computed in the numerical simulations with fiber winding angle equal to 45^o and 60^o are, respectively, 4754 m/s and 3186 m/s. The experimental values are 3686 m/s and 2777 m/s, which correspond to errors of 29.0% and 14.7%, respectively. The errors computed between the experimental and numerical precursor wave speeds are higher than those relative to all the other parameters compared between simulations and experiments. The material properties are considered to be the main cause of this discrepancy since the ones given for the composite tube correspond to the mean values reported in the literature and from the tube manufacturer. No tests on the real tube specimens have been performed to determine the real specimen material properties. The precursor wave speed is highly influenced by the fiber material properties since it mostly travels along them. A calibration process could be undertaken to calibrate the fiber and matrix material properties and obtain a better agreement between simulations and experiments. However, the scope of the present validation was not to fine-tune the model to these specific examples, which are anyway relative to only two single experiments.

The precursor wave speed is greater in the tube with winding angle equal to 45^o because it travels principally along the fibers; a smaller winding angle corresponds to a shorter distance to travel along the tube.

The primary wave speed (Korteweg wave, Lighthill (1978)) is defined as the speed at which

the main deformation wave travels. With respect to the precursor wave speed, a different time and displacement scale are needed to capture the primary wave speed. Indeed the primary wave speed is slower and involves larger displacements than the precursor wave speed. For this reason, two displacement versus time plots are used, which are different from the ones presented in Figure (4.6). The displacements in the radial direction versus time are plotted in Figure (4.7) at the gage locations along the tube. As in the case of the precursor wave speed, the displacement traces are offset based on the gage location in order to highlight the motion of the primary wave front along the tube. The primary wave passes at a given location when the radial displacement increases significantly (the first sharp increase in radial displacement corresponds to the peak of hoop strain at the primary wave front). The primary wave speeds computed in the simulations with fiber winding angle equal to 45^o and 60^o were, respectively, 709 m/s and 1015 m/s. The respective experimental values are 675 m/s and 1062 m/s. These correspond to errors equal to 5.0% and -4.4% for the 45^o and 60^o winding angle tubes.

Figure (4.8) shows the longitudinal strain histories at the strain gage locations during the beginning of the simulations. The first peaks of longitudinal strain at different strain gage locations correspond to the passage of the primary wave front. The averages of the first peaks of longitudinal strain computed in the simulations are equal to -2.86×10^{-3} and -2.41×10^{-3} for fiber angles equal to 45^o and 60^o, respectively. The corresponding experimental value for both fiber angles is -2.7×10^{-3} and the relative error is 5.9% and -10.7% in the case with fiber angle equal to 45^o and 60^o, respectively. Another aspect observed in the experiments is the presence of a longitudinal strain precursor, which is initially in tension: Figure (4.8) shows that the same tension precursor is computed in the numerical simulations. The greater amplitude of the tension precursor in the 60^o case is due to a stronger coupling between hoop and longitudinal strains with respect to the 45^o winding angle case.

Figure (4.9) shows the hoop strain histories at the strain gage locations during the beginning of the simulations. The averages of the first peaks of hoop strain computed in the simulations are 3.51×10^{-3} and 1.67×10^{-3} corresponding to the fiber winding angle equal to 45^o and 60^o, respectively. The corresponding experimental values are 3.3×10^{-3} and 1.9×10^{-3}, which lead to errors of 6.4% and -12.1%, respectively.

Figure (4.10) shows the pressure histories at the top, middle and bottom of the fiber composite tube. In the case with fiber angle equal to 45^o, the pressure wave traveling down the tube and being reflected back from the bottom of the tube is clearly visible. The 60^o angle case simulation was too short to capture the reflection. The maximum pressure at the bottom of the tube computed in the simulations is 8.74 MPa and 13.07 MPa, respectively, for fiber winding angle equal to 45^o and 60^o. The experimental pressure values at the bottom of the tube are 8.04 MPa and 13.25 MPa, respectively, and the corresponding errors between experiment and simulations are equal to 8.8% and -1.3% .

The energy balance during the simulations is reported in Figure (4.11) and the convergence of the code is once more verified even during complex fluid-solid coupled simulations.

Finally a summary of the comparison between experimental and simulation results is presented in Tables (4.2) and (4.3).

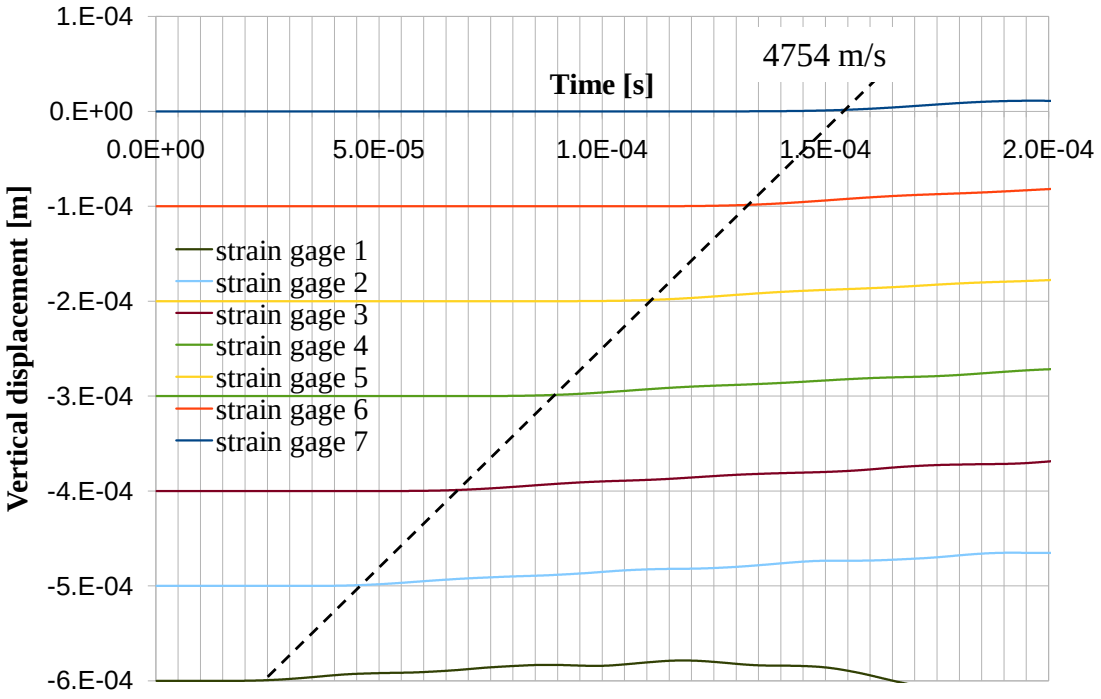

(a) Numerical simulation with fiber angle equal to 45^o.

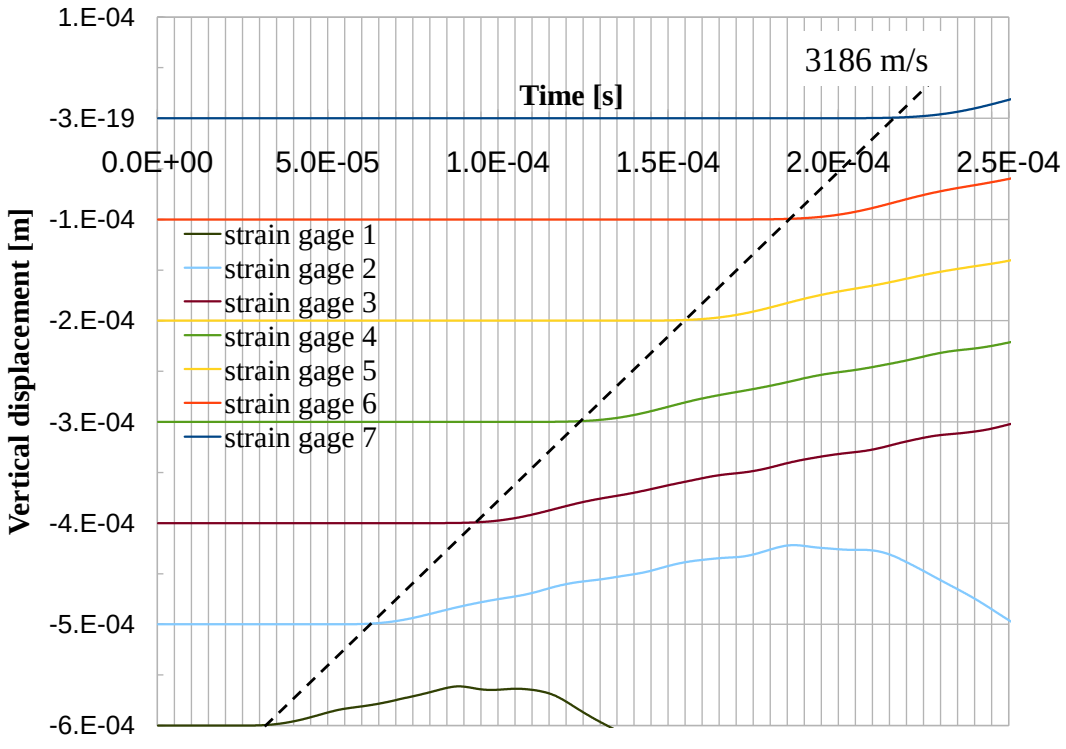

(b) Numerical simulation with fiber angle equal to 60^o.

Figure 4.6: Onset of vertical displacements at subsequent strain gage locations used to determine the precursor wave speed. Each measurement is offset based on the strain gage location.

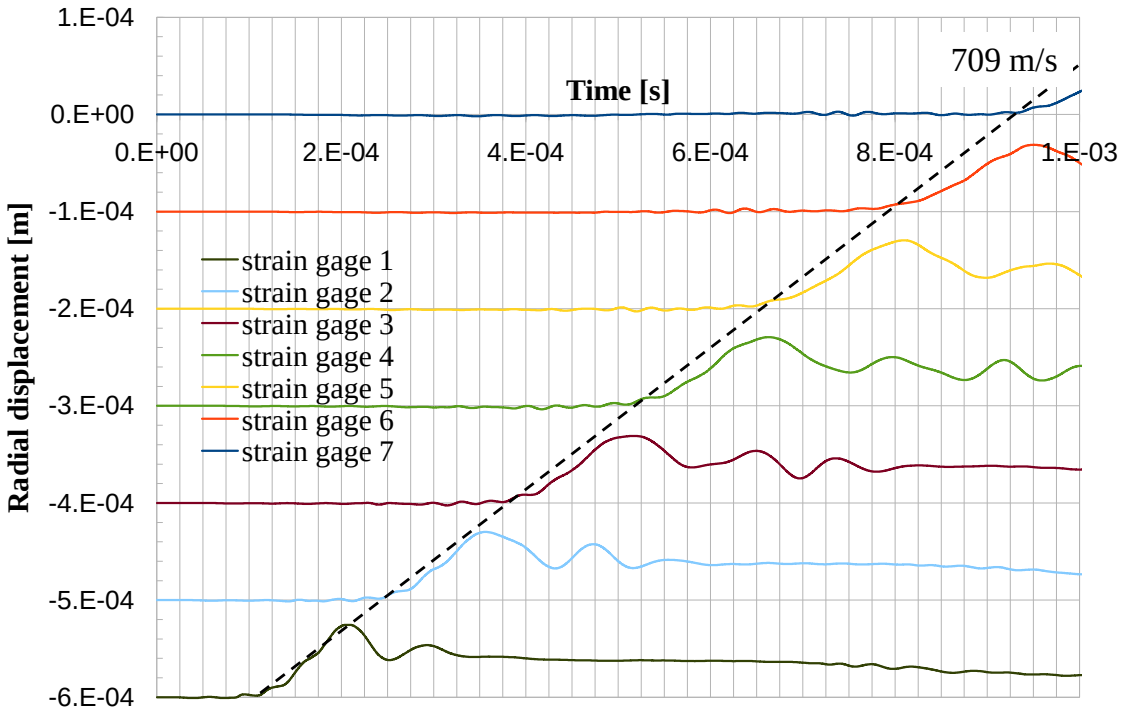

(a) Numerical simulation with fiber angle equal to 45^o.

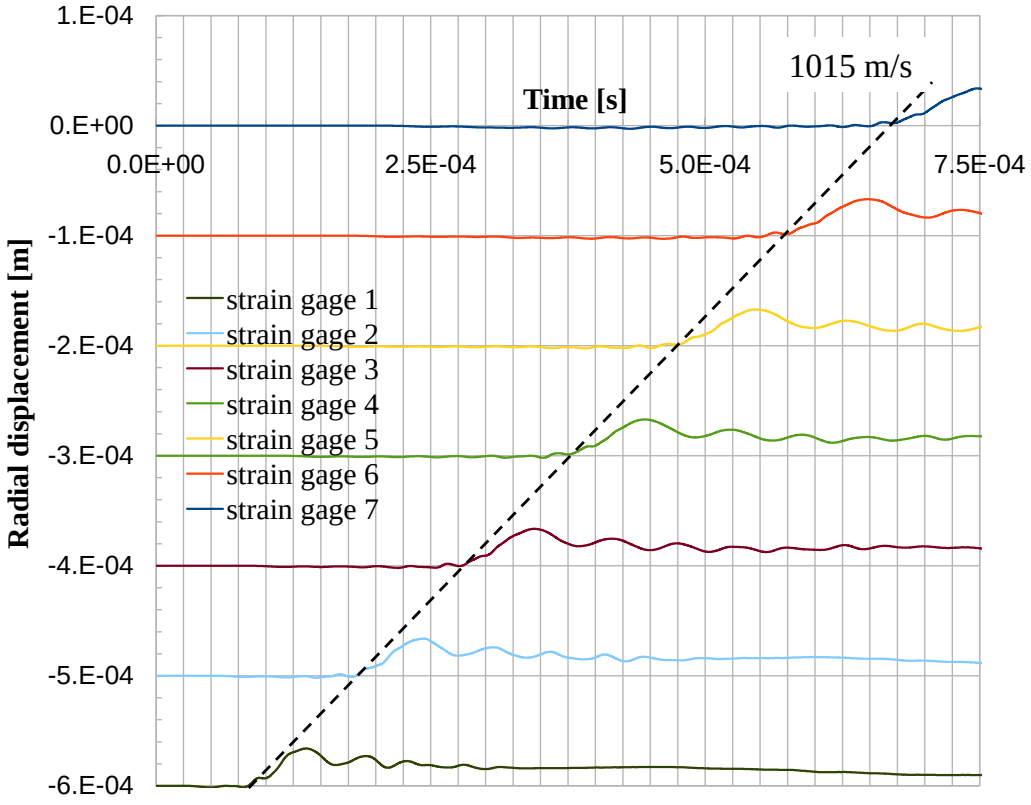

(b) Numerical simulation with fiber angle equal to 60^o.

Figure 4.7: Onset of radial displacements at subsequent strain gage locations used to determine the primary wave speed. Each measurement offset is based on the strain gage location.

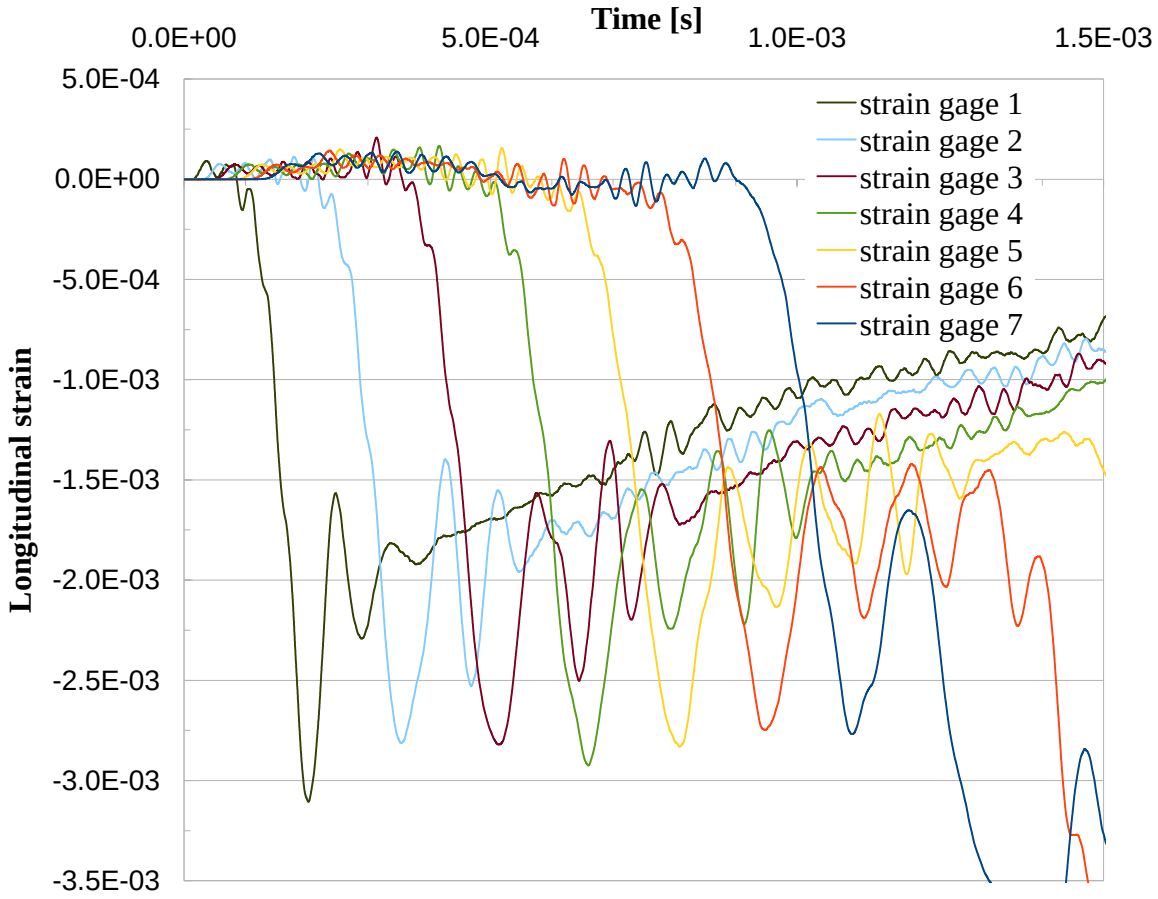

(a) Numerical simulation with fiber angle equal to 45^o.

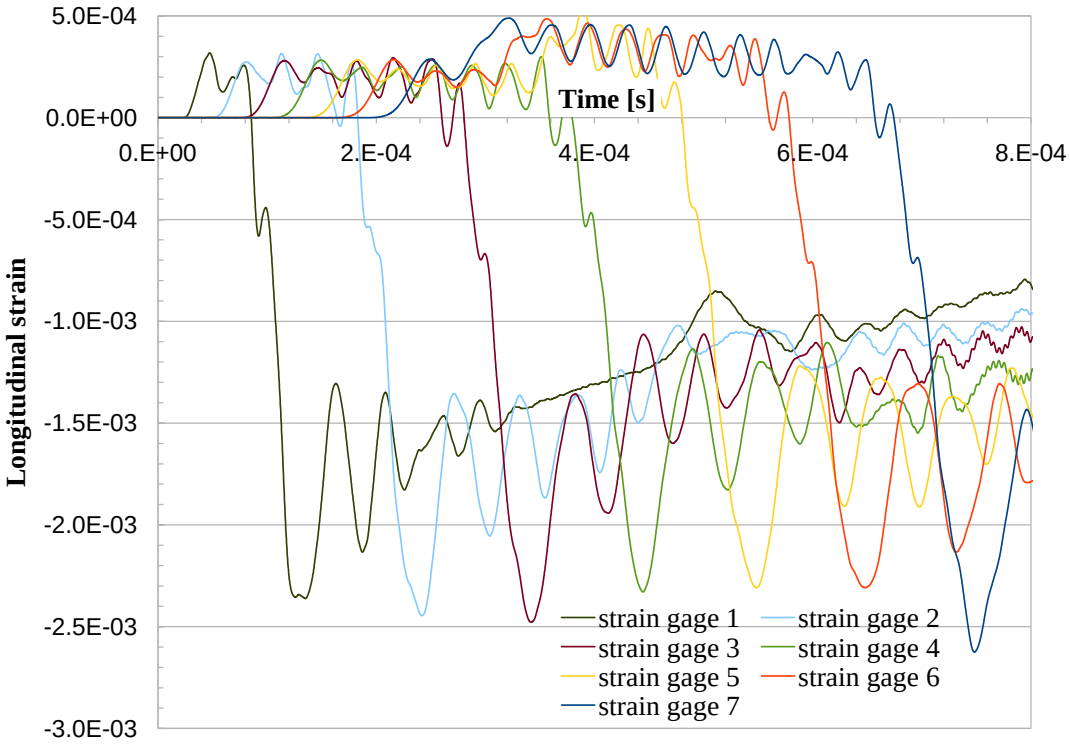

(b) Numerical simulation with fiber angle equal to 60^o.

Figure 4.8: First peaks of longitudinal strain at subsequent strain gage locations.

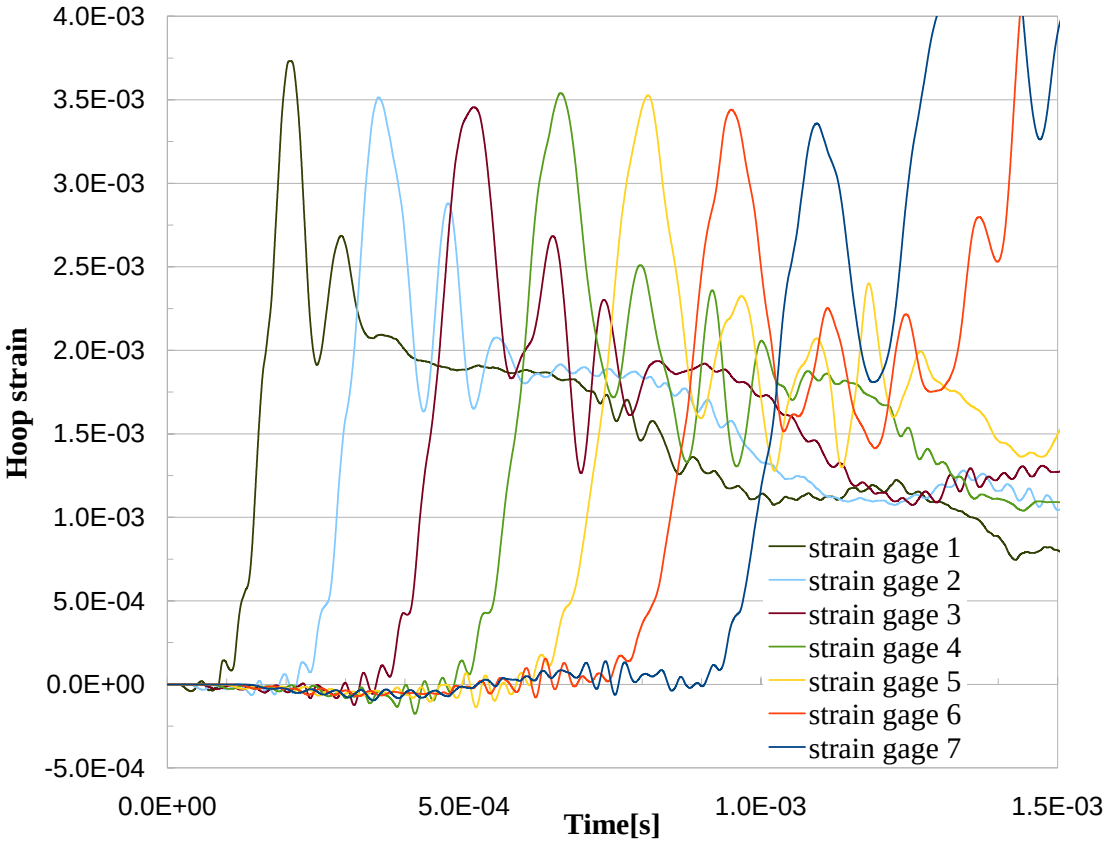

(a) Numerical simulation with fiber angle equal to 45^o.

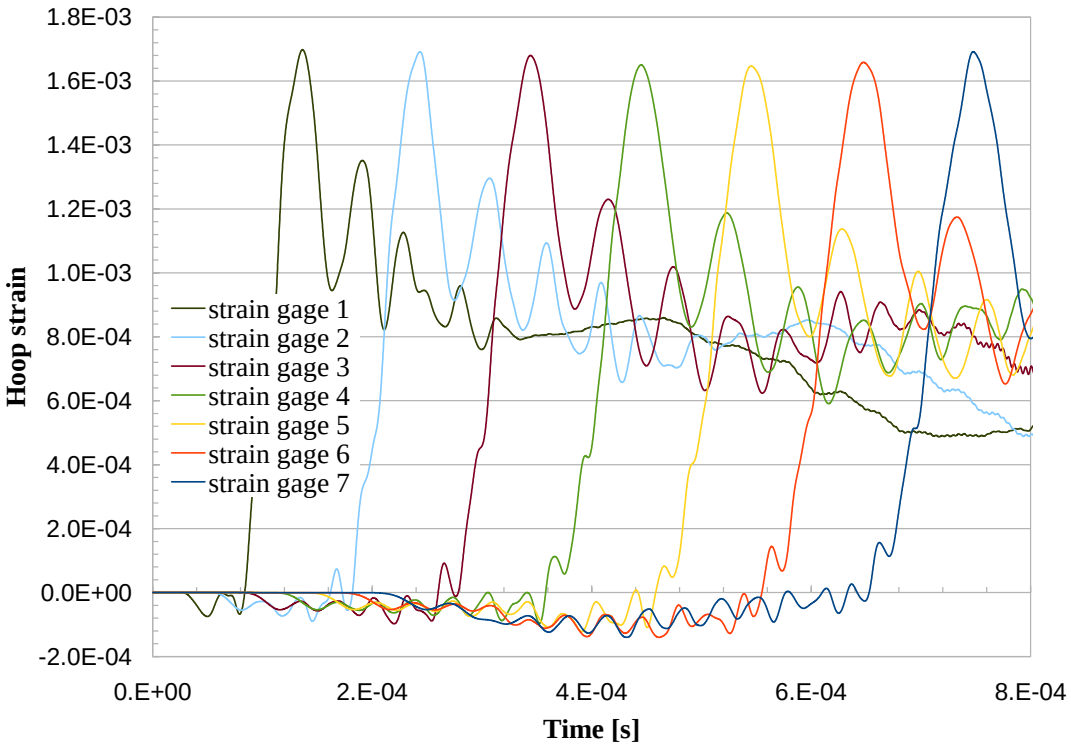

(b) Numerical simulation with fiber angle equal to 60^o.

Figure 4.9: First peaks of hoop strain at subsequent strain gage locations.

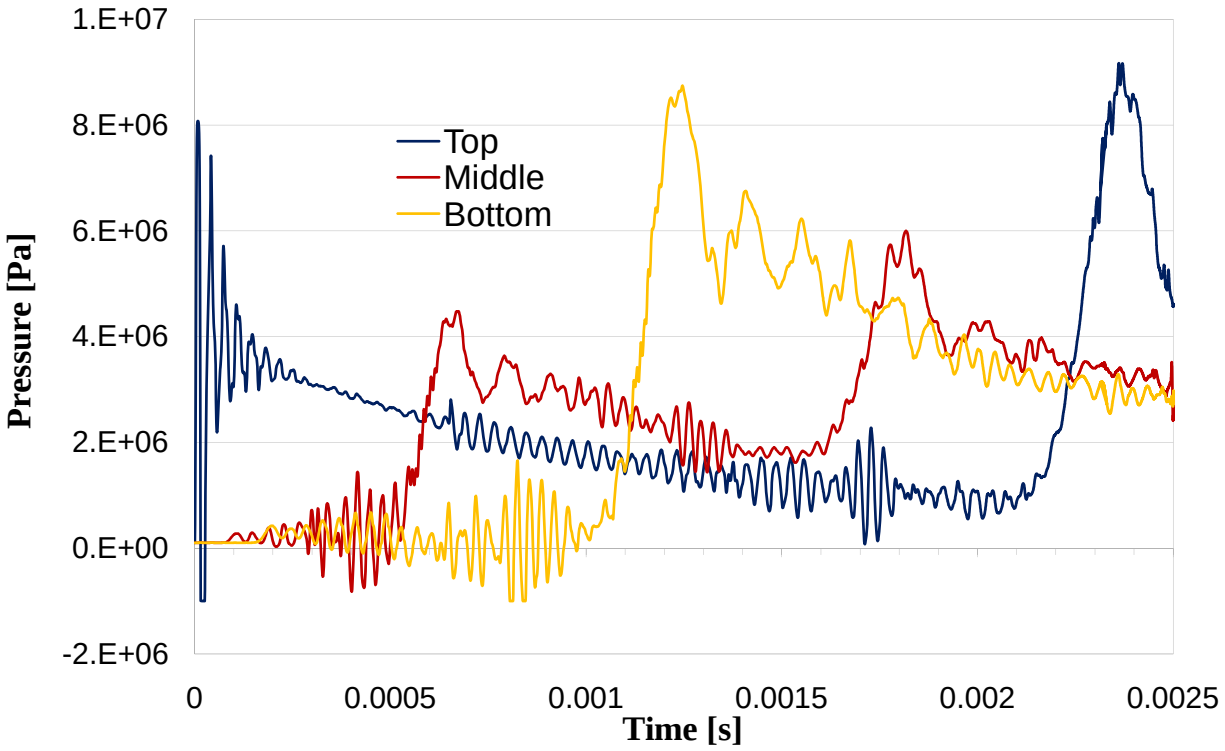

(a) Numerical simulation with fiber angle equal to 45^o.

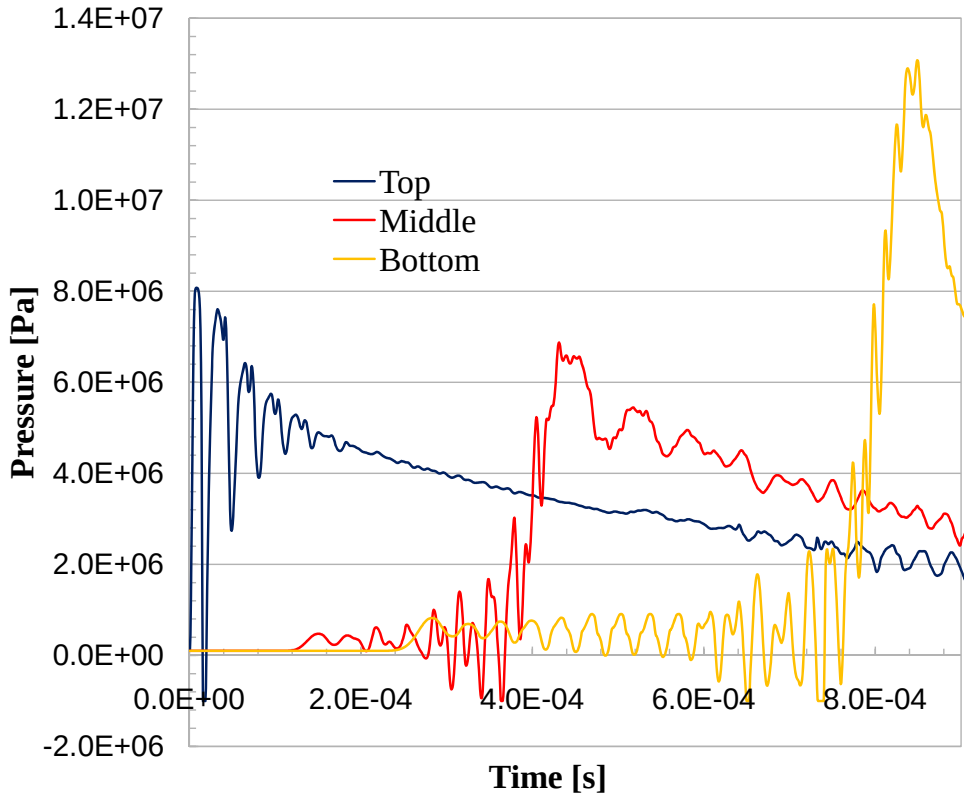

(b) Numerical simulation with fiber angle equal to 60^o.

Figure 4.10: Pressure history at three different locations along the tube axis.

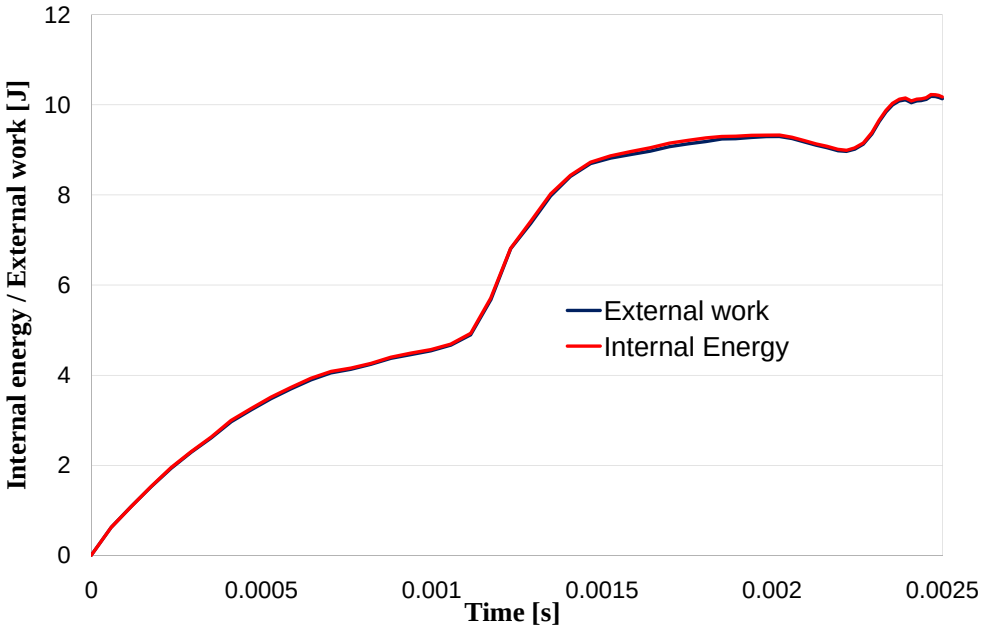

(a) Numerical simulation with fiber angle equal to 45^o.

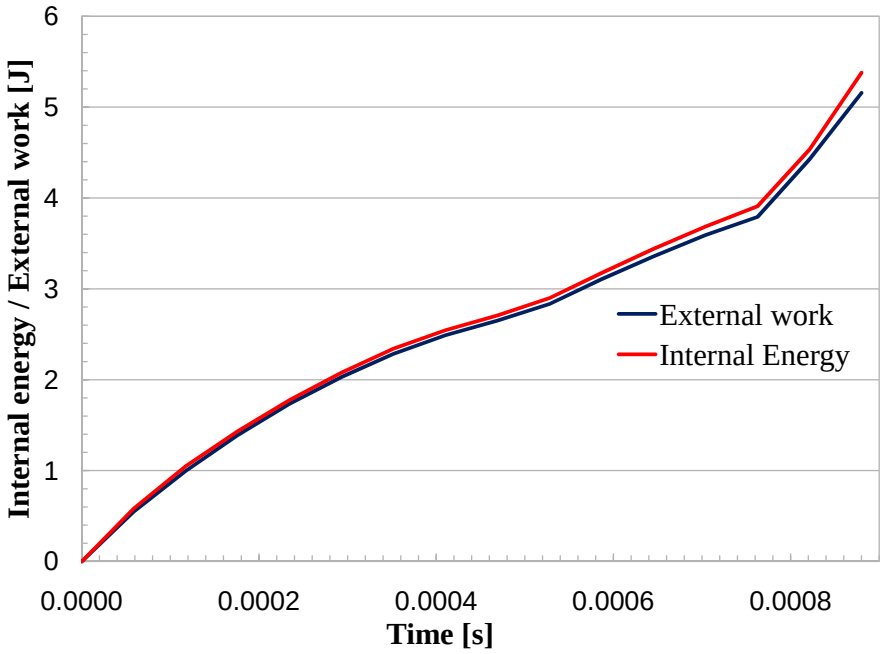

(b) Numerical simulation with fiber angle equal to 60^o.

Figure 4.11: Balance between external work and internal energy during the validation analyses.

	Experimental	**Computed**	**Error %**
Precursor wave speed [m/s]	3686	4754	29.0
Primary wave speed [m/s]	675	709	5.0
Averaged first peak hoop strain	3.3×10^{-3}	3.51×10^{-3}	6.4
Averaged first peak longitudinal strain	-2.7×10^{-3}	-2.86×10^{-3}	5.9
Ratio between axial and hoop strain	-0.82	-0.81	-0.5
Pressure at tube bottom [MPa]	8.0	8.7	8.8

Table 4.2: Comparison among experimental and computed results (fiber angle equal to 45^o).

	Experimental	**Computed**	**Error %**
Precursor wave speed [m/s]	2777	3186	14.7
Primary wave speed [m/s]	1062	1015	-4.4
Averaged first peak hoop strain	1.9×10^{-3}	1.67×10^{-3}	-12.1
Averaged first peak longitudinal strain	-2.7×10^{-3}	-2.41×10^{-3}	-10.7
Ratio between axial and hoop strain	-1.42	-1.44	1.6
Pressure at tube bottom [MPa]	13.3	13.1	-1.3

Table 4.3: Comparison among experimental and computed results (fiber angle equal to 60^o).

As Inaba and Shepherd (2009a) found in the experiments, the anisotropy of fiber composite tubes leads to a significantly different relation between axial and hoop strains with respect to metal tubes. Since the fiber winding angle is less than 90^o, the stress in the hoop direction is transmitted in the longitudinal direction. Therefore a longitudinal contraction is caused by the radial expansion due to the pressure wave induced by the water hammer. For this reason the hoop and longitudinal strains are of similar magnitude but opposite in sign. The longitudinal to hoop strain ratio ($\frac{\varepsilon_A}{\varepsilon_H}$) obtained in the experiments with fiber angle equal to 45^o and 60^o is equal to -0.82 and -1.42. The longitudinal to hoop strain ratios computed in the simulations are, respectively, equal to -0.81 and -1.44 and agree very well with the experimental ones. In the tube with winding angle equal to 60^o, a given hoop strain generates a greater axial contraction than in the tube

with winding angle equal to 45^o.

4.4 Failure of water filled composite tubes under impulsive loading

Inaba and Shepherd (2009b) repeated the experiments described in the previous section with higher initial projectile velocities. With respect to the tests described in Section (4.3), the experimental setup only differs for the presence of two circumferential clamps at the top and bottom of the tube to prevent radial expansion and fluid leakage. As before, two fiber winding angles equal to 45^o and 60^o are considered in the experimental setup and in the simulations. The tube characteristics and the buffer initial velocity in each experiment are reported in Table (4.4)

Winding angle	**Wall thickness**	**Inner diameter**	**Buffer speed**
45^o	1.59 mm	38.3 mm	40.8 m/s
60^o	1.65 mm	38.3 mm	43.9 m/s

Table 4.4: Specimens' characteristics and initial buffer velocity for the considered experiments.

Table (4.5) contains strength material properties to characterize the failure of the fiber composite material.

Fibers	
Elongation at break	1.8 %
Tensile strength	4620 MPa
Matrix	
Elongation at break	5.5 %
Tensile strength	68.95 MPa

Table 4.5: Material properties to characterize the failure threshold of the fiber composite tubes used in the experiments.

Due to the high initial buffer speed, fracture occurs in the fiber composite tubes and

therefore the numerical models used to replicate the current experiments are quite different from the ones used in the analyses of Section (4.3). In particular, the shell finite elements that discretize the tube are now allowed to separate if the maximum cohesive strength of the material is locally reached. This requires that all the shell elements need to be pre-fractured at the beginning and that a penalty formulation is used to ensure element compatibility until a crack starts to propagate as explained in Section (3.1.3). Moreover, the fluid model is composed of two parts; one represents the water inside the tube and the other the air outside it. If the tube fractures, water is allowed to spill from the tube: this aspect of the model is particularly complicated. The used computational model contains 600,912 degrees of freedom and 399,360 elements in the shell solver. The fluid domain is discretized using a 24 x 24 x 264 grid for a total of 152,064 cells.

Primary and precursor wave speeds together with the pressure at the bottom of the tube are reported in the experiments and are used to compare experimental and simulation results. Contrary to the previous set of experiments with lower buffer speed, the hoop and longitudinal strains are not reported for the present experiments and therefore cannot be used in the following comparison.

Tables (4.6) and (4.7) report the experimental and simulated results together with the respective error.

	Experimental	**Computed**	**Error [%]**
Precursor wave speed [m/s]	3586	4444	23.9
Primary wave speed [m/s]	663	710	7.1
Pressure at tube bottom [MPa]	23.0	54.8	138.3

Table 4.6: Comparison between experimental and computed results (fiber angle equal to 45^o).

	Experimental	**Computed**	**Error [%]**
Precursor wave speed [m/s]	2862	3077	7.5
Primary wave speed [m/s]	1059	1000	-5.6
Pressure at tube bottom [MPa]	83.1	83.4	0.4

Table 4.7: Comparison between experimental and computed results (fiber angle equal to 60^o).

The precursor and primary wave speeds reported in the experiments with high initial buffer speed do not differ significantly from the values reported in Tables (4.2)−(4.3), which were obtained for lower buffer initial velocity. Given the distinctly different numerical setup, it is noteworthy that the numerically predicted wave speeds still agree reasonably well with the experimental values. In the case of winding angle equal to 60^o, the pressure computed at the bottom of the tube agrees very well with the reported experimental value but a large difference is present in the case of winding angle equal to 45^o. However, just as in the experiments, the pressure value at the bottom of the tube with winding angle equal to 45^o is significantly smaller than the value reported for the tube with winding angle equal to 60^o.

The discrepancy between experimental and computed pressure value may be due to an over-idealized modeling of the experimental boundary conditions. The pressure value at the bottom of the tube has been found to be very sensitive to the boundary conditions imposed at the top and bottom of the tube. Different boundary conditions may trigger the fracture of the tube in different places and influence the pressure profile inside the tube. Moreover, a more accurate material model to describe fiber composite failure may be necessary including components such as: fiber-matrix debonding, fiber-fiber sliding, and fiber-fiber interaction. Additionally Inaba and Shepherd (2009b) report the pressure value in only one isolated experiment with fiber winding angle equal to 45^o. A consistently repeated result would be helpful to understand the full nature of the problem. A priori, a higher pressure value should be expected in the experiments with fiber winding angle equal to 45^o. In a similar experiment made using a glass fiber reinforced tube and fiber angle equal to 50^o, the bottom pressure value is equal to 79.3 MPa. Moreover, the experimental response of the tube with fiber angle equal to 45^o is more elastic than that

of the tube with winding angle equal to 60^o. Indeed, the 45^o tube bursts only when the pressure wave reflected from the bottom reaches the buffer, while the 60^o tube bursts when the pressure wave first reaches the bottom of the tube. A more elastic behavior should contribute to an increase in the pressure value registered at the bottom of the tube. A better understanding of the behavior of the tube with winding angle equal to 45^o is left for future research as at the moment more experimental results are also needed. Moreover, current work is also focused on simulating the fracture pattern observed in the experiments with fiber winding angle equal to 60^o.

Chapter 5

Results and applications

A brief comparison is first carried out to assess the use of an applied pressure profile versus a fluid-solid coupled simulation in modeling the response of shell structures to underwater explosion. Subsequently, the simpler and computationally less expensive approach which consists of applying an equivalent pressure profile is used in two sets of analyses. First, the role of fiber volume fraction and fiber orientation in the face sheets of a sandwich panel is addressed through a factorial design. Then, the resistance of sandwich panels composed of aluminum face sheets and fiber reinforced face sheets is compared. The best cross section design is finally applied to the hull of a real Argentinean navy vessel. An 8 m long section of the vessel hull is subjected to an underwater explosion and its response is studied with respect to varying charge mass and charge distance.

5.1 Applied pressure profile versus FSI simulations

As described in Section (3.2), two methods are available in the present computational scheme to simulate the load due to an underwater explosion: a pressure profile applied to the solid structure or a fluid-solid coupled simulation. A fluid-solid coupled simulation models more realistically the physics of the problem. However, a prescribed pressure profile results in a less complex numerical setup and also in a faster simulation. Before choosing which method to use in different analyses, a brief comparison is carried out to capture the main differences between these two methodologies.

The simulation of the experiment performed by Ashani and Ghamsari (2008) is chosen to compare the two approaches since:

1. The coupled fluid-shell code `VTF` has also been validated by Deiterding et al. (2008) using this experiment and the agreement with the experimental results is very satisfactory.

2. The experiment focuses on the response of a small aluminum plate subjected to an underwater explosion. Therefore the comparison may be restricted to the methodology for applying the explosive pressure load and does not involve other new variables such as the response of a sandwich material configuration.

3. The comparison between the loading methods may be carried out with respect to a real experiment and not only between two numerical simulations.

During the experiment, a 0.02 kg charge of C4 (1.34 x TNT) explosive is detonated inside a water filled pool at distance of 0.25 m from the air-backed aluminum plate. The aluminum plate of radius 150 mm is fixed to the top of an immersed air filled cylinder and the exposed radius is equal to 85 mm. The plate thickness is equal to 3 mm (Figure 5.1). The plate finite element model contains 8,148 triangles, which are constrained for $r \geq 85mm$.

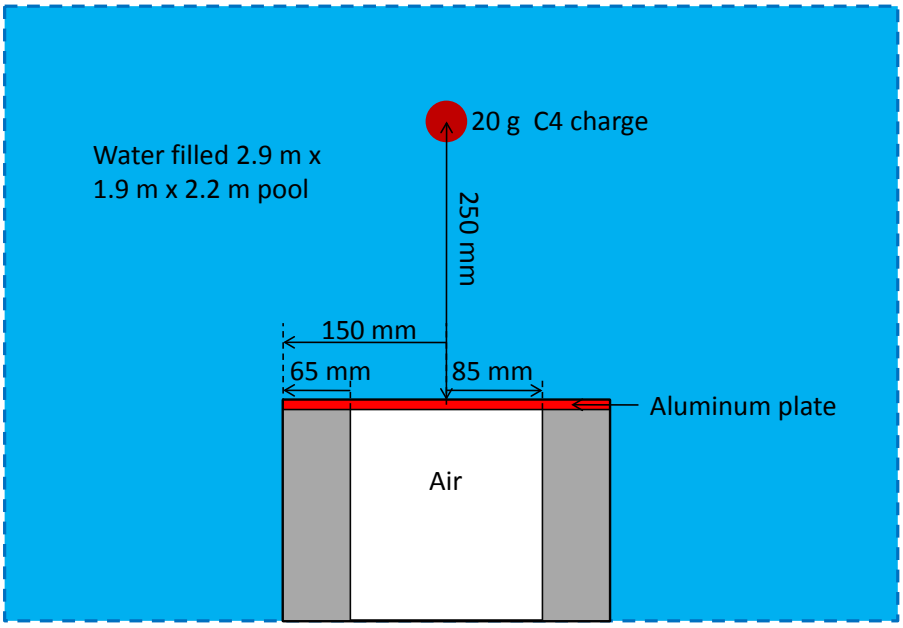

Figure 5.1: Schematic experimental setup.

The aluminum material behavior is described using a J_2 plasticity model (Lubliner, 2008) with power law hardening and rate dependency and the material properties employed in the simulations are listed in Table (5.1).

Mass density	2719 kg
Young's modulus	69000 Mpa
Yield stress	275 MPa
Poisson ratio	0.33
Reference plastic strain	0.001
Hardening exponent (1/n)	0.07
Reference plastic strain rate	0.6
Rate sensitivity exponent (1/m)	0.01

Table 5.1: Aluminum material properties used in both simulations.

The first analysis performed reproduces the validation made by Deiterding et al. (2008); in this analysis the C4 charge is modeled as an energy deposition uniformly distributed over an initial 5 mm radius sphere of air at a temperature equal to $1,500^o$ C. In the second analysis performed, the effect of the C4 charge is modeled using an applied pressure profile, which is described by the equations presented in Section (3.2.1).
Figure (5.2) shows the history of the displacement at the center of the plate obtained in both the simulations.

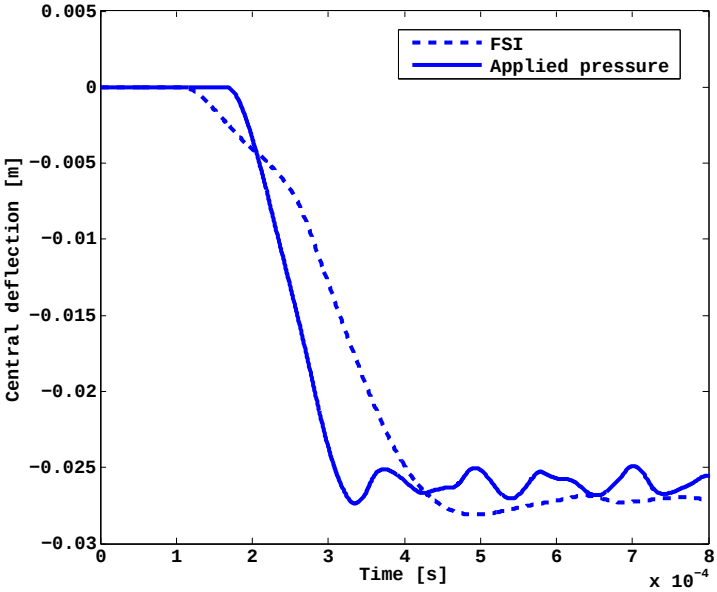

Figure 5.2: Central plate deflection versus time obtained in the simulations with an applied pressure profile and considering fluid-structure interaction (FSI).

The maximum central deflection computed in the fluid-solid coupled simulation is equal to 28.10 mm while the maximum central deflection obtained by applying a prescribed pressure profile is equal to 27.35 mm. The maximum central deflection recorded in the experiment is equal to 28.83 mm and agrees well with the results of both the numerical simulations. However, as expected, the fluid-solid coupled simulation better approximates the experimental result.

Besides the computed maximum deflection, also the maximum plastic deformation (representing the irreversible damage suffered by the plate) is very similar in both the numerical simulations. However, the deformation time scale in the two analyses is quite different: the maximum displacement is reached in $3.35\times10^{-4}s$ during the simulation in which a pressure profile is applied and is reached in $4.92\times10^{-4}s$ during the fluid-solid coupled simulation. If the fluid-structure interaction (FSI) is considered, the deformation process is divided in mainly two parts: when the first shock wave hits the plate, the plate starts moving away from the water, which is unable to immediately follow it and therefore cavitates. This phase corresponds to the lower slope of the first part of the deformation history obtained in the fluid-solid coupled simulation. Subsequently, a second pressure wave reaches the plate and this event coincides with the sharp gain in slope observed in the displacement history during the fluid-solid simulation. Another difference between the two displacement histories concerns the final oscillations of the plate, which are due to the remaining elastic part of the energy. These oscillations are slower, as expected, if water is present on the back side of the plate and are otherwise completely unconstrained and faster if only the solid shell is present (once the applied pressure has decayed to zero). Figure (5.3) shows the complete deformed shape of the plate corresponding to the instant when the maximum deflection is reached in both analyses and it is possible to see the good agreement between the two.

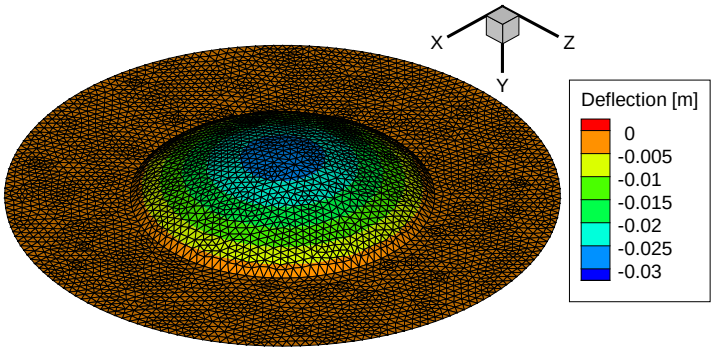

(a) Contour plot for the plate deflection obtained in the analysis which uses an applied pressure profile at time 3.35×10^{-4} s.

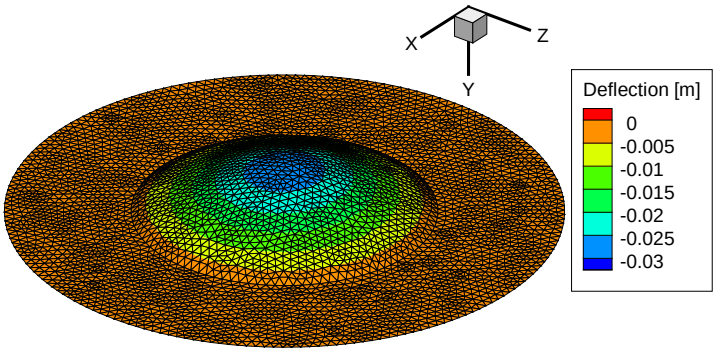

(b) Contour plot for the plate deflection obtained in the fluid-solid coupled analysis at time 4.92×10^{-4} s.

Figure 5.3: Deformed configuration of the plate corresponding to the instant of maximum deflection.

The final applied total work is another global measure that can be used to assess the differences between the two loading methods. Figure (5.4) shows the external work applied to the plate using a prescribed pressure profile and a fluid-solid coupled simulation. Although the two methodologies are very different, the maximum difference in the applied external work is only equal to 6.9%.

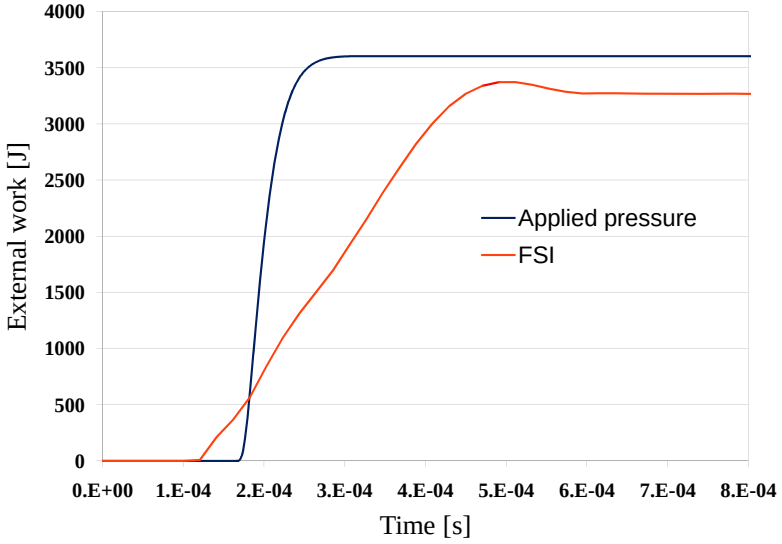

Figure 5.4: External work applied to the circular plate versus time during a shell-only and a fluid-shell coupled analysis.

It appears that an applied pressure profile may be used to approximate the load due to an underwater explosion during preliminary analyses aimed, for instance, at the optimization of different design parameters. These analyses must in general be repeated many times in order to explore the entire space of the design parameters of interest. A reliable but efficient computational tool is thus desirable to perform those optimization and first order analyses. However, a more accurate modeling of the fluid structure interaction is necessary to study the response of the final structure of interest (i.e., the boat hull that will be, or has been, fabricated). In this work the same approach has been followed: first a prescribed pressure profile is used to assess the role of chosen design parameters on the sandwich external face sheets and then the optimized design, together with fluid-solid coupled simulations, is used in the study of the final structure of interest.

5.2 Design optimization of fiber reinforced composite panels using a parametric study

The role of fiber volume fraction and fiber orientation in the design of the sandwich panel external faces is investigated. A square plate with side length equal to 4 m and thickness equal to 40 mm is considered. The applied pressure profile represents the detonation of

a 50 g TNT charge placed under the center of the plate at a distance equal to 0.2 m. According to the equations reported in Section (3.2.1) the maximum pressure applied when the shock wave hits the plate is initially equal to 104.5 MPa. The computational mesh and the sandwich material configuration are shown in Figure (5.5). The finite element mesh is composed of 2,048 shell elements with 3,267 displacement degrees of freedom. The mesh is pre-fractured at the beginning to locate cohesive elements between shell elements in order to allow for fracture and fragmentation if these occur due to the explosive load.

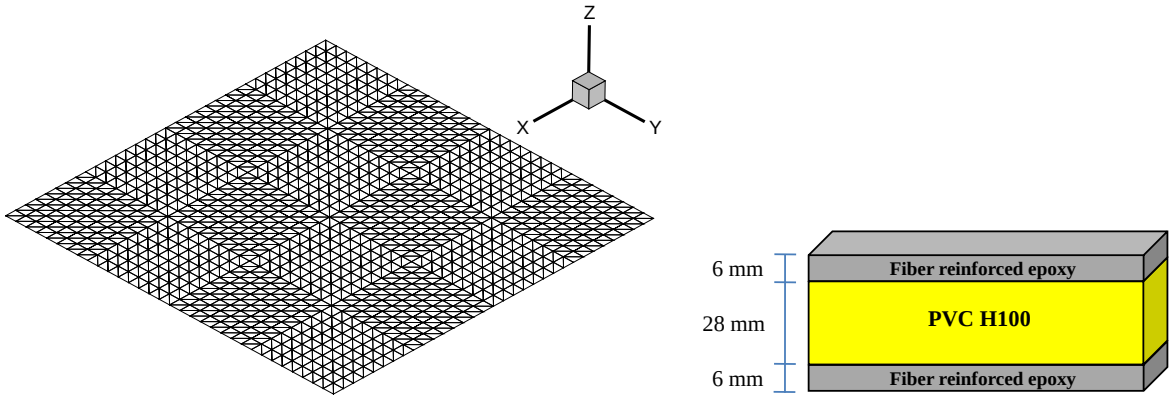

(a) Plate finite element mesh.

(b) Sandwich material configuration.

Figure 5.5: Geometry setup used in the factorial design analyses.

The sandwich panel is composed of a foam core made of PVC H100 and two external fiber composite layers made of carbon fibers and epoxy resin. Two groups of fibers are included in the composite material. The foam material properties have been taken from ElSayed (2008) while the fiber composite material properties have been taken from Yokozeki et al. (2007), Yu et al. (2002) and Inaba and Shepherd (2009a). The material behaviors of the foam core and of the fiber composite are described using the material models discussed in Sections (2.1) and (2.2) while the material properties used in the analyses are listed in Tables (5.2) and (5.3).

Foam core	
Mass density	100 kg/m^3
Initial Young's modulus before cell collapse	0.105 Gpa
Poisson ratio	0.32
Final Young's modulus after cell collapse	1.0 Gpa
Tensile strength	3.5 MPa
Compressive strength before cell collapse	-2.0 MPa
Final compressive strength	-50.0 MPa
Critical opening displacement	4.4e-5 m

Table 5.2: Material properties for PVC H100 foam core. The foam material behavior in uni-axial compression is represented in Figure (2.5).

Epoxy resin	
Mass density	1208 kg/m^3
Young's modulus	2.83 Gpa
Poisson ratio	0.25
Tensile strength	68 MPa
Carbon fibers	
Mass density	1780 kg/m^3
Young's modulus	215 Gpa
Tensile strength	3800 MPa
Composite	
Critical opening displacement	2.65e-5 m

Table 5.3: Material properties for epoxy resin reinforced with carbon fibers.

In the following analyses geometry, loading conditions and all but two material parameters remain constant. The fiber volume fraction of the external face sheets varies between 0.2 and 0.7 assuming 5 equally spaced values. The angle between the two families of fibers that compose the sandwich external layers also varies from 0^o (all the fibers are aligned in one direction) to 90^o (fibers are divided in two equal fractions and oriented in orthogonal directions) assuming 5 equally spaced values.

At the end of the analyses, the performance of the analyzed plates is evaluated on the basis of two global measures: the total elastic energy stored in the sandwich panel and the elastic energy stored in the foam core only. These energies have been chosen as primary indices to evaluate the plate performance because higher elastic energy stored in the material means that more energy due to the explosion has been absorbed and less energy has been dissipated through fracture and fragmentation induced structural damage.
The values of the elastic energy stored in the entire sandwich panel and in the core only are reported in Tables (5.4) and (5.5), respectively, and are plotted in Figures (5.6) and (5.7).

V_f \ θ	0^o	22.5^o	45^o	67.5^o	90^o
0.2	2239	2472	5024	8100	9030
0.325	2515	3180	6782	12301	13023
0.45	3072	3554	8105	15066	16454
0.575	4116	4080	10136	15920	17989
0.7	4324	4322	11730	17289	18970

Table 5.4: Total elastic energy stored in the sandwich panel as a function of fiber volume fraction V_f and fiber angle. θ represents the angle between two families of fibers.

V_f \ θ	0^o	22.5^o	45^o	67.5^o	90^o
0.2	220	310	473	749	857
0.325	280	305	662	1156	1192
0.45	358	369	809	1476	1499
0.575	472	441	1089	1575	1676
0.7	560	561	1394	1766	1928

Table 5.5: Elastic energy stored in the sandwich core as a function of fiber volume fraction V_f and fiber angle. θ represents the angle between two families of fibers.

As clearly visible in Tables (5.4) and (5.5), the computed values of the elastic energy stored in the entire sandwich plate or in the foam core alone vary by up to an order of

magnitude depending on fiber volume fraction and fiber orientations. This confirms that both fiber volume fraction and fiber orientation have a significant effect in determining the energy absorbed by the sandwich panel subjected to an explosive load. The optimization of these design parameters is therefore meaningful to improve the sandwich structure final response when subjected to an underwater explosion.

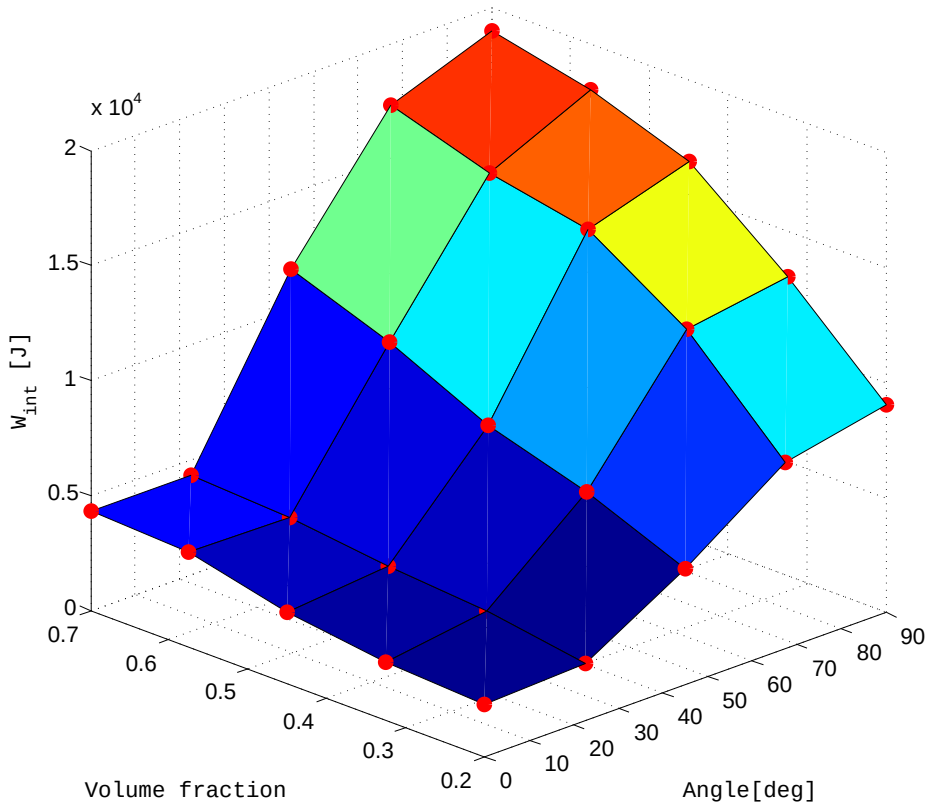

Figure 5.6: Total elastic energy stored in the sandwich plate as function of fiber angle and fiber volume fraction.

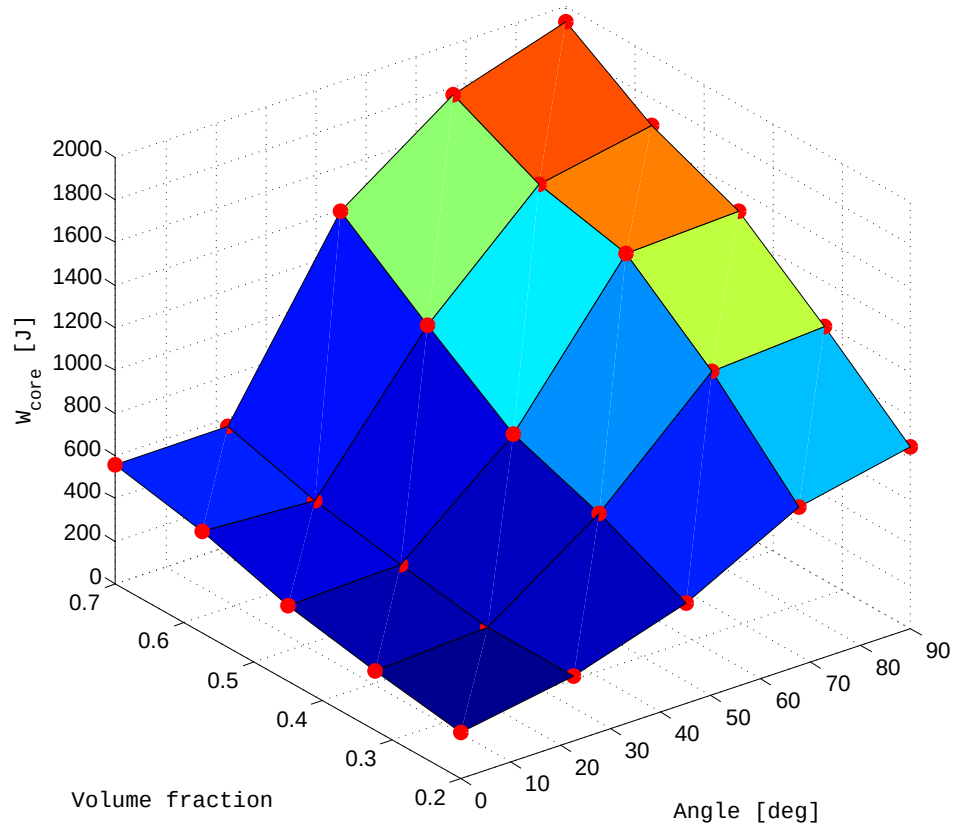

Figure 5.7: Elastic energy stored in the sandwich foam core as function of fiber angle and fiber volume fraction.

The elastic energy stored in the entire sandwich panel increases, although non-linearly, with the increasing volume fraction and angle between two families of fibers. The elastic energy absorbed in the panel is maximized if the fiber volume fraction is equal to 0.7 and if the fibers are divided equally into two orthogonal families. A greater fiber volume fraction corresponds to a higher local cohesive strength of the composite materials in the face sheets. Moreover, if two orthogonal families of fibers are present, there is no preferential direction for fracture propagation. Therefore, the design that corresponds to the maximum stored elastic energy also corresponds to the design with the highest resistance to fracturing. When the explosive load is applied to the sandwich plate, fracture and fragmentation are reduced if this design is used, and a greater part of the explosion energy may be converted into elastic energy.

The increase in stored elastic energy does not depend equally on the fiber volume fraction and on the angle between two families of fibers. Figures (5.8) and (5.9) represent the

absorbed elastic energy as a function, separately, of fiber volume fraction and fiber angle. Figures (5.8) and (5.9) are obtained by averaging respectively over the columns and over the rows of Table (5.4). It can be seen that the stored elastic energy increases almost linearly with respect to fiber volume fraction and non-linearly as a function of fiber angle. As written in Equation (2.17), the final cohesive strength of the material depends in the same linear way on fiber volume fraction and non-linear way on fiber angle. This aspect confirms that sandwich external layers with higher cohesive strength and therefore greater resistance to fracturing will absorb more elastic energy and sustain less structural damage.

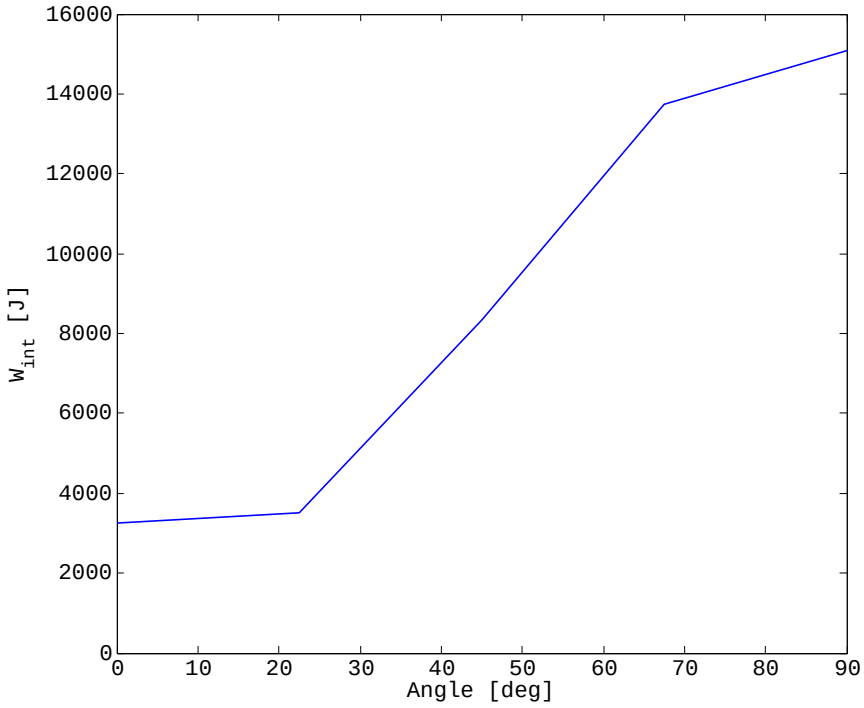

Figure 5.8: Total elastic energy stored in the sandwich plate as function of fiber angle.

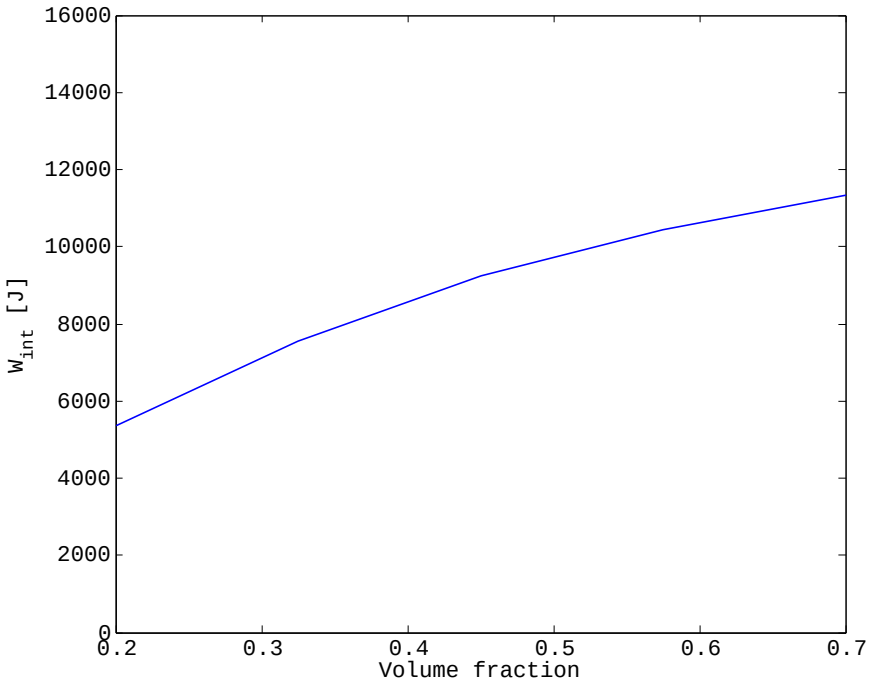

Figure 5.9: Total elastic energy stored in the sandwich plate as function of fiber volume fraction.

Qualitatively, the amount of elastic energy stored in the foam core depends on fiber volume fraction and fiber angle in the same manner as the total stored elastic energy does. Figure (5.10) shows the foam core elastic energy as a non linear function of fiber angle and Figure (5.11) reports the almost linear dependence on fiber volume fraction. Similarly to the observations relative to the total stored elastic energy, stronger external face sheets also enable higher elastic energy to be stored in the foam core. It can therefore be concluded that the foam core contributes more to the total resistance of the sandwich panel if stronger face sheets are used.

In order to optimize the role of the foam core in absorbing part of the energy due to an explosion, orthogonal fibers and high fiber volume fraction in the face sheets are recommended.

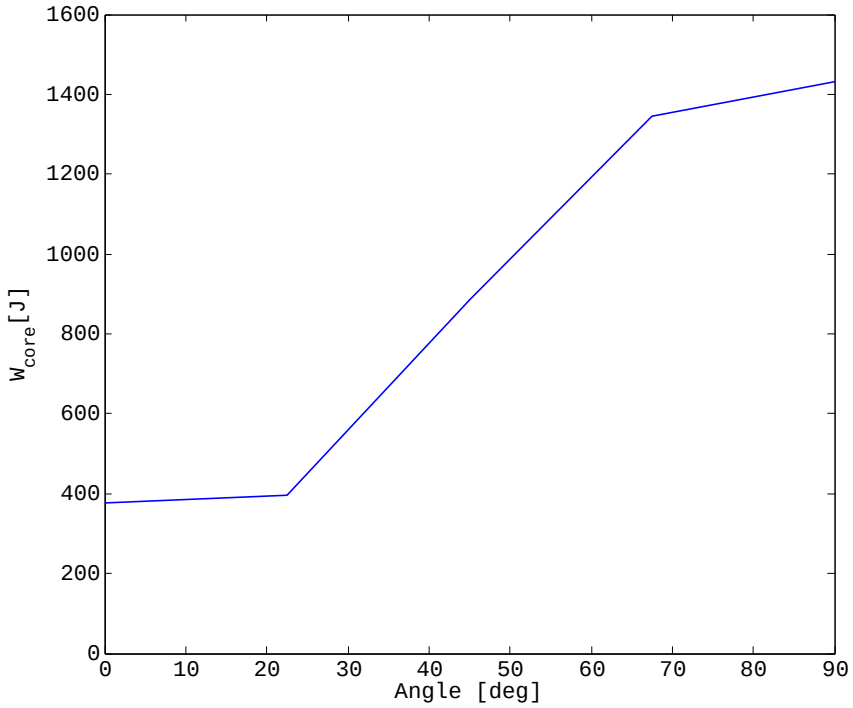

Figure 5.10: Elastic energy stored in the sandwich foam core as a function of fiber angle.

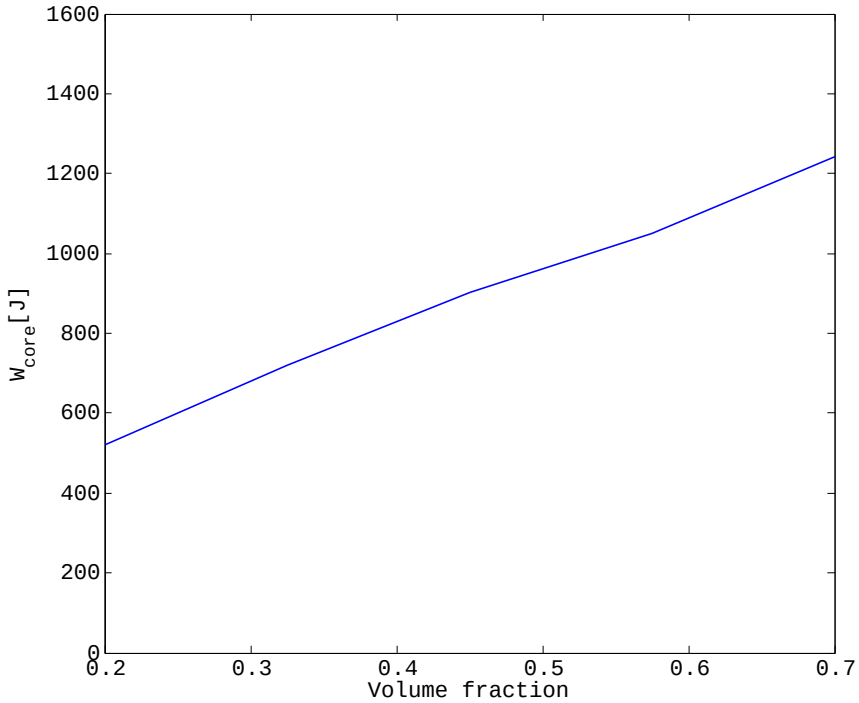

Figure 5.11: Elastic energy stored in the sandwich foam core as a function of fiber volume fraction.

Figure (5.12) shows the final deformation and damage for the two limiting cases of the

factorial design: in the first analysis, one family of fibers is present in the external face sheets and a fiber volume fraction equal to 0.2 is used. In the second analysis, the opposite limit is considered: two orthogonal families of fibers are considered in the external face sheets and the fiber volume fraction is equal to 0.7. In Figure (5.12), it is clearly visible that greater damage is present when only one family of fibers with volume fraction equal to 0.2 is used.

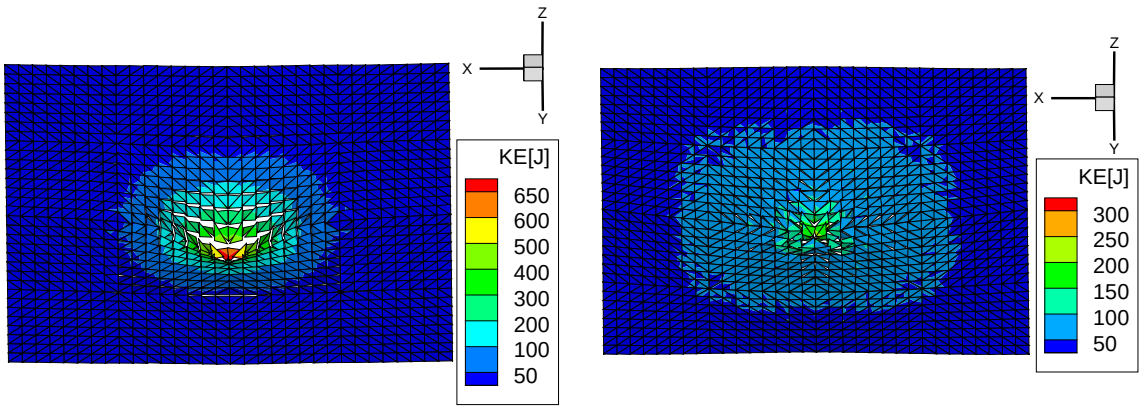

(a) Fibers oriented only along the X axis and fiber volume fraction equal to 0.2 .

(b) Fibers oriented along the X and Y axes and fiber volume fraction equal to 0.7 .

Figure 5.12: Final deformed configuration and kinetic energy contour plot relative to the plates with design parameters at the extremes of the parametric study.

The results of the presented parametric study are confirmed in the analysis of the response of two sections of a cylindrical shell subjected to an underwater explosion. The thickness of the considered cylindrical shell is 20 mm: the foam core is 14 mm thick and each fiber composite face sheet is 3 mm thick. The mass of the TNT charge is equal to 0.2 kg and is placed at 0.4 m from the cylinder surface. The fiber volume fraction is constant in the two analyses and is equal to 0.4; however in analysis A all the fibers are oriented along the cylinder axis, whereas in analysis B half of the fibers are oriented along the axis of the cylinder, and the remaining are oriented in the circumferential direction. The material properties used in the analyses are the same as the ones reported in Tables (5.2) and (5.3).

Once the pressure load due to the underwater explosion has been completely applied:

- The damage is greater in analysis A as can be seen qualitatively in Figure (5.13).

- The total elastic energy stored in the structure is equal to about 8,000 J and 14,000 J in analyses A and B, respectively. If two orthogonal families of fibers are present, a greater part of the external work due to the TNT explosion is converted into elastic energy and minor damage is observed.

- The dissipated cohesive energy is equal to 3,985 J and 2,304 J in analyses A and B, respectively (Figure 5.14). The dissipated cohesive energy is directly proportional to the extent of fracture and fragmentation and therefore to the present structural damage. This confirms that the shell with two orthogonal families of fibers better sustains the underwater explosion.

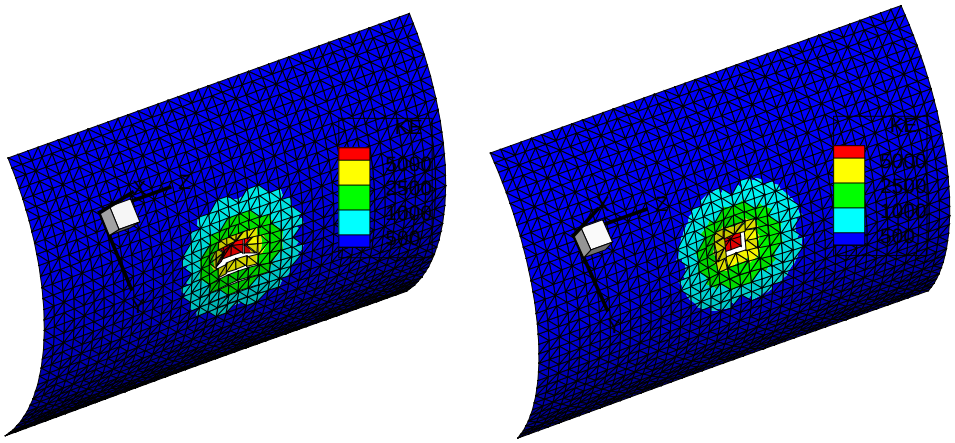

(a) One family of fibers oriented along the cylinder axis.

(b) Two sets of fibers oriented along the cylinder axis and in the circumferential direction.

Figure 5.13: Final deformed configuration.

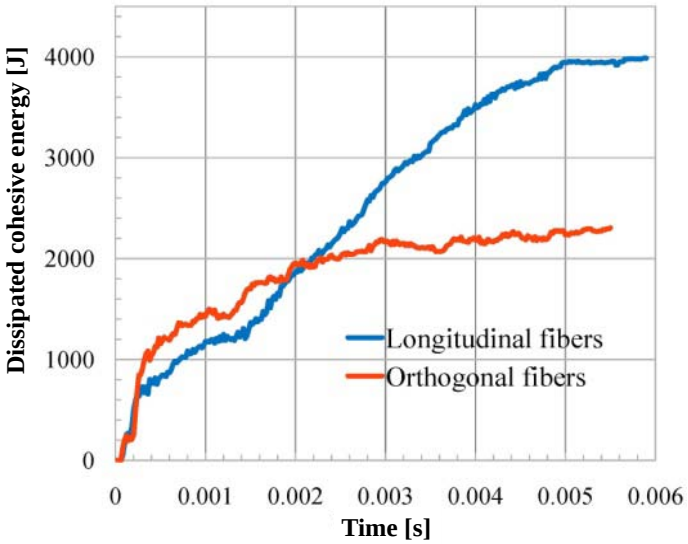

Figure 5.14: History of dissipated cohesive energy.

Analysis / Energies	A	B
Elastic energy [J]	8000	14000
Dissipated cohesive energy [J]	3985	2304

Table 5.6: Final elastic energy and dissipated cohesive energy computed in the analyses A and B.

5.3 Capability of different hull cross sections to contain explosive loads

The use of metal face sheets constitutes an alternative to the use of external layers made of fiber reinforced composites. In view of maintaining a low weight of the sandwich panel, aluminum face sheets are considered and compared to fiber reinforced external layers. In a first set of analyses, square sandwich plates with side length equal to 4.0 m are considered. The core thickness is constant in all the analyses and is equal to 70 mm while the thickness of the external face sheets varies in order to maintain a constant weight of the sandwich panel. The total weight of the sandwich panel represents a crucial factor in designing naval structures, and it is therefore important to compare the performance of

different sandwich panels normalized with respect to the panel weight. The characteristics of three different plates used in the analyses are summarized in Table (5.7).

	Fiber composite and foam	Aluminum and foam	Fiber composite only
Total thickness [mm]	100.0	88.7	34.0
Face sheet thickness [mm]	15.0	8.9	-
Core thickness [mm]	70.0	70.9	-
Specific weight [kg/m^2]	55.3	55.3	54.7

Table 5.7: Plate sandwich material configurations.

The mesh used in the analyses is the same as the one represented in Figure (5.5(a)) and consists of 2,048 shell elements. The elements are pre-fractured at the beginning to allow for fracture and fragmentation. The material properties for the epoxy resin and the carbon fibers are the same as the ones reported in Tables (5.2) and (5.3). The employed material models have been discussed in Sections (2.1) and (2.2). The material behavior of aluminum is described by a J_2 plasticity model with power law hardening and rate dependency. The aluminum material properties are taken from Cirak et al. (2005) and are reported in Table (5.8).

Mass density	2719 kg
Young's modulus	69000 Mpa
Yield stress	90 MPa
Poisson ratio	0.33
Reference plastic strain	0.001
Hardening exponent (1/n)	4.0
Reference plastic strain rate	0.0001
Rate sensitivity exponent (1/m)	0.01
Cohesive strength	180 MPa

Table 5.8: Material properties for aluminum Al2024-0.

The sandwich panels are simply supported on the boundaries and are subjected to the pressure load corresponding to the detonation of an underwater 0.2 kg TNT charge placed at 0.4 m vertically under the center of the plate. The maximum pressure generated by the underwater explosion is equal to 89.9 MPa.

If fiber reinforced face sheets are used as opposed to aluminum face sheets:

1. the kinetic energy of the plate is lower indicating a lower structural damage. Moreover, as visible in Figure (5.15) the kinetic energy of the sandwich plate with fiber

composite face sheets reaches a maximum and then markedly decreases, meaning that the plate has contained the pressure due to the explosion and is slowing its motion. On the contrary, the kinetic energy of the aluminum sandwich shells does not decrease markedly after reaching its maximum. This is due to the presence both of fragments detached from the main plate and of cracks in the sandwich panel which reduce the structural stiffness of the sandwich plate.

2. The elastic energy stored in the sandwich core is higher, indicating that a greater part of the explosion energy has been absorbed in the core (Figure 5.16).

3. The fractured cross section area is lower (Figure 5.17). The surface of the fractured cross section is computed by dividing the dissipated cohesive energy by the mean fracture energy of the sandwich cross section which is computed averaging the fracture energy of the external face sheets and of the internal foam core based on their relative thickness. The average fracture energy for the sandwich cross section with fiber composite and aluminum face sheets is equal to 10708 N/m and 1850 N/m respectively.

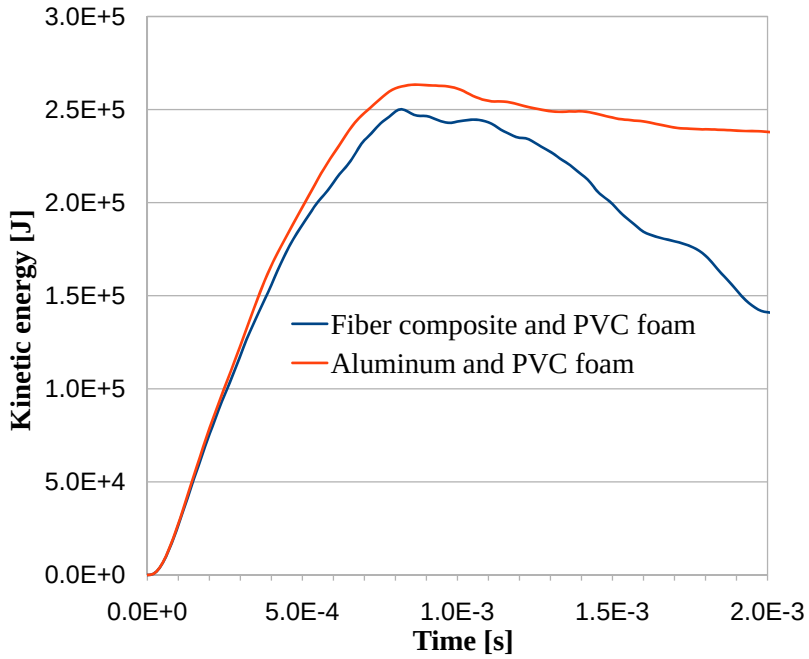

Figure 5.15: History of the kinetic energy of simply supported 4 m × 4 m sandwich plates with different face sheet materials subjected to an underwater explosion.

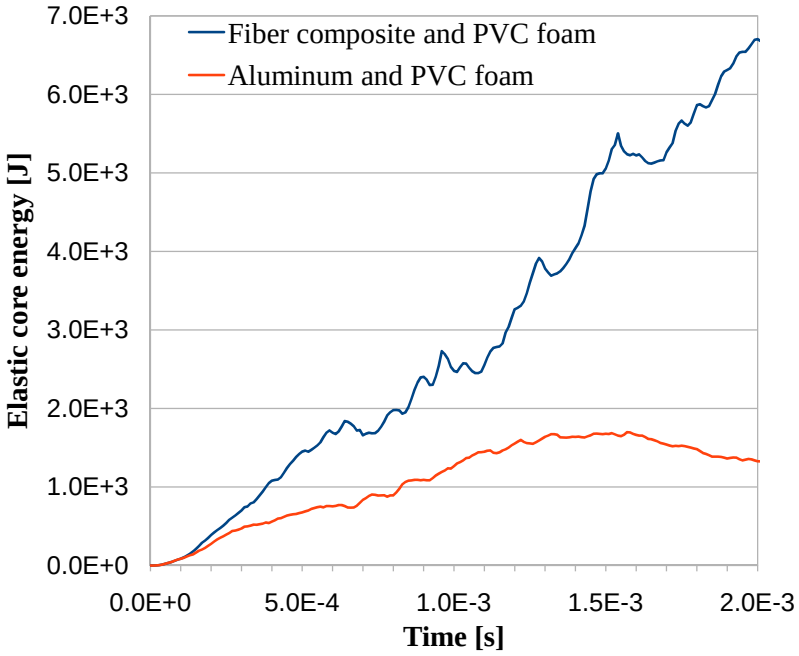

Figure 5.16: Evolution of the elastic energy stored in the foam core of simply supported 4 m $\times$ 4 m sandwich plates with different face sheet materials subjected to an underwater explosion.

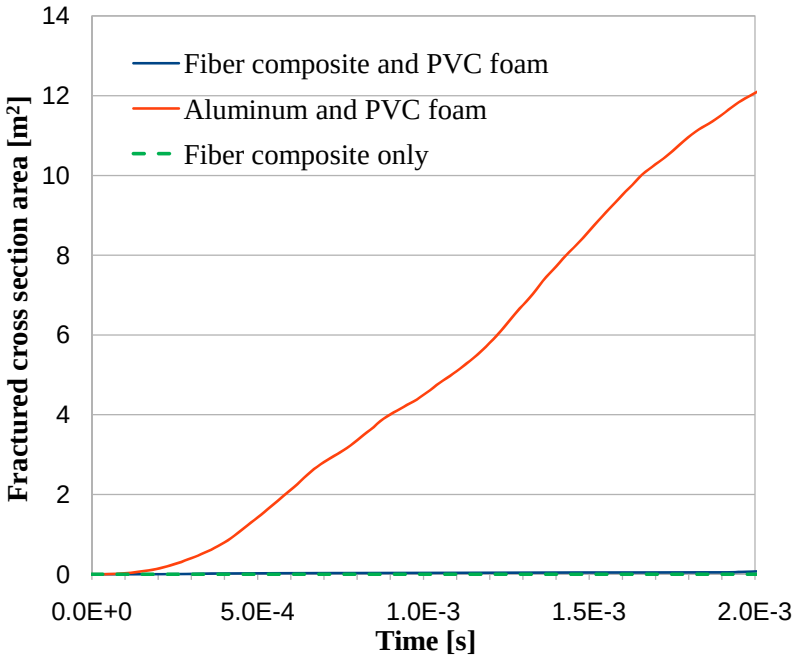

Figure 5.17: Fracture propagation history for simply supported 4 m $\times$ 4 m sandwich plates with different face sheet materials subjected to an underwater explosion.

The analyses just described have been repeated using a smaller square sandwich panel with sides of length equal to 2.0 m and thickness equal to 70 mm. In this second set of analyses the applied pressure profile corresponds to a TNT charge equal to 0.15 kg placed at 0.25 m below the plate center. The maximum pressure applied to the plate is equal to 126.9 MPa, and larger structural damage is inflicted. Figures (5.18), (5.19), and (5.20) confirm the observations relative to the first set of analyses.

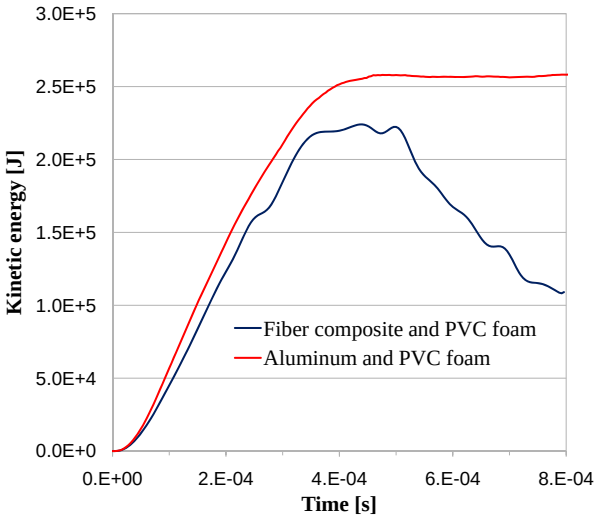

Figure 5.18: History of the kinetic energy of simply supported 2 m $\times$ 2 m sandwich plates with different face sheet materials subjected to an underwater explosion.

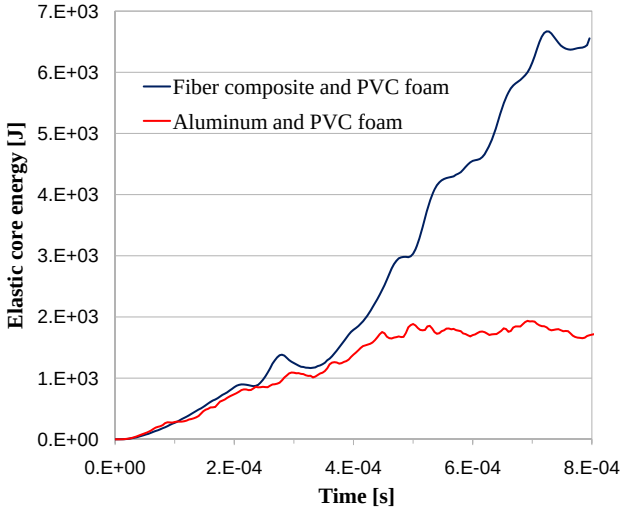

Figure 5.19: Evolution of the elastic energy stored in the foam core of simply supported 2 m $\times$ 2 m sandwich plates with different face sheet materials subjected to an underwater explosion.

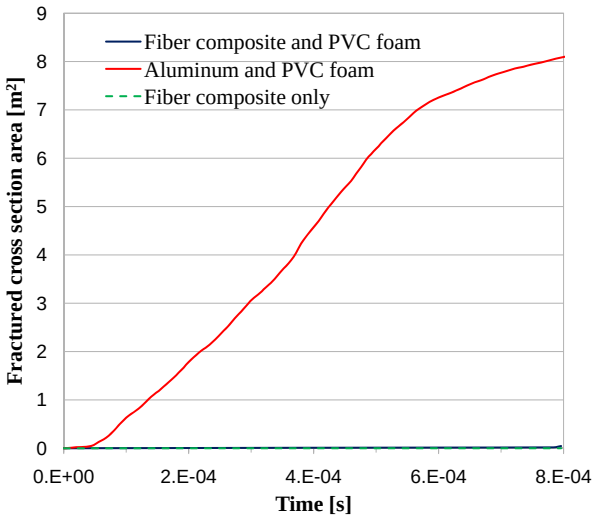

Figure 5.20: Fracture propagation history for simply supported 2 m × 2 m sandwich plates with different face sheet materials subjected to an underwater explosion.

Although interlayer delamination between the foam core and the external face sheets is not simulated and addressed in the present work, it is worth mentioning that fiber reinforced sandwich panels are expected to offer also a greater resistance to delamination in comparison to sandwich panels with aluminum external layers. Indeed, it is expected that the inner surface in contact with the foam core is, in general, more rough in the case of fiber reinforced external layers, therefore offering a greater interlocking between the foam core and the external face sheets and consequently a higher interlayer cohesive strength.

As it is possible to see from Figures (5.17) and (5.20), a plate made exclusively of fiber composite material sustains the load as well as a sandwich plate with fiber composite face sheets and of equal weight. However, as it appears from Figure (5.21), the plate made of only fiber composite material undergoes a larger deflection if subjected to the same pressure load than a sandwich plate of equal weight (the pressure load used in this last set of analyses is due to a small TNT charge equal to 0.1 kg placed 1.0 m below the plate center and does not cause structural damage). Usual structural applications require the maximum deformation to be limited. Therefore, even if both the sandwich fiber composite plate and the fiber-only composite plate sustain an explosive load equally well, the first is preferred in structural applications.

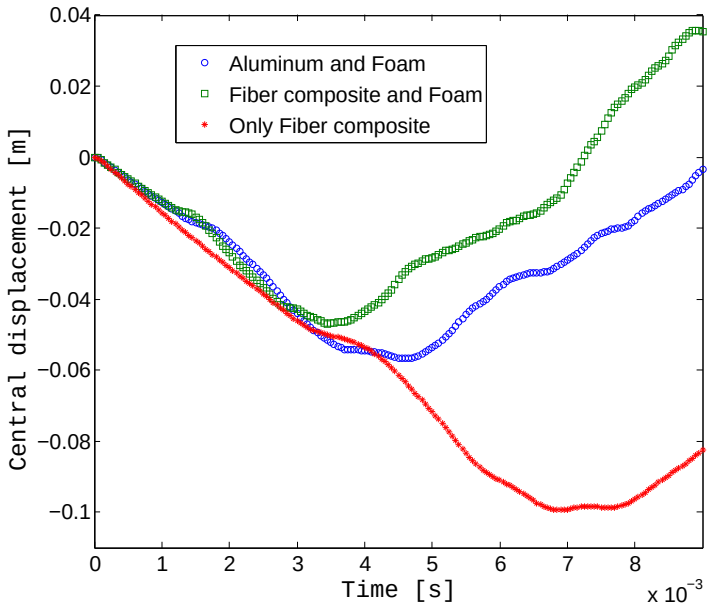

Figure 5.21: Simply supported 4 m × 4 m square plates subjected to a small underwater explosion: deflection history.

5.4 Fluid-solid coupled simulations of fiber reinforced sandwich hulls

As a final application, the present computational capability is used to investigate the response to an underwater explosion of a hull section of a Meko 140 corvette ship used by the Argentinean navy. The geometry of the hull section is taken from ElSayed (2008) and is shown in Figure (5.22).

An 8.3 m long hull section is modeled using 2,880 shell finite elements which are pre-fractured at the beginning to allow fracture and fragmentation. The fluid domain is discretized using 344,400 finite volume cells and contains the entire solid domain. A sandwich material configuration is considered for the hull cross section. The total thickness of the hull is equal to 100 mm and is composed of two external fiber-composite face sheets and a foam core. The finite element mesh and the sandwich material configuration are shown in Figure (5.23).

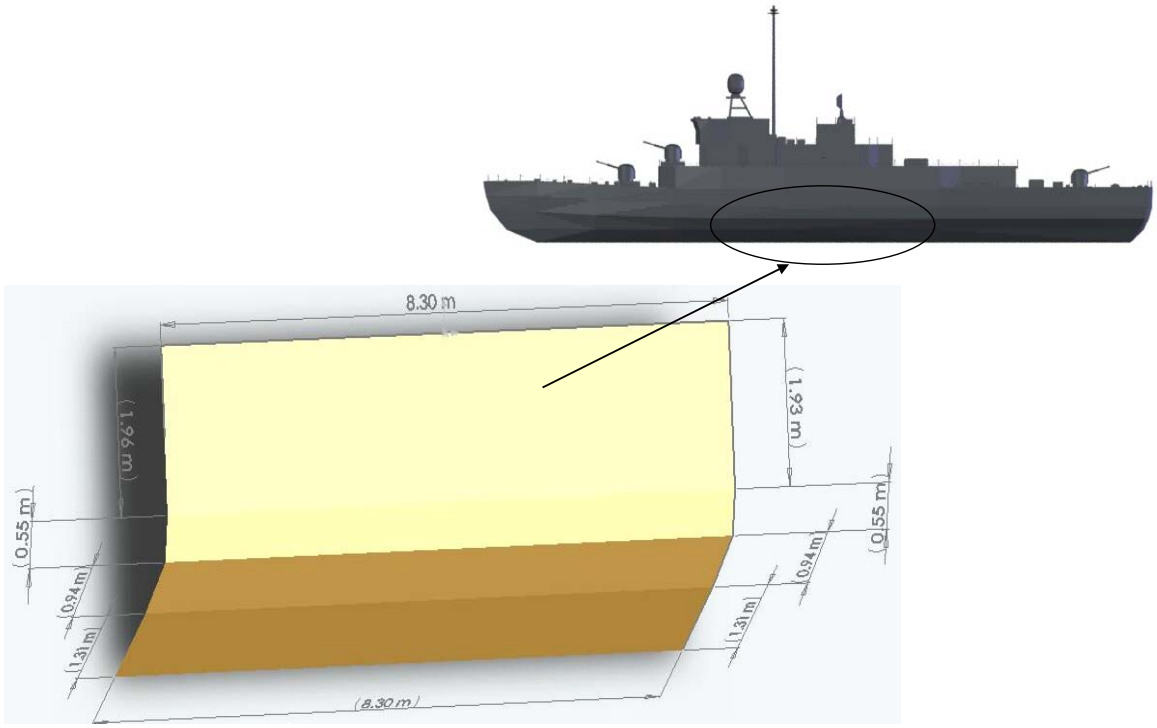

Figure 5.22: Side view of the Meko 140 corvette ship and geometry of the hull section used in the numerical simulations.

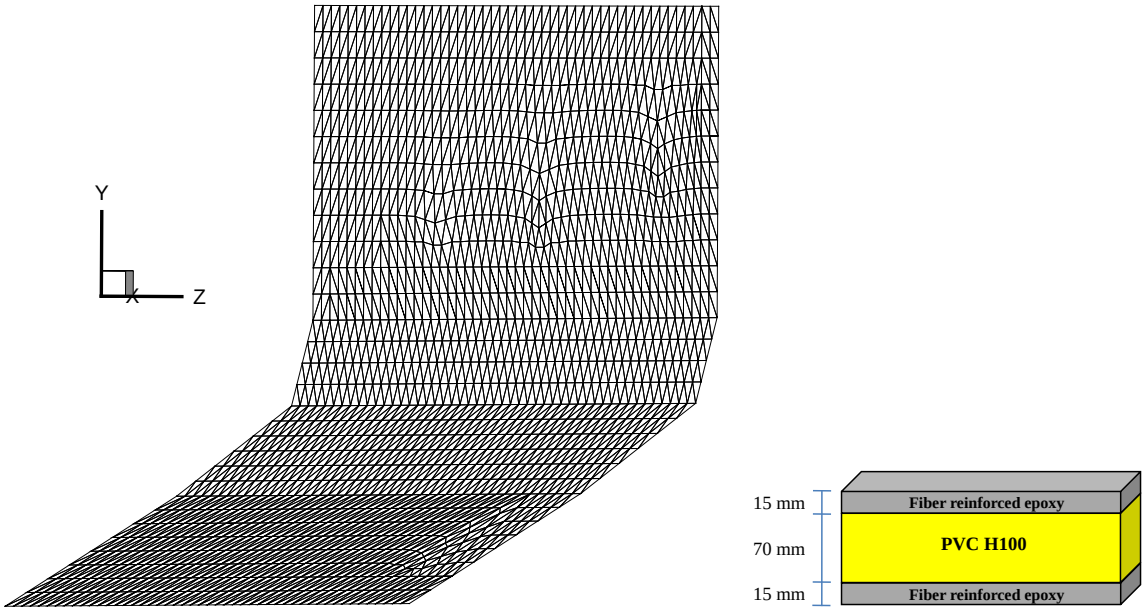

(a) Hull finite element mesh.

(b) Sandwich material configuration.

Figure 5.23: Analysis geometry.

The fiber composite external layers are made of epoxy resin and carbon fibers for which

the material properties are reported in Table (5.3) and the material model is described in Section (2.2). The foam core is made of PVC H100 with material properties listed in Table (5.2) and material model described in Section (2.1) .

The hull section is simply supported at its boundaries and is subjected to five different loading conditions with varying mass of the TNT charge and its distance from the vessel hull as reported in Table (5.9)

Analysis ID	TNT mass	Charge distance
Hull-m1-d05	1 kg	0.5 m
Hull-m1-d1	1 kg	1.0 m
Hull-m10-d05	10 kg	0.5 m
Hull-m10-d1	10 kg	1.0 m
Hull-m20-d05	20 kg	0.5 m

Table 5.9: Loading conditions considered in the simulations of the hull section subjected to an underwater explosion.

Figure (5.24) reports the dissipated cohesive energy at the end of each analysis; the hull damage is directly proportional to the dissipated cohesive energy. As expected, the damage inflicted on the hull increases with increasing charge mass and decreasing distance from the vessel. Moreover, the damage is contained for the analyses with charge mass equal to 1 kg and for the analysis with charge mass equal to 10 kg placed at a distance equal to 1.0 m from the hull. The underwater explosions caused by 10 kg and 20 kg of TNT placed at 0.5 m from the hull are instead able to cause major damage and fracture of the hull as seen in Figures (5.25) and (5.26). The damage caused by the 10 kg TNT mass is more extended than the one caused by the 20 kg TNT charge which is able to perforate the hull at the location where the shock wave first impacts the hull. The higher pressure due to a 20 kg TNT charge punctures the hull limiting the extension of fracture and fragmentation.

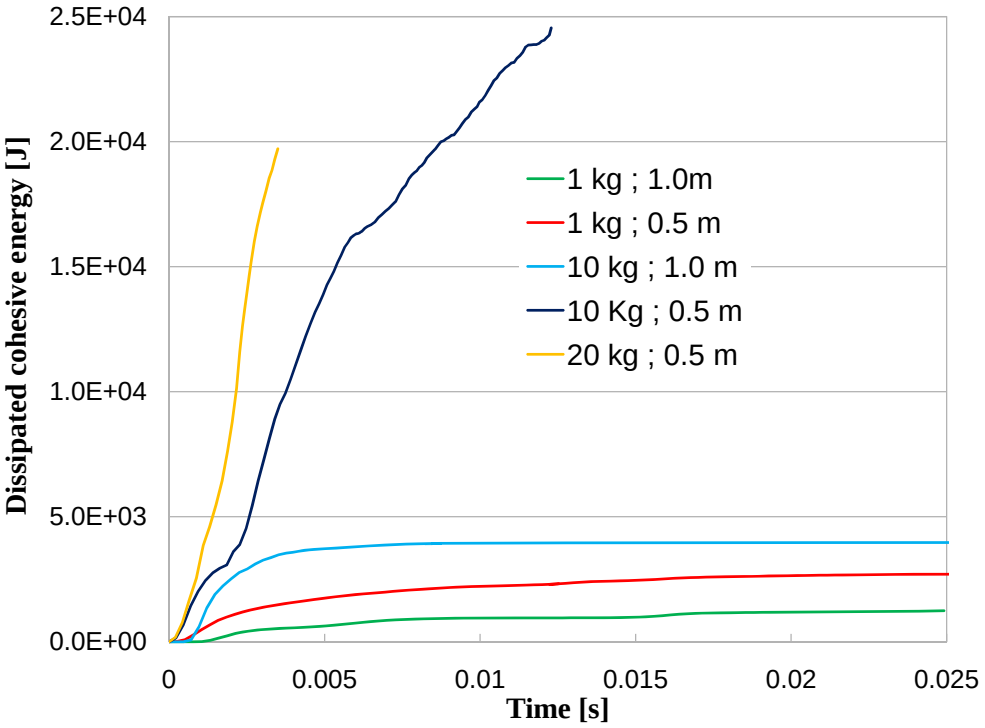

Figure 5.24: Dissipated cohesive energy during each analysis for which the mass and offset of the TNT charge are reported in the legend of the plot.

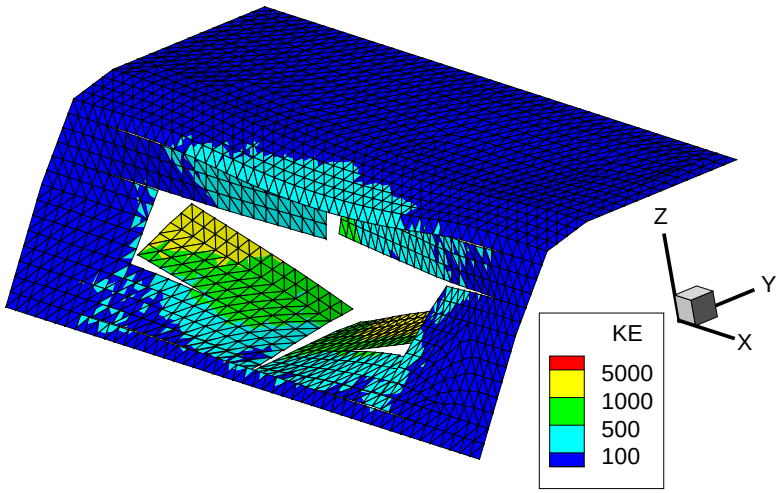

Figure 5.25: Final damage sustained by the hull subjected to the underwater explosion of a 10 kg TNT charge placed at 0.5 m from the vessel. The contour plot of the kinetic energy [J] is also shown.

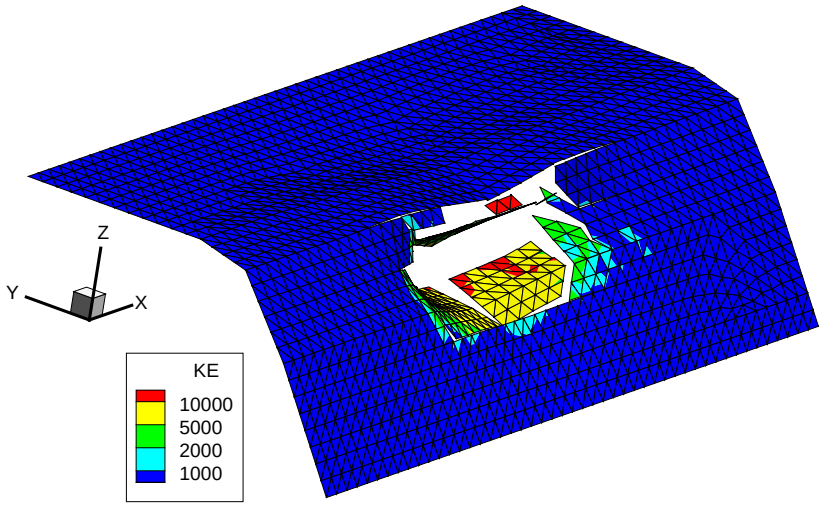

Figure 5.26: Final damage sustained by the hull subjected to the underwater explosion of a 20 kg TNT charge placed at 0.5 m from the vessel. The contour plot of the kinetic energy [J] is also shown.

Figures (5.27) - (5.30) show the fluid-solid coupled domain (viewed from inside the hull) during a sequence of time steps of the analysis in which a 20 kg TNT charge is detonated at 0.5 m from the hull. In Figure (5.27) the initial high pressure gas sphere representing the TNT explosion is shown together with the vessel hull in the initial configuration. Subsequently, the high pressure sphere expands, reaches the hull (Figure 5.28) and damages it (Figures 5.29 and 5.30).

Figure (5.31) shows, for the same analysis, the density contour plot at different times in the central section of the computational domain taken at x=0. The initial gas bubble formed by the TNT explosion reaches the vessel and breaks the hull connecting the water (red) and air (blue) parts of the fluid domain.

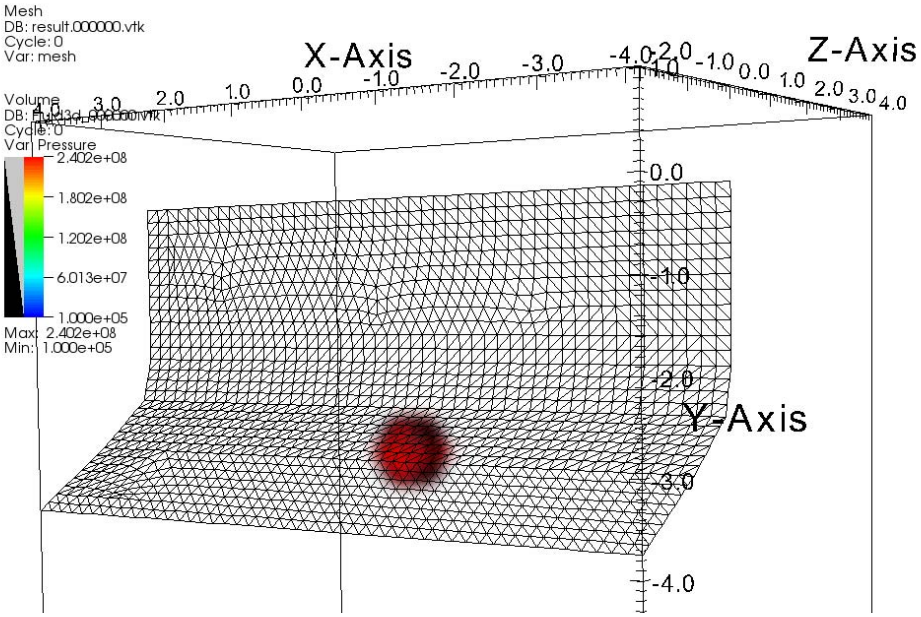

Figure 5.27: Hull mesh and pressure contour plot at time t = 0.0 s for the analysis in which a 20 kg TNT charge is detonated at 0.5 m from the vessel (Pressure unit = Pa).

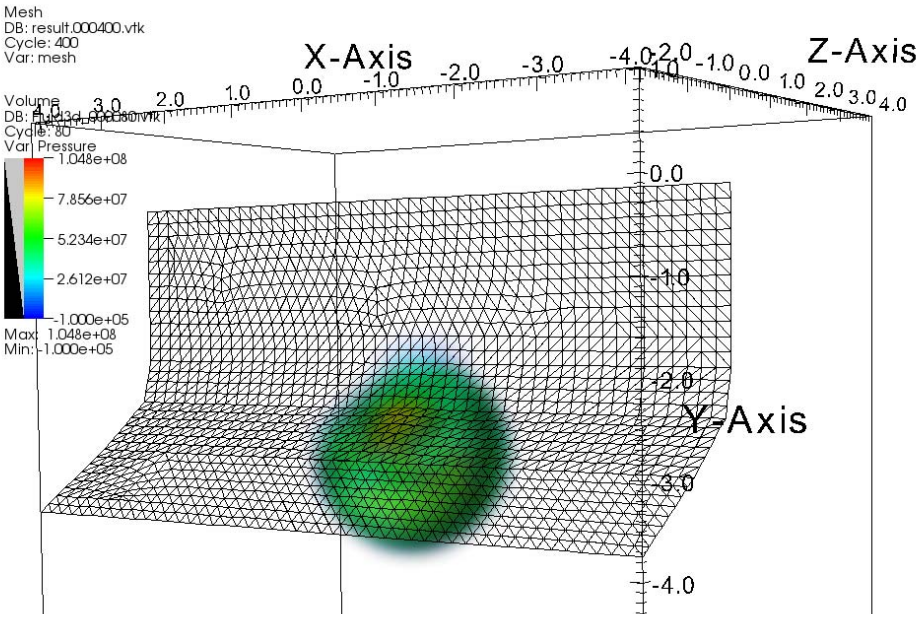

Figure 5.28: Hull mesh and pressure contour plot at time t = 4.2 $\times 10^{-4}$s for the analysis in which a 20 kg TNT charge is detonated at 0.5 m from the vessel (Pressure unit = Pa).

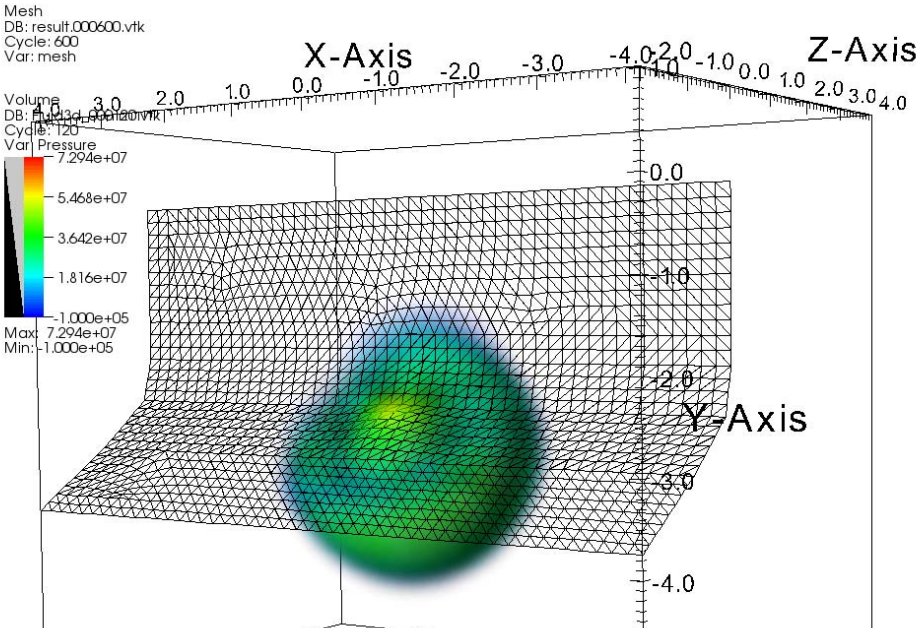

Figure 5.29: Hull mesh and pressure contour plot at time t = 6.5 $\times 10^{-4}$s for the analysis in which a 20 kg TNT charge is detonated at 0.5 m from the vessel (Pressure unit = Pa).

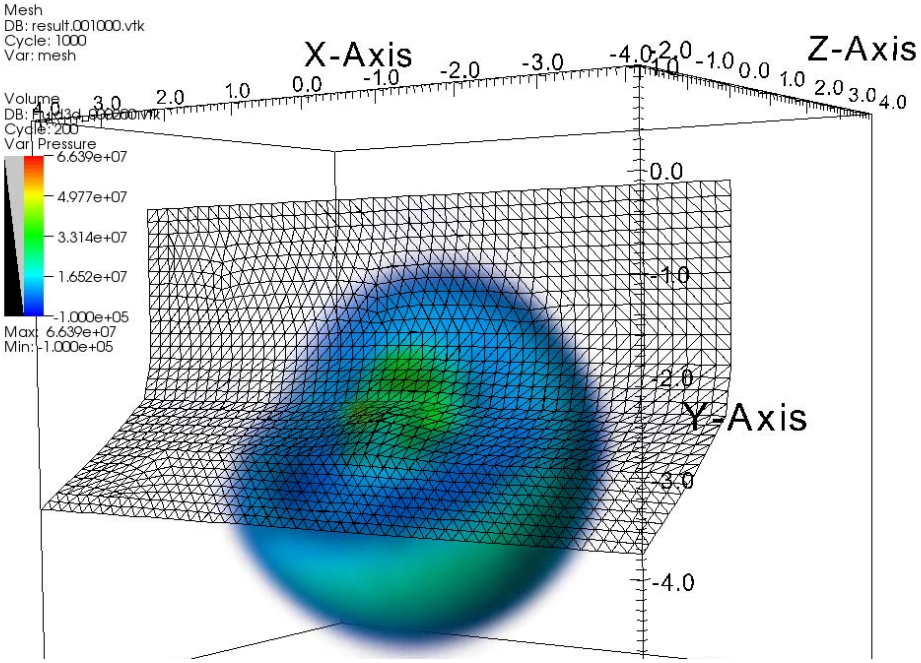

Figure 5.30: Hull mesh and pressure contour plot at time t = 10.0 $\times 10^{-4}$s for the analysis in which a 20 kg TNT charge is detonated at 0.5 m from the vessel (Pressure unit = Pa).

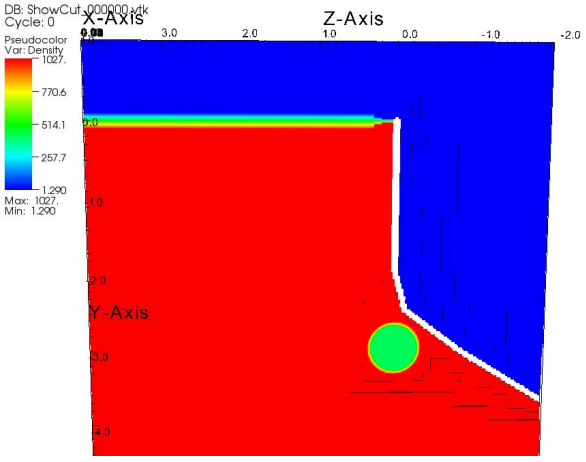

(a) Time = 0.0 s .

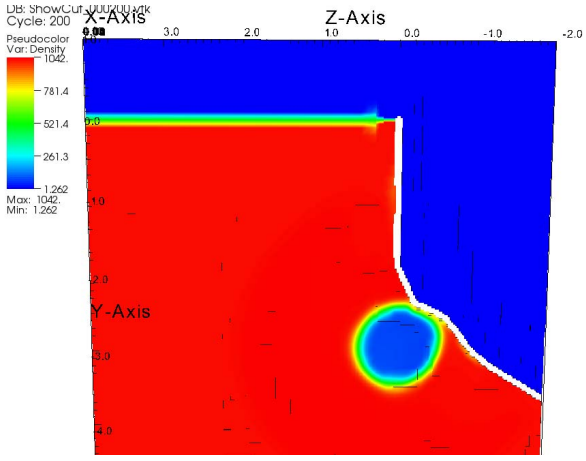

(b) Time = 10.0 $\times 10^{-4}$ s .

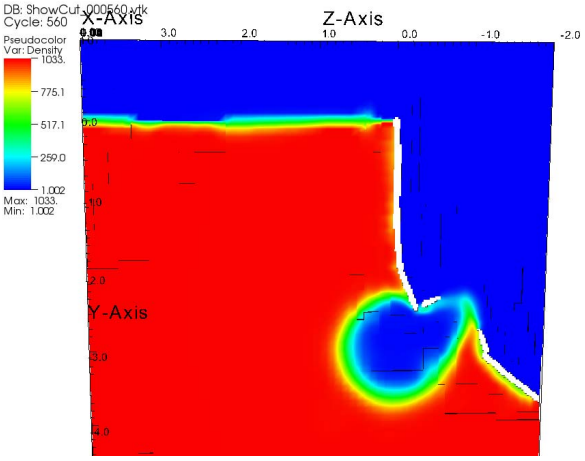

(c) Time = 23.6 $\times 10^{-4}$ s .

Figure 5.31: Density contour plot at different time steps for the analysis in which a 20 kg TNT charge is detonated at 0.5 m from the vessel (Density unit = kg/m^3).

Chapter 6

New approaches and improvements

Several detailed paths for future research are presented in the following sections. In particular, three areas of future research are recognized as particularly important to improve the predictive capability of the computational scheme: the study of a new shell finite element, a better description of the displacement field in the thickness of the sandwich shell finite element and a more detailed characterization of the damage occurring in the sandwich panel. Additionally, the coupling of the presented method with uncertainty quantification techniques is briefly discussed.

6.1 Beyond subdivision elements

One of the major drawbacks of the presented computational scheme is the need to prefracture the finite element mesh a priori. This not only increases greatly the number of degrees of freedom of the model but also requires a penalty approach to enforce elements' compatibility before any cracks start to propagate. A penalty approach often causes the ill-conditioning of the system of equations to be solved during the analysis and requires a reduction of the time step in dynamic analyses to avoid instabilities of the solution algorithm. Moreover, elements' compatibility is never enforced exactly before crack propagation and this contributes to the error in the analysis.

In order to improve the simulation of sandwich shells subjected to underwater explosions, a different finite element is needed that does not require prefracturing of the mesh. At the same time, the new shell finite element must retain optimal convergence properties

and therefore should not lock [1] in the thin limit.

In this spirit, two different approaches are currently under investigation and are presented in the following sections as candidates to improve the present computational capability. The first approach is based on the Mindlin-Reissner theory for shell/plate bending and uses the diamond approximation scheme introduced by Hauret et al. (2007) in incompressible elasticity. The diamond approximation scheme guarantees optimal convergence in the thin limit while the element interpolation functions remain local. Therefore there is no need to pre-fracture the mesh to handle complex topology changes, but cohesive elements may be inserted only when the crack starts to propagates.

The second approach presented is based directly on the three dimensional elasticity equations and utilizes the local maximum entropy interpolation scheme proposed by Arroyo and Ortiz (2006). As discussed by many authors (i.e., Noguchi et al. (2000), Krysl and Belytschko (1996), Li et al. (2000b)), meshless schemes greatly alleviate the locking problem in thin shells and are able to describe very large deformations such as the ones likely to be caused by an underwater explosion.

6.1.1 Diamond plate finite element

The concepts presented in Brezzi and Fortin (1991) and Ortiz and Morris (1988) are reviewed at the beginning of this section and serve to introduce the diamond approximation scheme presented later. Finally, the diamond plate finite element is described together with some preliminary results.

[1] A finite element is said to lock when its response is overly stiff. If not properly implemented, internal kinematic conditions may overconstrain a finite element, making it worthless. Examples of internal kinematic constraints are:

- in incompressible elasticity problems: $(div(\boldsymbol{u}) = 0)$ where $\boldsymbol{u}$ represents the displacement field.
- in thin plate problems: $(\nabla w - \boldsymbol{\theta} = 0)$ where w represents the displacement normal to the plate middle surface and $\boldsymbol{\theta}$ are the plate middle surface rotations.

6.1.1.1 The Mindlin plate problem in the continuum setting

The potential energy Π of a plate described by Mindlin theory and subjected to a distributed load q may be written as:

$$\Pi = \frac{t^3}{2} a\left(\boldsymbol{\beta}, \boldsymbol{\beta}\right) + \frac{\lambda t}{2} \int_{\Omega} (\nabla w - \boldsymbol{\beta})^2 dxdy - \int_{\Omega \times]-t,t[} qwdxdydz \tag{6.1}$$

where $\Omega \times]-t,t[$ defines the plate domain, $\boldsymbol{\beta}$ and w represent the plate rotations and transversal displacement, respectively, $\lambda = \frac{kE}{2(1+\nu)}$, and k is a shear correction factor. The bilinear form $a\left(\boldsymbol{\beta}, \boldsymbol{\beta}\right)$ is given in Equation (6.2):

$$a\left(\boldsymbol{\beta}, \boldsymbol{\beta}\right) = \frac{E}{12(1-\nu^2)} \int_{\Omega} [\left(\frac{\partial \beta_x}{\partial x} + \nu \frac{\partial \beta_y}{\partial y}\right) \frac{\partial \beta_x}{\partial x} + \left(\nu \frac{\partial \beta_x}{\partial x} + \frac{\partial \beta_y}{\partial y}\right) \frac{\partial \beta_y}{\partial y} + \frac{1-\nu}{2} \left(\frac{\partial \beta_x}{\partial y} + \frac{\partial \beta_y}{\partial x}\right)^2] dxdy \tag{6.2}$$

As it possible to see from Equation (6.1), only the first derivatives of rotations and displacements appear in Mindlin potential energy. As a consequence, the solution of the Mindlin plate problem must belong to H^1 since rotations and displacements must be square integrable functions together with their first derivatives. In contrast, if Kirchhoff equations for thin plate bending are directly implemented imposing the kinematic constraint $\boldsymbol{\beta} = \nabla w$, then the second derivatives of the transversal displacements appear in the expression of the plate potential energy requiring that the solution belongs to H^2. As already discussed in Section (3.1.1), requiring that the solution belongs to H^2 leads to several problems in the finite element discretization.

In the present case, considering Mindlin plate theory and assuming homogeneous displacement/rotations boundary conditions, the space V of admissible solutions is defined as:

$$V = H \times W \qquad H = \left(H_0^1\left(\Omega\right)\right)^2 \qquad W = H_0^1\left(\Omega\right) \tag{6.3}$$

Every element of V will be denoted $\boldsymbol{v} = (\boldsymbol{\eta}, \zeta)$ with $\boldsymbol{\eta} = (\eta_x, \eta_y) \in H$ and $\zeta \in W$.

Setting $q\left(x, y, z\right) = \frac{t^2}{2} g\left(x, y\right)$ with $g\left(x, y\right)$ independent of t, and dividing Equation (6.1)

by t^3 the plate potential energy may be rewritten as:

$$\Pi = \frac{1}{2} a\left(\boldsymbol{\beta}, \boldsymbol{\beta}\right) + \frac{\lambda t^{-2}}{2} \int_{\Omega} (\nabla w - \boldsymbol{\beta})^2 dxdy - (g, w) \tag{6.4}$$

It is now clear from Equation (6.4) that, as the plate thickness goes to zero, the plate potential energy may become unbounded unless the constraint $\nabla w - \boldsymbol{\beta} = 0$ is enforced. In other words, in the thin limit, Mindlin theory converges to Kirchhoff plate theory and the Kirchhoff constraint has to hold. If the solution spaces for displacements and rotations are not chosen properly, then the trivial zero solution is the only case when the Kirchhoff constraint is satisfied. On the other hand if the so called inf-sup condition (Brezzi and Fortin, 1991) is satisfied, then the correct solution is recovered. In the present case, the inf-sup condition is indeed satisfied using the solution space V as proved in Brezzi et al. (1991) and Duran (1991).

In order to rewrite the Mindlin plate problem in a more convenient form, the following auxiliary variable $\boldsymbol{\gamma}$, related to the shear stress, is introduced:

$$\boldsymbol{\gamma} = \lambda t^{-2} \left(\nabla w - \boldsymbol{\beta}\right) \tag{6.5}$$

Moreover, using Helmholtz decomposition, every $\boldsymbol{\gamma}$ may be written in a unique way as:

$$\boldsymbol{\gamma} = \nabla \psi + \boldsymbol{rot} p \tag{6.6}$$

where $\psi \in H_0^1(\Omega)$, $p \in L^2(\Omega)/\mathbb{R}$ and the rotor $\boldsymbol{rot}$ of a scalar function is defined as:

$$\boldsymbol{rot}\phi = \{\frac{\partial \phi}{\partial y}, -\frac{\partial \phi}{\partial x}\} \tag{6.7}$$

The Euler Equations for Π may now be written in the form:

$$a\left(\boldsymbol{\beta}, \boldsymbol{\eta}\right) + \left(\boldsymbol{\gamma}, \nabla \zeta - \boldsymbol{\eta}\right) = (g, \zeta) \qquad \forall \left(\boldsymbol{\eta}, \zeta\right) \in V \tag{6.8}$$

Using the decomposition of $\boldsymbol{\gamma}$, Equations (6.8) and (6.5) may now be rewritten as the

sequence of three staggered problems:

$$(\nabla\psi, \nabla\xi) = (g, \xi) \qquad \forall\xi \in H_0^1(\Omega) \tag{6.9}$$

$$a(\boldsymbol{\beta}, \boldsymbol{\eta}) - (\boldsymbol{rot}(p), \boldsymbol{\eta}) = (\nabla\psi, \boldsymbol{\eta}) \qquad \forall\boldsymbol{\eta} \in \left(H_0^1(\Omega)\right)^2 \tag{6.10}$$

$$-(\boldsymbol{\beta}, \boldsymbol{rot}(q)) = \frac{t^2}{\lambda}(\boldsymbol{rot}(p), \boldsymbol{rot}(q)) \qquad \forall q \in L^2(\Omega)/\mathbb{R}$$

$$(\nabla w, \nabla\chi) = (\boldsymbol{\beta}, \nabla\chi) + \frac{t^2}{\lambda}(\nabla\psi, \nabla\chi) \qquad \forall\chi \in H_0^1(\Omega) \tag{6.11}$$

The Mindlin plate problem has therefore been rewritten as three staggered problems: Equations (6.9) and (6.11) are Poisson-type problems, and Equation (6.10) is a Stoke-like problem.

As underlined by Brezzi, the decomposition of $\boldsymbol{\gamma}$ clearly shows that it is the p component that depends on t. To better see that Equation (6.10) is a Stoke-like problem, the variable $\boldsymbol{\eta}^\perp = \{-\eta_2, \eta_1\}$ is defined and Equation (6.10) is rewritten as follows:

$$a^\perp\left(\boldsymbol{\beta}^\perp, \boldsymbol{\eta}^\perp\right) + \left(p, div(\boldsymbol{\eta}^\perp)\right) = \left(-\boldsymbol{rot}(\psi), \boldsymbol{\eta}^\perp\right) \qquad \forall\boldsymbol{\eta}^\perp \in \left(H_0^1(\Omega)\right)^2 \tag{6.12}$$

$$\left(div(\boldsymbol{\beta}^\perp), q\right) = \frac{t^2}{\lambda}(\nabla p, \nabla q) \qquad \forall q \in L^2(\Omega)/\mathbb{R} \tag{6.13}$$

where:

$$a^\perp\left(\boldsymbol{\beta}^\perp, \boldsymbol{\beta}^\perp\right) = \frac{E}{12(1-\nu^2)}\int_\Omega [\left(\frac{\partial\beta_y^\perp}{\partial x} - \nu\frac{\partial\beta_x^\perp}{\partial y}\right)\frac{\partial\beta_y^\perp}{\partial x} - \left(\nu\frac{\partial\beta_y^\perp}{\partial x} - \frac{\partial\beta_x^\perp}{\partial y}\right)\frac{\partial\beta_x^\perp}{\partial y} + \frac{1-\nu}{2}\left(\frac{\partial\beta_y^\perp}{\partial y} - \frac{\partial\beta_x^\perp}{\partial x}\right)^2] dxdy \tag{6.14}$$

As in the continuous setting, in the finite element discrete approach the space of displacement and rotations must be chosen such that they satisfy the inf-sup condition. In the thin limit, an element based on Mindlin theory will lock unless it satisfies the inf-sup condition. Since the limiting case $t \to 0$ is the most severe condition under which the inf-sup condition must be satisfied, the following analysis focuses on Equations (6.15) and

(6.16), which are obtained from Equations (6.12) and (6.13) with $t = 0$:

$$a^{\perp}\left(\boldsymbol{\beta}^{\perp}, \boldsymbol{\eta}^{\perp}\right) + \left(p, div(\boldsymbol{\eta}^{\perp})\right) = \left(-\boldsymbol{rot}(\psi), \boldsymbol{\eta}^{\perp}\right) \qquad \forall \boldsymbol{\eta}^{\perp} \in \left(H_0^1(\Omega)\right)^2 \tag{6.15}$$

$$\left(div(\boldsymbol{\beta}^{\perp}), q\right) = 0 \qquad \forall q \in L^2(\Omega)/\mathbb{R} \tag{6.16}$$

Equation (6.16) is equivalent to the Kirchhoff constraint $\nabla w - \boldsymbol{\beta} = 0$.

6.1.1.2 Discretization of the Mindlin plate problem

As discussed in the previous section, the Mindlin plate problem has been divided into three staggered problems: a Poisson problem to compute ψ (Equation 6.9), a Stoke-like problem to compute the plate rotations $\boldsymbol{\beta}$ (Equations 6.15 and 6.16) and a Poisson problem to compute the plate deflection w from the plate rotations (Equation 6.11). The first and the last Poisson problems are discretized using quadratic triangular elements and do not require any special treatment.

The Stoke-like problem represented by Equations (6.15) and (6.16) needs instead to be discretized carefully so as to satisfy the inf-sup condition in the discrete setting and guarantee optimal convergence properties to the plate finite element. Equations (6.15) and (6.16) are of the same type as the equations that govern two-dimensional problems in incompressible elasticity. Indeed, by analogy, the rotation field $\boldsymbol{\beta}^{\perp}$ in Equations (6.15) and (6.16) has the same role as the displacement field $\boldsymbol{u}$ in linear elasticity, and the Kirchhoff constraint $div(\boldsymbol{\beta}^{\perp}) = 0$ is equivalent to the incompressibility constraint $div(\boldsymbol{u}) = 0$. For these reasons, the diamond element approximation scheme introduced by Hauret et al. (2007) to satisfy the inf-sup condition in incompressible elasticity is used to solve Equations (6.15) and (6.16) in the discrete setting. The proof of the inf-sup condition for the present plate problem follows the same steps as the ones descibed in Hauret et al. (2007) and is based on the macroelement technique proposed by Stenberg (1990) and Boland and Nicolaide (1983).

Each diamond element is formed by two linear triangular elements. In the present problem, the rotations $\boldsymbol{\beta}$ are interpolated linearly on each of the triangles forming the diamond element, whereas the p component of the shear $\boldsymbol{\gamma}$ is assumed piecewise constant on each diamond element (Figure 6.1). The interpolations functions are therefore local and their

first derivatives do not need to be continuous across the element boundaries (this element belongs to the class of C^0 elements). These facts greatly simplify the element implementation and its use both in general and in fracture problems without compromising the optimal convergence properties assured by the fullfillment of the inf-sup condition.

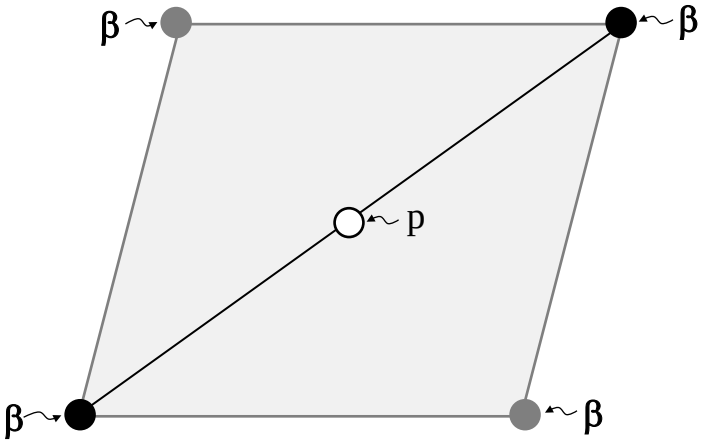

Figure 6.1: Plate diamond element (shaded grey) formed by two linear triangular elements. Rotations are linearly interpolated on each subtriangle (black primal nodes and grey dual nodes) whereas pressure is constant on each diamond element (white central node).

Every diamond mesh is based on a Delaunay triangulation of the two-dimensional plate surface resulting in a completely general method that places no requirements on the analysis domain. After the initial triangulation of the domain has been computed, the node set is enlarged by adding the set of dual nodes. A dual node is placed at the barycenter of every triangle generated by the initial triangulation. Each two-dimensional diamond element is then created based on the faces of each triangle. If the considered face is on the boundary of the domain, the diamond element is simply the triangle defined by the selected face and the dual node at the barycenter of the triangle to which the face belongs (this kind of diamond elements are called degenerate). Otherwise, if the considered face is not on the boundary of the domain, the two-dimensional diamond element is the quadrilateral based on the two nodes that define the selected face and the two dual nodes at the barycenter of the triangles that share the selected face. Figure (6.2) shows the creation of a simple diamond mesh with degenerate and regular diamond elements starting from an initial triangulation of the analysis domain.

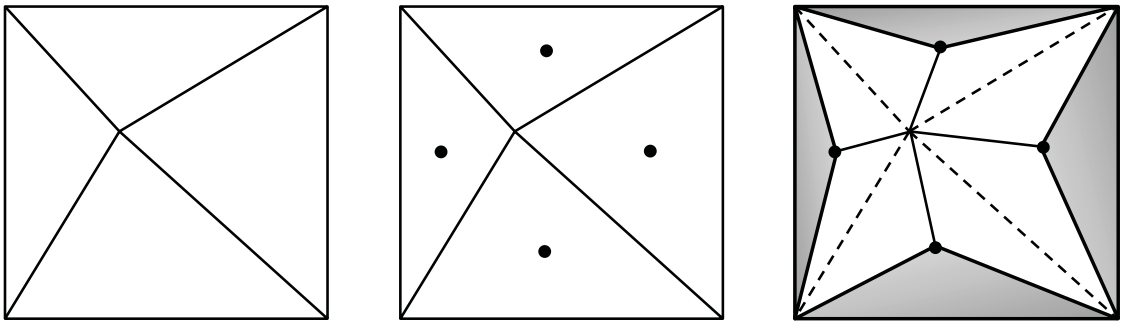

Figure 6.2: Initial triangulation of the domain (left), insertion of dual nodes at the barycenter of each triangle (center), diamond mesh generation (right). Degenerate diamond elements are shaded whereas regular diamond elements are white.

The discussion in the present section has been limited to diamond elements for plates, but the same concepts may be extended to shell problems and this approach will be pursued in future research.

6.1.1.3 C^0 plate finite element for Kirchhoff's equations of thin plate bending

Ortiz and Morris (1988) developed a plate finite element based on concepts very similar to the ones presented in the previous section. The only difference in the method of Ortiz and Morris (1988) is that they start directly from Kirchhoff's theory of thin plate bending and therefore the Kirchhoff constraint $(\nabla w - \boldsymbol{\beta}) = \mathbf{0}$ does not appear in the initial plate potential energy but is enforced through a penalty term. Therefore the potential energy to be minimized in classical Kirchhoff's plate problem is augmented by a penalty term as shown in Equation (6.17).

$$a(\boldsymbol{\beta}, \boldsymbol{\beta}) + \frac{\lambda}{2} (curl(\boldsymbol{\beta}))^2 - \text{forcing terms} \tag{6.17}$$

where λ is a penalty parameter. Imposing $curl(\boldsymbol{\beta}) = \beta_{1,2} - \beta_{2,1} = 0$ is equivalent to enforcing the Kirchhoff constraint $\nabla w - \boldsymbol{\beta} = \mathbf{0}$ since it implies that $\boldsymbol{\beta}$ may be derived from a gradient field. The diamond element approach may be applied to the Kirchhoff theory based formulation of Ortiz and Morris (1988) by enforcing the penalty term on each diamond element. This application is considered a valid preliminary test of the plate diamond approach even if the original formulation of the plate diamond element does not

require a penalty term and is valid also when the plate thickness does not go to zero. The diamond approach applied to the plate element of Ortiz and Morris (1988) was tested with different plate geometries, loading conditions and boundary conditions. Reported here is the example of a thin circular plate subjected to a uniformly distributed load and with clamped boundary conditions. The deformed plate configuration is shown in Figure (6.3), and the results of the convergence study are illustrated in Figure (6.4). Both the deformed configuration and the convergence plots show the good performance of the diamond approach applied to the plate element of Ortiz and Morris (1988) and motivate further development of the method.

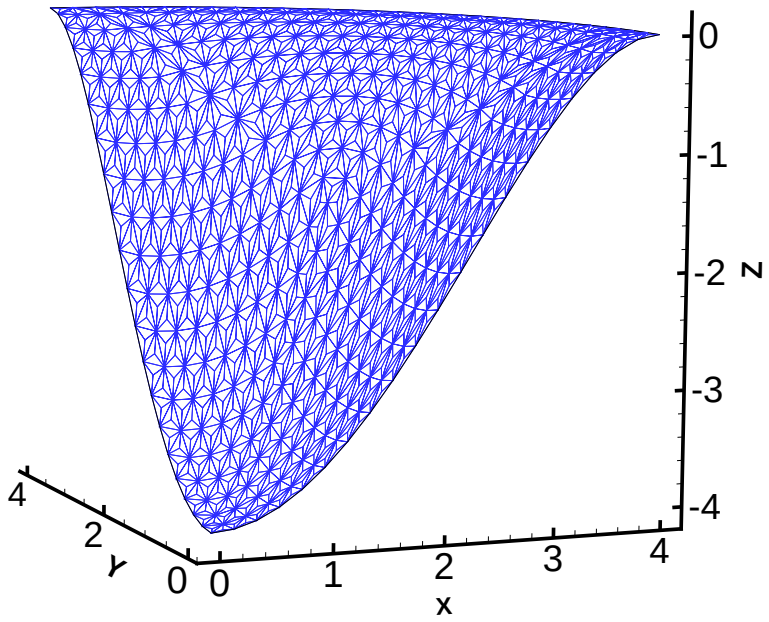

Figure 6.3: Deformed configuration of a thin clamped circular plate subjected to uniformly distributed load. The underlying diamond mesh obtained from an initial triangulation of the domain is also shown.

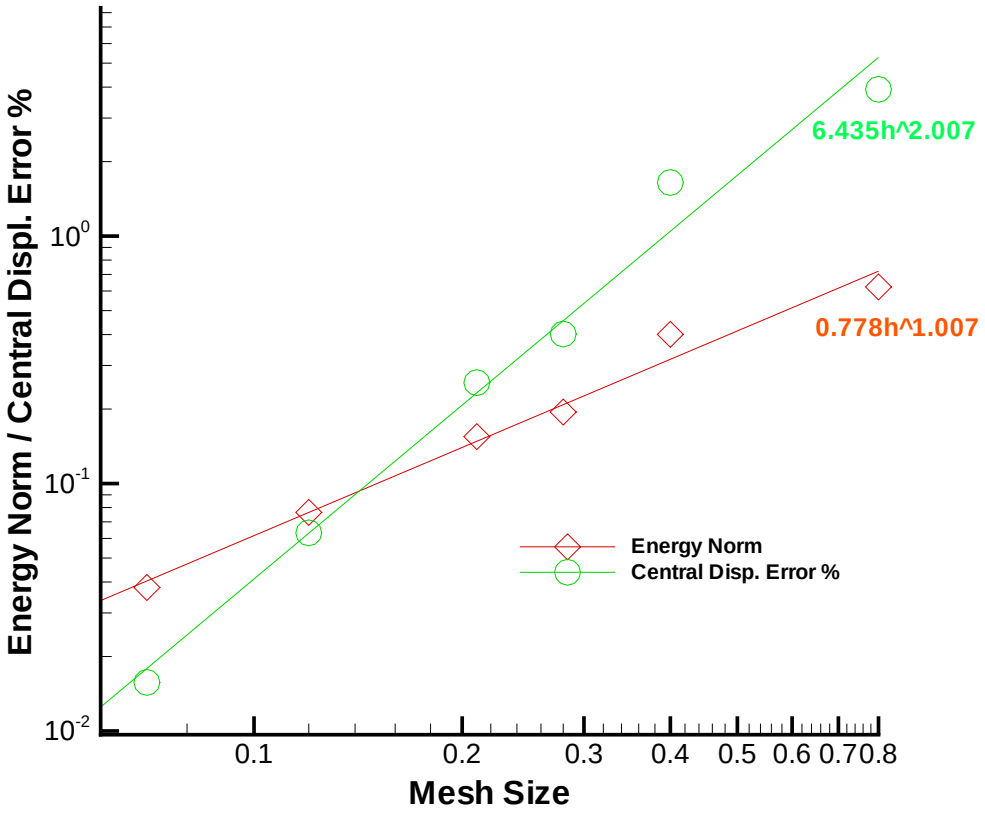

Figure 6.4: Convergence plot for the plate central displacement and the plate energy norm. The predicted theoretical rate of convergence is equal to 2 and to 1 for the plate central displacement and energy norm, respectively. Such rates of convergence have been recovered in the present test.

6.1.2 Local Max-Ent meshfree method for shells

In this approach the shell domain, including the shell thickness, is directly modeled in 3D and the equations of three-dimensional elasticity are used. As the shell thickness approaches the thin limit, the governing equations approach Kirchhoff-Love's equations for thin shells and locking would occur if the shape functions were not C^1 continuous with respect to the curvilinear coordinates θ^1 and θ^2, which span the shell middle surface. Local maximum entropy (Max-Ent) interpolation functions are C^∞ (under easily met conditions to be presented in the following section) and are used in order to prevent locking.

The local Max-Ent interpolation functions also possess a weak Kronecher delta property at the boundary, which greatly facilitates the enforcement of Dirichelet boundary conditions as opposed to other meshless methods such as the ones based on the moving least squares

method of Krysl and Belytschko (1996). Moreover local Max-Ent approximation functions are robust with respect to the parameter that controls the width of the shape function as opposed to moving least squares schemes, which are nevertheless used extensively to model shells in small and large deformation regimes (Li et al., 2008).
The local Max-Ent interpolation scheme introduced by Arroyo and Ortiz (2006) is briefly reviewed followed by its application to plate and shell problems.

6.1.2.1 Local maximum entropy approximation scheme

The local Max-Ent approximation functions belong to the general class of convex approximation schemes and possess the following characteristics: they are positive, interpolate linear functions exactly and have a weak Kronecker delta property at the boundary. Local Max-Ent shape functions are defined by two competing requirements:

- least width;
- unbiased statistical inference of the nodal data.

The shape functions of least width are the linear shape functions; only the closest nodes contribute to the value of the approximation functions in the point of interest. On the other hand, the least biased shape functions are the ones that maximize an appropriate entropy function such as the one proposed by Arroyo and Ortiz (2006):

$$H(\boldsymbol{p}) = -\sum_{a=1}^{N} p_a \log(p_a) \tag{6.18}$$

where p_a is the shape function at node a. $H(\boldsymbol{p})$ is non-negative, symmetric, continuous and strictly concave. The least biased approximation schemes are therefore the ones that, maximizing the entropy function (6.18), are solutions of the following convex optimization

problem:

$$\text{For fixed } \boldsymbol{x} \text{ maximize} \quad H(\boldsymbol{p}) \tag{6.19}$$

$$\text{subject to} \quad p_a \geq 0, \quad \text{a=1, ... , N} \tag{6.20}$$

$$\sum_{a=1}^{N} p_a = 1 \tag{6.21}$$

$$\sum_{a=1}^{N} p_a \boldsymbol{x}_a = \boldsymbol{x} \tag{6.22}$$

Conditions (6.20) and (6.21) guarantee that the shape functions may be regarded as probabilities for which an entropy function such as the one defined in Equation (6.18) is valid. Moreover, conditions (6.21) and (6.22) assure that the linear shape functions are interpolated exactly.

The convex optimization problem (6.19)−(6.22) has a solution $\boldsymbol{p}(\boldsymbol{x})$ if and only if the point $\boldsymbol{x}$ at which the shape functions p_a are evaluated belong to the convex domain $convX$ defined by the nodes $a = 1, ..., N$.

If no additional constraints are added, the support of the Max-Ent shape functions is highly non-local and extends to the entire convex hull defined by the nodes set. This motivates the introduction of the second competing requirement that characterizes the local Max-Ent interpolation scheme: locality. To define the locality of an approximation scheme, the shape function width is defined as:

$$w\left[p_a\right] = \int_{\Omega} p_a\left(\boldsymbol{x}\right) \left|\boldsymbol{x} - \boldsymbol{x}_a\right|^2 d\boldsymbol{x} \tag{6.23}$$

where Ω is the convex hull defined by the nodal set.

The most local approximation scheme may then be defined as the one that minimizes the total width of the shape functions:

$$W\left[\boldsymbol{p}\right] = \sum_{a=1}^{N} w\left[p_a\right] = \int_{\Omega} \sum_{a=1}^{N} p_a\left(\boldsymbol{x}\right) \left|\boldsymbol{x} - \boldsymbol{x}_a\right|^2 d\boldsymbol{x} \tag{6.24}$$

Since Equation (6.24) does not contain derivatives of the shape functions, its minimization may be performed pointwise as done in problem (6.25)−(6.28).

As already mentioned, unbiased statistical inference and locality are competing objectives and they are combined together by seeking a Pareto optimum, which corresponds to the solution of the following convex problem:

$$\text{For fixed } \boldsymbol{x} \text{ minimize} \quad f_\beta(\boldsymbol{x}, \boldsymbol{p}) = \beta U(\boldsymbol{x}, \boldsymbol{p}) - H(\boldsymbol{p}) \tag{6.25}$$

$$\text{subject to} \quad p_a \geq 0, \quad \text{a=1, ... , N} \tag{6.26}$$

$$\sum_{a=1}^{N} p_a = 1 \tag{6.27}$$

$$\sum_{a=1}^{N} p_a \boldsymbol{x}_a = \boldsymbol{x} \tag{6.28}$$

where $U(\boldsymbol{x}, \boldsymbol{p}) = \sum_{a=1}^{N} p_a(\boldsymbol{x}) |\boldsymbol{x} - \boldsymbol{x}_a|^2$ and the parameter $\beta \in (0, \infty)$ sets the relative contributions of locality and unbiased inference in determining the approximation scheme. The convex optimization problem (6.25)−(6.28) has a solution $\boldsymbol{p}_\beta(\boldsymbol{x})$ if and only if the point $\boldsymbol{x}$ at which the shape functions p_a are evaluated belong to the convex domain defined by the nodes a=1, ... , N. The convex approximation scheme defined by $\boldsymbol{p}_\beta(\boldsymbol{x})$ is called the local Max-Ent approximation scheme.

Figure (6.5) shows $\boldsymbol{p}_\beta(\boldsymbol{x})$ evaluated at the center of a simple square convex domain: the locality of the approximation scheme increases as the value of the parameter β increases, clearly showing the role of β in balancing locality and unbiased statistical inference. Arroyo and Ortiz (2006) used the dual formulation of the minimization problem (6.25)−(6.28) for the analysis of the local Max-Ent approximation scheme and to provide a practical way to compute the local Max-Ent shape functions and their spatial derivatives. In this context, few results are reported in view of the application of the Max-Ent approximation scheme to plates and shells. At first it is important to note that a local Max-Ent shape function related to a node a in the convex domain decays exponentially with the distance from node a. Moreover, the rate of the exponential decay depends on the parameter β, which, as discussed above, sets the locality of the approximation scheme.

A key motivation for the application of local Max-Ent approximation scheme to plate and shell problems regards the smoothness of $\boldsymbol{p}_\beta(\boldsymbol{x})$ with respect to $\boldsymbol{x}$. If $\beta : convX \to [0, \infty) \in C^r$ in int(convX) then the local Max-Ent shape functions are of class C^r in

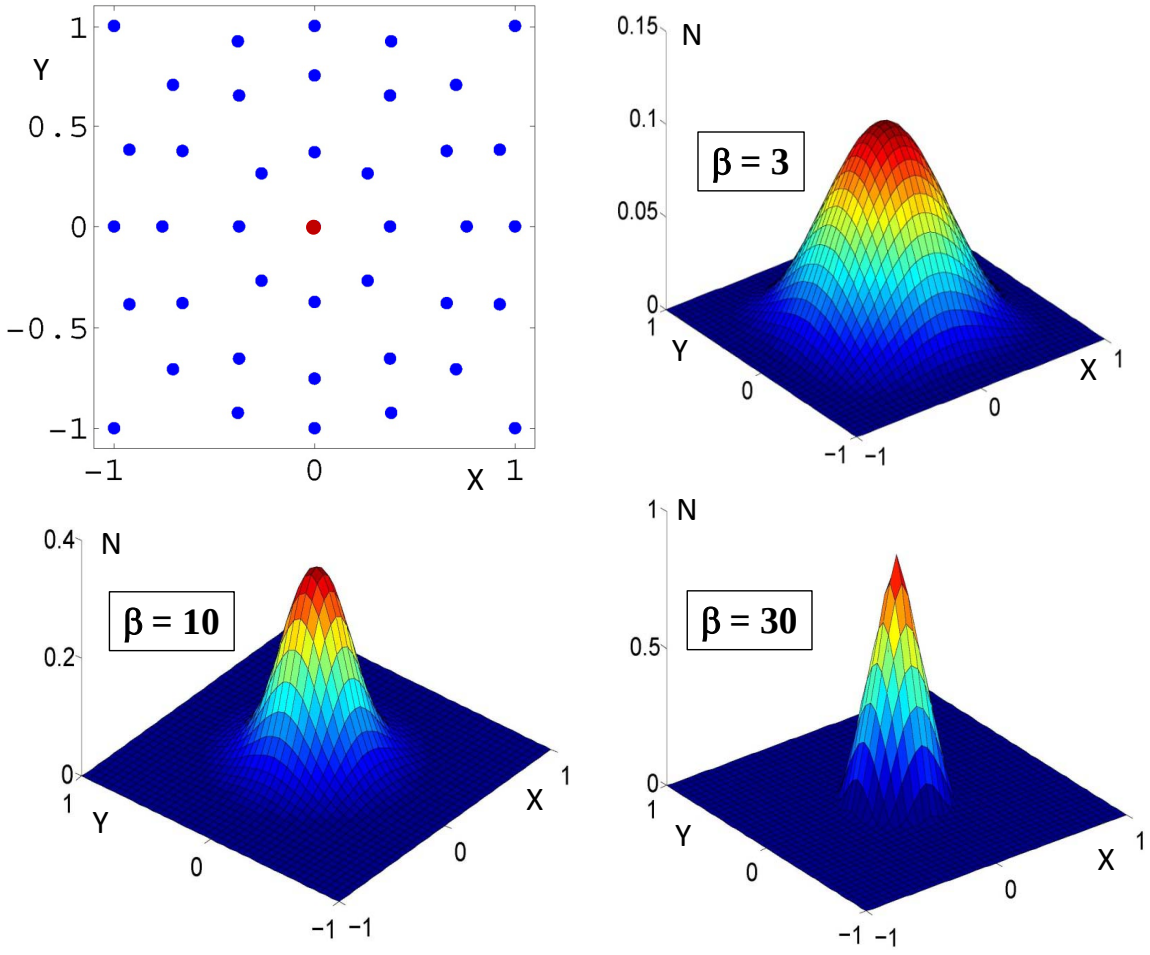

Figure 6.5: Max-Ent local shape functions for a square convex domain shown in the left upper corner. The shape function relative to the node at the center of the convex domain (red point) is represented for different values of the parameter β.

int(convX). Therefore the local Max-Ent shape functions may be easily constructed so that they are C^1 over all the domain and may be employed to describe the deformation of shell-like bodies.

Local Max-Ent shape functions are also continuously differentiable with respect to the parameter β. If the solution of the considered problem corresponds to the minimum of a given functional, then β may vary inside the analysis domain and may be selected so that it minimizes the governing functional. In other words, the given functional may be minimized with respect to both β and the problem unknowns. This minimization problem is largely facilitated by the fact that local Max-Ent shape functions are differentiable with respect to β and that such derivatives may be computed explicitly.

Although the local Max-Ent interpolation scheme has been constructed for convex do-

mains, non-convex domains may be considered as well. Indeed, it is sufficient to decompose them into convex subdomains that may be glued together in a fully conforming way by taking advantage of the weak Kronecher delta property of the local Max-Ent approximation scheme.

Finally it is important to underline that no meshing of the domain is needed to construct the local Max-Ent interpolation scheme, which therefore is a meshfree method.

6.1.2.2 Local maximum entropy approximation scheme for plates

As previously mentioned, the three-dimensional plate domain is directly considered and the governing equations for three-dimensional elasticity are employed without introducing any kinematic assumptions. The plate domain is discretized by inserting a set of nodes on the boundary of the domain as well as in its interior. These nodes carry information about the plate displacements that are the only unknowns of the problem. In order to interpolate the displacement field over the entire plate starting from the nodal displacements, the Max-Ent approximation scheme is used on the plate surface together with linear or quadratic polynomial shape functions across the plate thickness. More precisely the plate displacement field $\boldsymbol{u}(\boldsymbol{X})$ is given by:

$$\boldsymbol{u}(\boldsymbol{X}) = \sum_{i}^{p} \boldsymbol{u}_i N_i(\boldsymbol{X}) \tag{6.29}$$

where p is the total number of nodes in the plate domain, $\boldsymbol{u}_i$ is the displacement of node i in the plate domain and $N_i(\boldsymbol{X})$ are the nodal shape functions reported in Equation (6.30).

$$N_i(X,Y,Z) = M_i(X,Y)\, P_i(Z) \tag{6.30}$$

$M_i(X,Y)$ is the local Max-Ent shape function for node i, $P_i(Z)$ is a polynomial shape function dependent on Z only, and it has been assumed that the Z axis is perpendicular to the plate middle surface. Therefore, each nodal shape function is given by the product of two shape functions: $M_i(X,Y)$, which only depends on the surface coordinates (X,Y) and $P_i(Z)$, which only depends on Z (Figure 6.6). It is important to note that the nodal shape function $N_i(X,Y,Z)$ is defined in the plate reference domain directly and there are no standard domains in contrast with classical finite elements.

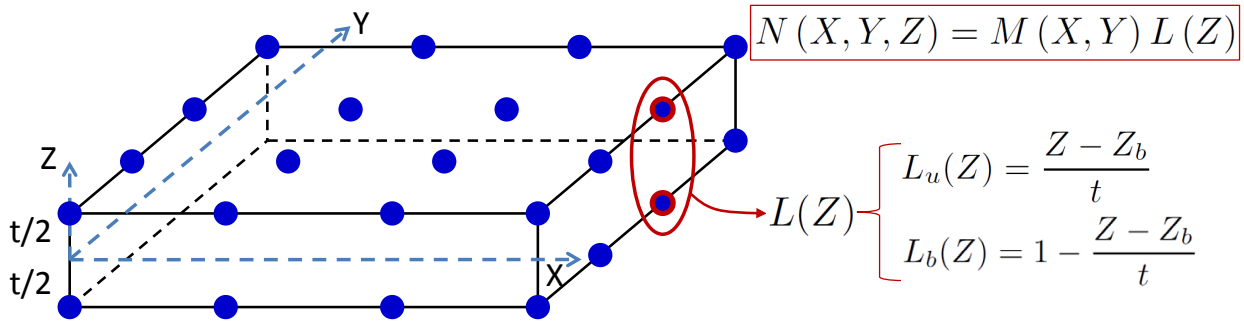

Figure 6.6: Example of 3D plate domain discretization using the Max-Ent approximation scheme. An example of nodal shape functions with linear interpolation L across the thickness is also shown. Across the thickness the plate domain is defined by $-\frac{t}{2} \leq Z \leq \frac{t}{2}$ and u stands for upper node while b refers to a bottom node.

Another fundamental aspect of this approximation scheme is that the weak Kronecker delta property is valid only at the boundary of the domain (where, as previously mentioned, greatly facilitates the application of essential boundary conditions). Inside the domain, particular care needs to be exerted to apply nodal forces and to compute displacement at a given location. Indeed the displacement at the location of node a is not equal to $\boldsymbol{u}_a$ since $N_i(\boldsymbol{X}_a) \neq \delta_{ai}$. Instead the displacement at node a must be computed as $\sum_i^p \boldsymbol{u}_i N_i(\boldsymbol{X}_a)$. Analogously, to apply a local force $\boldsymbol{F}$ at the location of node a, a force $\boldsymbol{F}_i$ equal to $\boldsymbol{F} N_i(\boldsymbol{X}_a)$ is applied to all the nodes i in the domain so that $\boldsymbol{F}(\boldsymbol{X}_a) = \sum_i^p \boldsymbol{F} N_i(\boldsymbol{X}_a)$. Since the local Max-Ent shape function M_i decays exponentially with distance from node i, the nodes involved in the application of the local force $\boldsymbol{F}$ are only the ones close to node a (the extension of the domain of influence depends on the parameter β).

The exponential decay of local Max-Ent shape functions may also be exploited to reduce the number of nodes needed to compute the shape function at a given location. In other words, the problem (6.25)−(6.28) may be solved not considering all the nodes in the analysis convex domain but only those inside a circle of radius R from the location at which the shape function needs to be evaluated. Reducing the number of nodes implies that the minimization problem (6.25)−(6.28) may be solved faster and that the resulting stiffness matrix of the plate problem will be banded.

This approximation scheme for plates has been tested in a simple example regarding

a clamped square plate subjected to a concentrated load applied at its center. The plate thickness is 0.01 and the length of the plate side is 4. The high side length to thickness ratio equal to 400 implies that the plate deformation is well described by Kirchhoff theory. However, locking does not occur because the proposed shape functions based on the local Max-ent approximation scheme are continuously differentiable with respect to the plate surface coordinates. In the presented test the value of the parameter β is chosen so as to minimize the plate problem potential energy, but it is kept constant throughout the analysis domain. Moreover, a quadratic interpolation across the thickness was chosen to avoid membrane locking (Hauptmann and Schweizerhof, 1998, Li et al., 2005) since no plane stress condition is enforced. Figure (6.7) shows the plate deformed shape whereas Figure (6.8) shows the convergence of the energy error with respect to node distance.

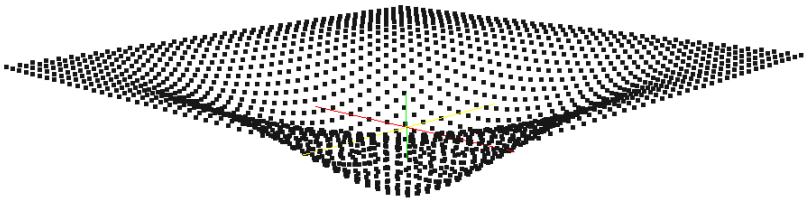

Figure 6.7: Deformed configuration of a clamped square plate subjected to a centered concentrated load. The nodes used to describe the analysis domain are shown.

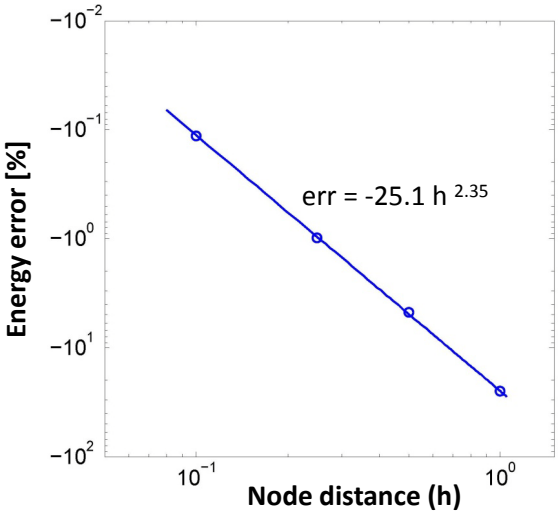

Figure 6.8: Convergence of energy error versus node distance relative to the presented plate example.

It is important to notice that using the present approximation scheme, thin plate domains and general three-dimensional solid domains may be joined in a seamless way, with no need for transitional elements or any other special treatment.

There is a potential modification that may speed up the calculation of local Max-Ent shape functions by more than 30 times (the gain in computational speed increases advantageously with the number of nodes in the domain). In the case of rectangular domains the interpolation functions $N(\boldsymbol{X})$ may be computed from the product of three one-dimensional shape functions. Using the previous convention, $N(\boldsymbol{X})$ may be written as $N(\boldsymbol{X}) = M(X)M(Y)P(Z)$ where $M(X)$ and $M(Y)$ are one-dimensional Max-Ent shape functions and $P(Z)$ is, as before, a polynomial shape function in the direction perpendicular to the plate middle surface. The calculation of 1D versus 2D local Max-Ent shape functions greatly decreases the computational time to calculate $N(\boldsymbol{X})$. Moreover, taking advantage of the local Max-Ent weak Kronecker delta property, rectangular subdomains may be glued together with other shape domains to form larger plate-like bodies.

The extension of the presented method to shell-like structures is under investigation, and here only a few preliminary results are reported to show the very promising performance of this scheme. In order to represent the shell deformation as a function of nodal displacements, the Max-Ent interpolation scheme is, as before, combined with a polynomial shape function in the thickness direction. The most important challenge to apply the same scheme developed for flat plate-like bodies to shells is the fact that Max-Ent shape functions are only defined for convex domains and shell domains are not convex with respect to a 3D coordinate system. To overcome this challenge, Max-Ent shape functions are first defined in a flat reference domain and successively are mapped to the shell domain using an isoparametric map.

A second intrinsic challenge in the study of shell-like bodies is related to the correct representation of the curved analysis domain (Krysl and Belytschko, 1996). For instance, the use of flat finite elements introduces an unavoidable error in the approximation of curved analysis domain. Max-Ent shape functions seem better able to approximate curved analysis domains as shown in a first example reported in Figure (6.9). This example compares the ability of the Max-Ent approximation scheme with that of quadrilateral finite elements

in approximating a quarter of a hemisphere. The pointwise error computed at the finite element quadrature points shows the better performance (by an order of magnitude) of the Max-Ent approximation scheme.

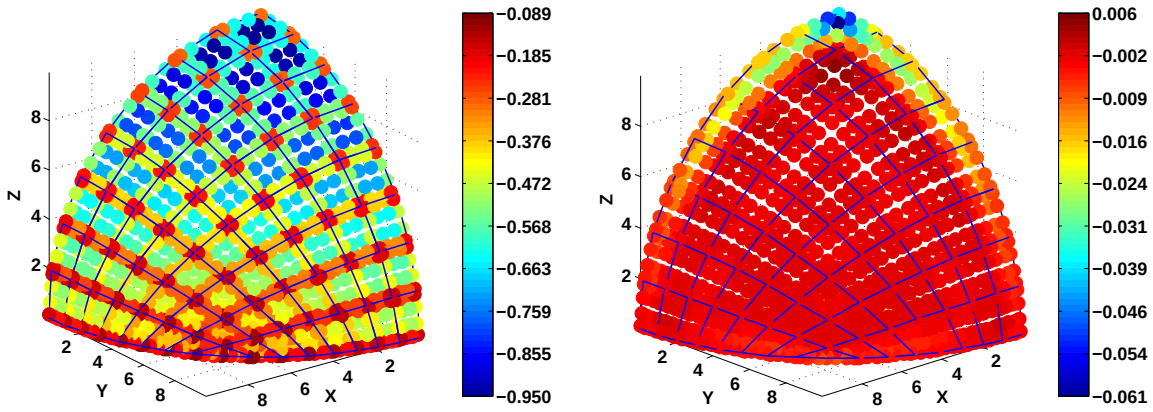

(a) Color map of the approximation error (%) due to the discretization of a quarter of a hemisphere using quadrilateral finite element.

(b) Color map of the approximation error (%) due to the approximation of a quarter of a hemisphere using the Max-Ent scheme.

Figure 6.9: The approximation error err is computed at the finite element quadrature points as: $err = \frac{(R_{app} - R_{hem}) \cdot 100}{R_{hem}}$ where R_{hem} is the radius of the hemisphere and R_{app} is the radius computed from the approximation scheme.

As a second preliminary result, the application of the Max-Ent approximation scheme for shells to the pinched hemisphere problem proposed in the obstacle course of Belytschko et al. (1985) is chosen. Figure (6.10(a)) shows the example setup while Figure (6.10(b)) shows the energy convergence plot obtained using the Max-Ent approximation scheme for shells.

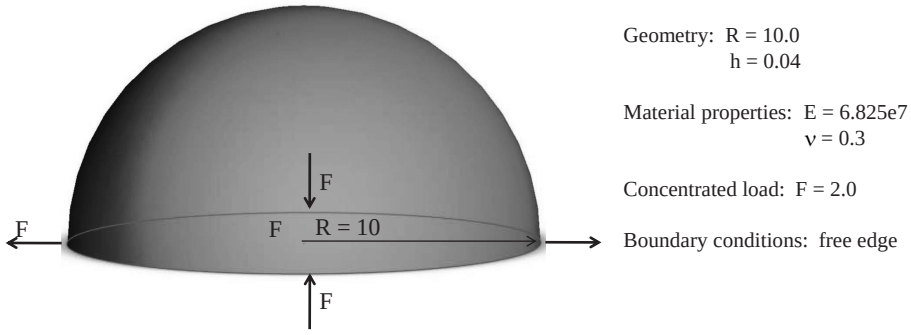

(a) Geometry and loading conditions in the pinched hemisphere example.

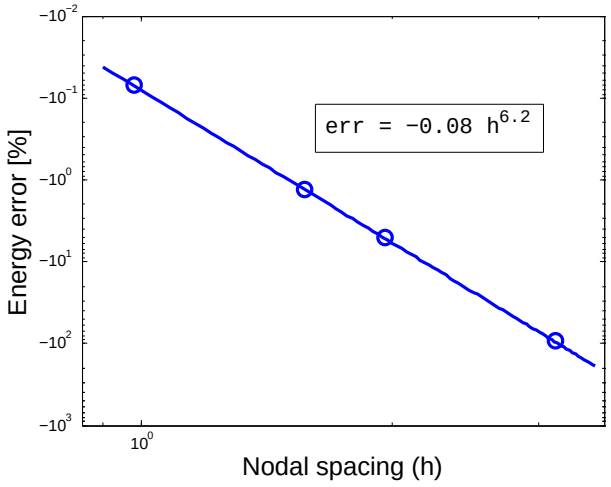

(b) Energy error $= \frac{(E_{computed} - E_{exact}) \cdot 100}{E_{exact}}$ versus nodal spacing. The high rate of convergence equal to 6.2 is noteworthy.

6.2 Improving damage characterization and kinematic description of sandwich shells

The present computational scheme has been used to analyze large sandwich structures and to capture the response of full size hull sections and navy vessels. In order to achieve this goal and contain the overall computational cost, shell finite elements based on Kirchhoff-Love's theory have been used. This model may describe the global behavior of large shell sandwich structures subjected to underwater explosions, but it needs to be improved in order to better characterize the damage occurring in the sandwich core and between the core and the external face sheets.

One possibility would be to use three layers of 3D shell finite elements across the sandwich thickness to model separately the sandwich core and face sheets. In this case, the displacement field across the shell thickness would be better described since it may include a "zig-zag" term and higher order terms if multiple nodes are placed across the thickness of each 3D shell element. Moreover, the crushing of the core may be better captured since the 3D shell finite element used to model the core may independently change its thickness. Delamination between the sandwich core and the external fiber composite layers is another failure mechanism that cohesive elements inserted between the layers of shell finite elements across the sandwich thickness may be able to capture. The cohesive law presented in Section (2.3) may be calibrated to represent the material properties of the interface between the sandwich core and the face sheets. Using shell finite elements with local shape functions such as the ones discussed in Section (6.1.1) would greatly reduce the computational cost since cohesive elements would be introduced only when the local cohesive stress of the material is reached.

The use of 3D shell finite elements would also facilitate the transition to full three-dimensional elements and therefore the modeling of three-dimensional joints between the sandwich shell and the rest of the structure or between two adjacent panels. Joints may be critical in understanding the failure of the overall sandwich structure and they may need to be carefully modeled.

An additional aspect that may lead to future research is the improvement of the model for fiber composite materials in finite kinematics. Possible modifications of the model are to account for matrix-fiber debounding and for fiber-fiber sliding and interaction. These aspects are particularly important to take into account the material texture and better predict the failure mechanisms of fiber composites.

6.3 Uncertainty quantification

The performance of fiber composite sandwich structures may be affected by material imperfections or by damages deriving from exceptional or cycling loading during the structure service. Defects and damages may reduce the maximum load that the structure is able to sustain, as well as its life cycle. As mentioned in Section (1.1), one of the

reasons for which sandwich material configurations are not widely employed in structural engineering is the lack of knowledge of how reliable sandwich shells are, especially if defects or damages are present.

In this regard the developed computational scheme may be combined with uncertainty quantification techniques (Lucas et al., 2008, Leyendecker et al., 2010) to assess the failure probability of sandwich structures subjected to underwater explosions. The material defects in the sandwich core and in the face sheets and the damage due, for instance, to a previous explosion may be characterized probabilistically and their effect on the structure loading capability may be assessed.

Chapter 7

Concluding remarks

An existing computational scheme for the study of shell structures has been further developed to study the behavior of shell fiber composite sandwich structures subjected to underwater explosions. The computational scheme has been verified, validated and used in representative test scenarios.

This scheme includes material models for the sandwich core and fiber reinforced face sheets that have been validated and calibrated. A cohesive material law is used to describe the fracture process if this occurs. The structural sandwich shells are described using non-local shell finite elements with optimal convergence properties and which have been developed and tested in both linearized and finite kinematics. Moreover, cohesive elements are included in the finite element code and enable the study of fracture propagation and fragmentation due to an explosive load.

The finite element code has been further verified to test its convergence and fracture propagation in fiber composite materials. Water-hammer experiments are used to validate the shell solver coupled with a fluid solver inside the VTF (Virtual Test Facility) code. Two different methods for applying the pressure load due to an underwater explosion are considered: the use of an applied pressure profile or that of a fluid-solid coupled simulation in which the charge is represented by an energy deposition. These two methods have been briefly compared, and an applied pressure profile has been chosen to perform preliminary analyses while a full fluid-solid coupled simulation is used in the final analyses. An applied pressure profile has been used in the analyses to assess the role of fiber volume fraction and fiber orientation in the external face sheets. The effect of these design parameters has been investigated through a parametric study. Moreover, sandwich panels

with fiber composite or aluminum external layers are compared based on their capability to resist explosive loading. Among the designs considered, the best sandwich configuration is composed of fiber composite face sheets with two orthogonal families of fibers and a fiber volume fraction equal to 0.7. Finally a hull section of an Argentinean navy vessel is considered, and the optimized sandwich design is used as the hull cross section. The hull section is subjected to an underwater explosion modeled in a fluid-solid coupled simulation and the effect of charge mass and charge distance from the hull is investigated. The flexibility of the presented method is noteworthy; it can be applied to any geometry and can model various sandwich material layouts. This research shows how the role of different design parameters in resisting underwater explosions may be analyzed and optimized. The analysis process started from the materials' calibration followed by a preliminary optimization of certain design parameters and the final analysis of the structure of interest.

Future improvements, including two new shell finite elements, are finally discussed together with the possibility to combine the proposed computational scheme with uncertainty quantification techniques.

Bibliography

M. Arroyo and M. Ortiz. Local maximum-entropy approximation schemes: a seamless bridge between finite elements and meshfree methods. *International Journal for Numerical Methods in Engineering*, 65:2167–2202, 2006. 93, 102, 104

ASC. Virtual Test Facility, the software distribution site of the Caltech ASC Center for Simulation of Dynamic Response of Materials. `http://www.cacr.caltech.edu/asc/wiki/bin/view/`. 39

J.Z. Ashani and A.K. Ghamsari. Theoretical and experimental analysis of plastic response of isotropic circular plates subjected to underwater explosion loading. *Mat.-wiss. u. Werkstofftech*, 39(2):171–175, 2008. 62

S. Avachat and M. Zhou. Dynamic response of submerged composite sandwich structure to impulsive loading. In G. Ravichandran, editor, *Proceedings of the 9th International Conference on Sandwich Structures (ICSS9)*, June 2010. 6

R.C. Batra and N.M. Hasssan. Response of fiber reinforced composites to underwater explosive loads. *Composites: Part B*, 38:448–468, 2007. xvii, 6, 35, 36

R.C. Batra and N.M. Hasssan. Blast resistance of unidirectional fiber reinforced composites. *Composites: Part B*, 39:513–536, 2008. 6, 35

M. Battley. Failure Mechanisms of Sandwich Structures. Presentation in the Advanced Sandwich Structures School during ICSS9, 2010. 2

T. Belytschko, H. Stolarski, W.K. Liu, N. Carpenter, and J.S.J. Ong. Stress projection for membrane and shear locking in shell finite-elements. *Computer Methods in Applied Mechanics and Engineering*, 51:221–258, 1985. 110

J.M. Boland and R.A. Nicolaide. Stability of Finite Elements Under Divergence Constraints. *SIAM Journal on Numerical Analysis*, 20(4):722–731, 1983. 97

F. Brezzi and M. Fortin. *Mixed and Hybrid Finite Element Methods*. Springer-Verlag, 1991. 22, 93, 95

F. Brezzi, M. Fortin, and R. Stenberg. Error analysis of mixed-interpolated elements for Reissner-Mindlin plates. *Mathematical Models and Methods in Applied Sciences*, 1(2): 125–151, 1991. 95

G.T. Camacho and M. Ortiz. Computational modeling of impact damage in brittle materials. *International Journal of Solids and Structures*, 33:2899–2938, 1996. 18

L.A. Carlsson. Sandwich Plate and Beam Theory. Buckling Analysis of Sandwich Panels. Presentation in the Advanced Sandwich Structures School during ICSS9, 2010. xi, 2

A. Cavicchi and R. Massab. Damage interaction in fully backed sandwich beams subject to time dependent moving loads. In G. Ravichandran, editor, *Proceedings of the 9th International Conference on Sandwich Structures (ICSS9)*, June 2010. 6

F. Cirak and M. Ortiz. Fully C1-conforming subdivision elements for finite deformation thin-shell analysis. *International Journal for Numerical Methods in Engineering*, 51: 813–833, 2001. 23, 30, 41

F. Cirak, M. Ortiz, and P. Schröder. Subdivision surfaces: a new paradigm for thin-shell finite-element analysis. *International Journal for Numerical Methods in Engineering*, 47:2039–2072, 2000. xii, 22, 23, 24, 25, 30

F. Cirak, M. Ortiz, and A. Pandolfi. A cohesive approach to thin-shell fracture and fragmentation. *Computer Methods in Applied Mechanics and Engineering*, 194:2604–2618, 2005. xii, 23, 30, 32, 34, 79

R.H. Cole. *Underwater explosions*. Princeton University Press, 1948. xvii, 36

D.A. Crump, J.M. Dulieu-Barton, and J. Savage. The manufacturing procedure for aerospace secondary sandwich structure panels. *Journal of Sandwich Structures and Materials*, in press. 3

J.P. Dear, H. Arora, and P. Hooper. Blast and other high rate loading of composite sandwich structures. In G. Ravichandran, editor, *Proceedings of the 9th International Conference on Sandwich Structures (ICSS9)*, June 2010. 6

R. Deiterding, R. Radovitzki, S.P. Mauch, F. Cirak, D.J. Hill, C. Pantano, J.C. Cummings, and D.I. Meiron. Virtual Test Facility: a virtual shock physics facility for simulating the dynamic response of materials. Technical report, 2006. URL `http://www.cacr.caltech.edu/asc`. 37, 38

R. Deiterding, F. Cirak, and S.P. Mauch. Efficient Fluid-Structure Interaction Simulation of Viscoplastic and Fracturing Thin-Shells Subjected to Underwater Shock Loading. *Fluid-Structure Interaction. Theory, Numerics and Applications*, 29(9):65–80, 2008. xiii, 37, 38, 41, 45, 63, 64

V.S. Deshpande and N.A. Fleck. Multi-axial yield behaviour of polymer foams. *Acta materialia*, 49:1859–1866, 2001. xi, 10, 11

V.S. Deshpande and N.A. Fleck. The Resistance of Clamped Sandwich Beams to Shock Loading. *Journal of Applied Mechanics*, 71:386–401, 2004. xvii, 6, 35, 36

R. Duran. The inf-sup condition and error estimates for the Arnold-Falk plate bending element. *Numerische Mathematik*, 59:769–778, 1991. 95

T. ElSayed. *Constitutive models for polymers and soft biological tissues*. PhD thesis, California Institute of Technology, 2008. 14, 68, 84

T. ElSayed, A. Mota, F. Fraternali, and M. Ortiz. A variational constitutive model for soft biological tissues. *Journal of Biomechanics*, 41:1458–1466, 2008a. 11, 12, 13

T. ElSayed, A. Mota, F. Fraternali, and M. Ortiz. Biomechanics of traumatic brain injury. *Computer Methods in Applied Mechanics and Engineering*, 197:4692–4701, 2008b. 11, 12

T. ElSayed, W. Mock Jr, A. Mota, F. Fraternali, and M. Ortiz. Computational assessment of ballistic impact on a high strength structural steel/polyurea composite plate. *Computational Mechanics*, 43:525–534, 2009. xii, 11, 12

H.D. Espinosa, D. Grégoire, F. Latourte, and R.S. Bellur-Ramaswamy. Failure modes in solid and sandwich composite panels subjected to underwater impulsive loads. In G. Ravichandran, editor, *Proceedings of the 9th International Conference on Sandwich Structures (ICSS9)*, June 2010. 6

E.E. Gdoutos. Failure Mechanisms of Sandwich Structures. Presentation in the Advanced Sandwich Structures School during ICSS9, 2010. 3

S.C. Han, A. Tabiei, and W.T. Park. Geometrically nonlinear analysis of laminated composite thin shells using a modified first-order shear deformable element-based lagrangian shell element. *Composite Structures*, 82:465474, 2008. 21

R. Hauptmann and K. Schweizerhof. A systematic development of ''solid-shell'' element formulations for linear and non-linear analyses employing only displacement degrees of freedom. *International Journal for Numerical Methods in Engineering*, 42:49–69, 1998. 108

P. Hauret, E. Kuhl, and M. Ortiz. Diamond elements: a finite-element/discrete-mechanics approximation scheme with guaranteed optimal convergence in incompressible elasticity. *International Journal for Numerical Methods in Engineering*, 72:253–294, 2007. 93, 97

B. Hayman. Non-destructive examination and quality assurance. Presentation in the Advanced Sandwich Structures School during ICSS9, 2010. 5

T.J.R. Hughes. *The Finite Element Method: Linear Static and Dynamic Finite Element Analysis*. Dover, 2000. 29

K. Inaba and J.E. Shepherd. Fluid-structure interaction in liquid-filled composite tubes under impulsive loading. Number 413, Hyatt Regency Albuquerque, Albuquerque, New Mexico, USA, 2009a. xiii, 41, 45, 46, 47, 57, 68

K. Inaba and J.E. Shepherd. Failure of liquid-filled filament-wound composite tubes subjected to axial impact. Edinburgh International Convention Center (EICC), Edinburgh, UK, 2009b. 58, 60

I. Ivanez, B.L. Buitrago, S.K. Garcia-Castillo, C. Santiuste, S. Sanchez-Saez, and E. Barbero. Behaviour of sandwich structures with foam core subjected to high-velocity impact. In G. Ravichandran, editor, *Proceedings of the 9th International Conference on Sandwich Structures (ICSS9)*, June 2010. 6

Y.S. Jeung and I.Y. Shen. Development of isoparametric, degenerate constrained layer element for plate and shell structures. *AIAA Journal*, 39(10):1997–2005, 2001. 21

S. Kazemahvazi, J. Kiele, B. Russell, V. Deshpande, and D. Zenkert. Impact properties of corrugated composite sandwich cores. In G. Ravichandran, editor, *Proceedings of the 9th International Conference on Sandwich Structures (ICSS9)*, June 2010. 5

M. Klaus and H.G. Reimerdes. Influence of delaminations in sandwich skins on residual strength after impact simulations. In G. Ravichandran, editor, *Proceedings of the 9th International Conference on Sandwich Structures (ICSS9)*, June 2010. 6

P. Krysl and T. Belytschko. Analysis of thin shells by the element-free Galerkin method. *International Journal of Solids and Structures*, 33(20-22):3057–3080, 1996. 93, 102, 109

S. Leyendecker, L.J. Lucas, H. Owhadi, and M. Ortiz. Optimal Control Strategies for Robust Certification. *Journal of Computational and Nonlinear Dynamics*, 5:031008–1–10, 2010. 113

D. Li, Z.Q. Lin, and S.H. Li. Numerical analysis of Mindlin shell by meshless local Petrov-Galerkin method. *Acta Mechanica Solida Sinica*, 21(2):160–169, 2008. 102

Q. Li, J. Soric, T. Jarak, and S.N. Atluri. A locking-free meshless local petrov-galerkin formulation for thick and thin plates. *Journal of Computational Physics*, 208:116–133, 2005. 108

R. Li, G.A. Kardomateas, and G.J. Simitses. Nonlinear Response of a Shallow Sandwich Shell with Compressible Core to Blast Loading. *Journal of Applied Mechanics*, 75: 61023, 2000a. 21

S. Li, W. Hao, and W.K. Liu. Numerical simulations of large deformation of thin shell structures using meshfree methods. *Journal of Computational Mechanics*, 25:102–116, 2000b. 93

L. Librescu, S.Y. Oh, and J. Hohe. Dynamic response of anisotropic sandwich flat panels to underwater and in-air explosions. *International Journal of Solids and Structures*, 43: 3794–3816, 2006. 6

L. Librescu, S.Y. Oh, and J. Hohe. Implication of Nonclassical Effects on Dynamic Response of Sandwich Structures Exposed to Underwater and In-Air Explosions. *Journal of Ship Research*, 51(2):83–93, 2007. 6

J. Lighthill. *Waves in Fluids*. Cambridge University Press, 1978. 48

J. Lubliner. *Plasticity theory*. Dover, 2008. 64

L.J. Lucas, H. Owhadi, and M. Ortiz. Rigorous verification, validation, uncertainty quantification and certification through concentration-of-measure inequalities. *Computer Methods in Applied Mechanics and Engineering*, 197:4591–4609, 2008. 113

Millikarjuna and T. Kant. A general fiber-reinforced composite shell element based on a refined shear deformation-theory. *Computers and Structures*, 42(3):381–388, 1992. 22

R.A.W. Mines and A. Alias. Numerical simulation of the progressive collapse of polymer composite sandwich beams under static loading. *Composite: Part A*, 33:11–26, 2002. 10

R.A.S. Moreira, R.J. Alves de Sousa, and R.A.F. Valente. A solid-shell layerwise finite element for non-linear geometric and material analysis. *Composite Structures*, 92: 15171523, 2010. 21

A.P. Mouritz. The damage to stitched GRP laminates by underwater explosion shock loading. *Journal of Composite Science and Technology*, 55:365–374, 1995. 5

H. Noguchi, T. Kawashima, and T. Miyamura. Element free analyses of shell and spatial structures. *International Journal for Numerical Methods in Engineering*, 47:1215–1240, 2000. 93

R.W. Ogden. *Non-linear Elastic Deformations*. Ellis Horwood, Chichester, UK, 1984. 11

M. Ortiz and G.R. Morris. C^0 Finite Element Discretization of Kirchhoffs's Equations of thin Plate Bending. *International Journal for Numerical Methods in Engineering*, 26: 1551–1566, 1988. 93, 99, 100

M. Ortiz and A. Pandolfi. A class of cohesive elements for the simulation of three-dimensional crack propagation. *International Journal for Numerical Methods in Engineering*, 44:1267–1282, 1999. xii, 18, 19, 20, 31

A. Pandolfi and G.A. Holzapfel. Three-Dimensional Modeling and Computational Analysis of the Human Cornea Considering Distributed Collagen Fibril Orientations. *Journal of Biomechanical Engineering*, 130:061006, 2008. 15

A. Pandolfi and F. Manganiello. A Model for the Human Cornea. Constitutive Behavior and Numerical Analysis. *Biomechanics and Modeling in Mechanobiology*, 5:237–246, 2006. 15

M.R. Patel and I. Finnie. Structural Features and Mechanical Properties of Rigid Cellular Plastics. *Journal of Materials*, 5(4):909–932, 1970. xi, 10

R. Stenberg. A Technique for Analysing Finite Element Methods for Viscous Incompressible Flow. *International Journal for Numerical Methods in Fluids*, 11:935–948, 1990. 97

M. Sulmoni, T. Gmür, J. Cugnoni, and M. Matter. Modal validation of sandwich shell finite elements based on a p-order shear deformation theory including zigzag terms. *International Journal for Numerical Methods in Engineering*, 75:13011319, 2008. 22

M.M. Swisdak. Explosion Effects and Properties-Part ii: Explosion Effects in Water. Technical report, Naval Surface Weapons Center, Dahlgren, VA, 1978. xvii, 36

A. Tabiei and R. Tanov. Sandwich shell finite element for dynamic explicit analysis. *International Journal for Numerical Methods in Engineering*, 54:763787, 2002. 22

X.G. Tan and L. Vu-Quoc. Efficient and accurate multilayer solid-shell element: non-linear materials at finite strain. *International Journal for Numerical Methods in Engineering*, 63:21242170, 2005. 21

S.A. Tekalur, K. Shivakumar, and A. Shukla. Mechanical behavior and damage evolution in E-glass vinyl ester and carbon composites subjected to static and blast loads. *Composites: Part B*, 39:57–65, 2008. 5

T. Thomas, H. Mahfuz, K. Kanny, and S. Jeelani. High Strain Rate Response of Cross-Linked and Linear PVC Cores. *Journal of Reinforced Plastics and Composites*, 23(7): 739–749, 2004. 10

O.T. Thomsen. Sandwich Materials and Structures for Wind Turbine Blades Present and Future Challenges. Presentation in the Advanced Sandwich Structures School during ICSS9, 2010. xi, 3, 4, 5

M.T. Tilbrook, V.S. Deshpande, and N.A. Fleck. Underwater blast loading of sandwich beams: regimes of behaviour. *International Journal of Solids and Structures*, 46:3209–3221, 2009. 36

L. Vu-Quoc, H. Deng, and X.G. Tan. Geometrically-exact sandwich shells: the static case. *Computer Methods in Applied Mechanics and Engineering*, 189:167–203, 2000. 22

E. Wang and A. Shukla. Blast response of sandwich composites using digital image correlation technique. In G. Ravichandran, editor, *Proceedings of the 9th International Conference on Sandwich Structures (ICSS9)*, June 2010. 6

E. Wang, N. Gardner, and A. Shukla. The blast resistance of sandwich composites with stepwise graded cores. *International Journal of Solids and Structures*, 46:3492–3502, 2009. 5

W.F. Xie, Y.L. Young, T.G. Liu, and B.C. Khoo. Dynamic response of deformable structures subjected to shock load and cavitation reload. *Computational Mechanics*, 40:667–681, 2007. 7, 36

W.F. Xie, Z. Liu, and Y.L. Young. Application of a coupled Eulerian-Lagrangian method to simulate interactions between deformable composite structures and compressible multiphase flow. *International Journal for Numerical Methods in Engineering*, 80:1497–1519, 2009. 7, 36

T. Yokozeki, S. Ogihara, S. Yoshida, and T. Ogasawara. Simple constitutive model for nonlinear response of fiber-reinforced composites with loading-directional dependence. *Composites Science and Technology*, 67:111–118, 2007. 16, 68

Y.K. Yong and Y. Cho. Higher-Order, Partial Hybrid Stress, Finite Element Formulation for Laminated Plate and Shell Analyses. *Computers and Structures*, 57(5):817–827, 1995. 22

Y.L. Young, Z. Liu, and W. Xie. Fluid-Structure and Shock-Bubble Interaction Effects During Underwater Explosions Near Composite Structures. *Journal of Applied Mechanics*, 76:051303–1–10, 2009. 7

C. Yu, A. Pandolfi, M. Ortiz, D. Coker, and A.J. Rosakis. Three-dimensional modeling of intersonic shear crack growth in asymmetrically loaded unidirectional composite plates. *International Journal of Solids and Structures*, 39:6135–6157, 2002. 19, 20, 68

F. Zhu, L.M. Zhao, G.X. Lu, and Z.H. Wang. Structural Response and Energy Absorption of Sandwich Panels with an Aluminium Foam Core Under Blast Loading. *Advances in Structural Engineering*, 11(5):525–536, 2008. 6

F. Zhu, L.M. Zhao, G.X. Lu, and E. Gad. A numerical simulation of the blast impact of square metallic sandwich panels. *International Journal of Impact Engineering*, 36(5): 687–699, 2009. 6